STELLENBOSCH UNIVERSITY

MASTER'S THESIS

Towards Atomic Physics Using Spatially Structured Light

Author:
Jason WEBSTER

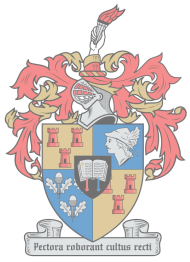

UNIVERSITEIT
iYUNIVESITHI
STELLENBOSCH
UNIVERSITY

Supervisors:
Dr. Hermann UYS
Co-supervisors:
Dr. Christine STEENKAMP
Prof. Andrew FORBES

A thesis submitted in partial fulfillment of the requirements for the degree of Masters in Physics

in the

Department of Physics
at
Stellenbosch University

December 2018

Declaration of Authorship

By submitting this thesis electronically, I declare that the entirety of the work contained therein is my own, original work, that I am the sole author thereof (save to the extent explicitly otherwise stated), that reproduction and publication thereof by Stellenbosch University will not infringe any third party rights and that I have not previously in its entirety or in part submitted it for obtaining any qualification.

December 2018

Abstract

Jason WEBSTER

Towards Atomic Physics Using Spatially Structured Light

Structured light has seen many applications in the fields of telecommunications, optical microscopy, and quantum information processing, however, few works exist that explore the interactions of structured light with atoms. In this thesis, we seek to explore these interactions further, both theoretically and experimentally. Of particular interest is the interaction between an atom and a Laguerre-Gauss beam of topological charge $\ell = 1$. Such a beam is easily constructed in a lab setting, and also carries an additional unit of orbital angular momentum that has been shown to couple with atomic transitions.

Theoretically, we derive a framework upon which to describe atomic transitions due structured light. We find that tailoring light's structure will have a direct influence on the strength of quadrupole transitions in atoms. A theoretical analysis of the effects of an atom situated in a magnetic field interacting with a Laguerre-Gauss beam of topological charge $\ell = 1$ was conducted. It was found that atoms placed in a region of zero intensity, such as the beam centre, can undergo quadrupole transitions – in contrast to dipole transitions that rely on the field intensity. We go on to show the differences between this beam and a gaussian beam, and find that the former can cause transitions between magnetic sub-levels that are typically considered forbidden in quadrupole spectroscopy under certain conditions. We explain this through the principle of conservation of angular momentum.

Experimentally, we chose to use a potassium vapour cell as our medium, as the linewidth of its quadrupole transition was relatively large, and could be simply modelled as a three-level system to easily understand its dynamics. We performed an experiment where we indirectly measured a $4^2\mathrm{S}_{1/2} \rightarrow 3^2\mathrm{D}_j$ quadrupole transition for $j = 3/2, 5/2$, induced by a custom-built external cavity diode laser operating at ~ 464.3 nm. The $4^2\mathrm{S}_{1/2} \rightarrow 3^2\mathrm{D}_j$ transition was measured by monitoring the fluorescence due to a dipole decay $4^2\mathrm{P}_{j'} \rightarrow 4^2\mathrm{S}_{1/2}$ during the decay cascade from $3^2\mathrm{D}_j \rightarrow 4^2\mathrm{P}_{j'} \rightarrow 4^2\mathrm{S}_{1/2}$, where $j' = 1/2, 3/2$. We then used our theoretical framework to fit the sum of two gaussian peaks to our measured fluorescence spectrum, and find an excellent agreement with our data.

Uittreksel

Jason WEBSTER

Atoom Fisika met Ruimtelik Gestruktureerde Lig

Gestruktureerde lig is reeds aangewend in verskeie toepassings in telekommunikasie, optiese mikroskopie, en kwantum informasie prosessering. Daar bestaan egter min pogings on die interaksie van gestruktureerde lig met atome te ondersoek. In hierdie tesis loods ons sodanige ondersoek, beide teoreties en eksperimenteel. Van besonder belang is die interaksie tussen 'n atoom en 'n Laguerre-Gauss laser straal met topologiese lading $\ell = 1$. So 'n straal kan maklik gekonstrueer word in 'n laboratorium en dra 'n addisionele eenheid hoekmomentum wat kan koppel met atomiese oorgange.

Teoreties herlei ons 'n raamwerk waarbinne die atomiese oorgan a.g.v. gestruktureerde lig beskryf kan word. Ons bevind dat die lig se struktuur 'n direkte invloed het op die sterkte van die kwadrupool oorgange in atome. 'n Teoretiese analise van die koppeling van 'n atoom met 'n Laguerre-Gauss straal met topologiese lading $\ell = 1$ terwyl dit in 'n magneet veld is word uitgevoer. Daar word bevind dat 'n atoom wat is by 'n posisie van nul veld-intensiteit steeds 'n kwadrupool oorgang kan ondergaan – in teenstelling met dipool oorgange. Ons beskryf voorts die verskille tussen sodanige straal en 'n Gaussiese straal, en bevind dat die voorgenoemde oorgange kan opwek tussen magnetise subvlakke wat tipies as verbode beskou work. Hierdie word verduidelik deur die behoud van hoekmomentum.

Eksperimenteel het ons kalium gekies as ons gassel medium, siende dat die kwadrupool oorgang van kalium betreklik wyd is en gemodelleer kan word met 'n eenvoudige drievlak model. Ons het ook 'n eksperiment uitgevoer om die $4^2\mathrm{S}_{1/2} \rightarrow 3^2\mathrm{D}_j$ kwadrupool oorgang indirek te meet, na opwekking met 464.3 nm lig uit 'n tuisgemaakte eksterne resonator diode laser. Die $4^2\mathrm{S}_{1/2} \rightarrow 3^2\mathrm{D}_j$ oorgang was waargeneem deur flouresensie te meet vanaf die $4^2\mathrm{P}_{j'} \rightarrow 4^2\mathrm{S}_{1/2}$ dipool oorgang se verval. Ons gebruik dan die teoretiese raamwerk om twee gaussiese pieke te pas teen die gemete fluoresensie spectrum en vind uitstekende ooreenstemming met ons data. Na die beste van ons wete is sodanige eksperimente nog nie voorheen op kalium uitgevoer nie, hoewel soortgelyke eksperimente al op sesium en rubidium toegepas was.

Acknowledgements

I'd firstly like to thank Dr. Hermann Uys, both as serving as my supervisor for this project and as a mentor throughout most of my physics career. Through his dedication to teaching complex subjects in simple ways, I've learned more from him than I could have hoped for, and I owe much of academic achievements to him.

I'd also like to thank Dr. Christine Steenkamp and Prof. Andrew Forbes for serving as co-supervisors. I also thank Dr. Steenkamp for offering to teach an unofficial Molecular Physics course after the official course had been unexpectedly removed. I'd also like to thank Prof. Forbes for pushing me far beyond my own expectations of what can be achieved throughout my career, and has shown me what it would take to be a leader in any field.

Finally to my parents, Malcolm and Bernice Webster, for their unending love and support thoughout my studies. To my father, who showed me the wonders of the world from a young age, and to my mother, who would always answer my questions about how the world worked.

Contents

Declaration of Authorship **iii**

Abstract **v**

Uittreksel **vii**

Acknowledgements **ix**

Contents **xi**

List of Figures **xiii**

List of Tables **xv**

List of Abbreviations **xvii**

1 Introduction **1**
1.1 Recap of light-matter interactions 1
1.2 Structuring light: Laguerre-Gauss beams 1
1.3 Review of structured light interacting with atoms 3

2 Background **7**
2.1 Electromagnetic waves and Laguerre-Gauss beams 7
2.1.1 Notation of EM fields 8
2.2 Atomic physics and angular momentum states 9
2.3 Atomic transitions 10
2.3.1 Einstein A and B coefficients 12
2.3.2 Rotating Wave Approximation 13
2.3.3 Rabi Frequency 14
2.3.4 Transition line-width and absorption cross section 14
2.3.5 Saturation Intensity 17
2.4 Spherical Tensors 17
2.5 The Wigner-Eckart theorem 18

3 Theory **21**
3.1 Quadrupole Coupling Theory 21
3.1.1 The quadrupole moment in terms of spherical tensors 21
3.1.2 Quadrupole selection rules 23
3.1.3 Effect of an external magnetic field on quadrupole transitions . 26
3.1.4 Quadrupole excitations in regions of zero-field intensity 28
3.1.5 Comparison of an OAM=1 beam to a Gaussian beam at the beam centre 29

3.1.6 Coupling strength outside of the beam centre 31
3.1.7 Transition strength comparison to dipole transitions 33
3.2 Experimental application of quadrupole coupling 33
3.2.1 Concerns from theoretical calculations 33
3.2.2 Three level model of potassium 34
3.2.3 Dynamics of the three level model 36
3.2.4 Saturation intensity and absorption cross-section 37

4 External Cavity Diode Laser **41**
4.1 Overview 41
4.2 Design and construction specifications 42
4.2.1 Principles for designing future ECDLs 43
4.3 Performance 45
4.3.1 Effect of diode current on ECDL metrics 45
4.3.2 Fabry-Perot spectrum 46
4.3.3 Free running stability over time 48
4.3.4 Scanning capability 49

5 Fluorescence Experiment **51**
5.1 Potassium reference data 51
5.2 Experimental Setup 54
5.3 Results and Analysis 56
5.4 Discussion 57
5.4.1 Choice of potassium over other atoms 58
5.4.2 Challenges in spectroscopy of quadrupole transitions 58

6 Conclusion **63**
6.1 Summary 63
6.2 Future Work 63

A Technical drawings of the ECDL **67**

Bibliography **77**

List of Figures

1.1 Transverse profiles of Laguerre-Gauss beams 2
1.2 Laguerre-Gauss beam side-profile 3

2.1 Atomic transition lineshape 16

3.1 Diagram of the polarization vector, magnetic field vector, and intensities of an $\ell = 0$ and $\ell = 1$ LG beam 27
3.2 Transition strength comparison between an $\ell = 0$ and $\ell = 1$ LG beam . 30
3.3 Plots of the quadrupole coupling strength as a function of the atom's position within the beam 32
3.4 Three level model of potassium 35

4.1 Diagrammatic representation of the ECDL that was constructed for our experiment. 42
4.2 Isometric view of the grating mount 43
4.3 Thorlabs pin classification system. LD = laser diode, PD = photodiode. 44
4.4 Graph of the output power of our ECDL as a function of the applied current 45
4.5 Graph of the output wavelength of our ECDL as a function of the applied current 45
4.6 Fabry-Perot spectrum of our ECDL 46
4.7 Plot of a single fabry-perot peak 47
4.8 Example spectrum of a multi-modal ECDL output 47
4.9 Plots of the wavelength and power of our ECDL over time 48
4.10 Graph of the measured wavelength over time during the single mode time period 48
4.11 Output frequency as a function of the voltage applied to the piezo placed behind the reflective grating in our ECDL 49

5.1 Energy levels of the ^{39}K potassium isotope 52
5.2 Vapor pressure curve of potassium 53
5.3 Experimental setup used to measure the fluorescence in a potassium gas cell 55
5.4 Initial doppler free experiment that we performed 59
5.5 Measured fluorescence of potassium as observed when the $4^2S_{1/2}$ to $3^2D_{3/2}$ transition is made 60
5.6 Measured fluorescence of potassium as observed when the $4^2S_{1/2}$ to $3^2D_{5/2}$ transition is made 60
5.7 Curve-fitting the sum of two gaussians to the fluorescence data collected from the $4^2S_{1/2}$ to $3^2D_{3/2}$ quadrupole transition 61

5.8 Curve-fitting the sum of two gaussians to the fluorescence data collected from the $4^2S_{1/2}$ to $3^2D_{5/2}$ quadrupole transition 61

List of Tables

3.1 Dipole fine-structure selection rules 24
3.2 Quadrupole fine-structure selection rules 25
3.3 Dipole hyperfine selection rules 26
3.4 Quadrupole hyperfine selection rules 26
3.5 Relative transition strength comparison between an $\ell = 0$ beam to an $\ell = 1$ beam 30

4.1 Summary of the parts used in our ECDL 44

5.1 Isotopes of potassium and their properties 51
5.2 Hyperfine constants of the ^{39}K potassium isotope 54

List of Abbreviations

AM	**A**ngular **M**omentum
OAM	**O**rbital **A**ngular **M**omentum
SAM	**S**pin **A**ngular **M**omentum
EM	**E**lectro**m**agnetic
RWA	**R**otating **W**ave **A**pproximation
ECDL	**E**xternal **C**avity **D**iode **L**aser

1 Introduction

1.1 Recap of light-matter interactions

One key fundamental aspect of atomic physics is light-atom interaction. This is because one of the few ways to probe atomic properties, such as their energy level transitions, is through light. Such interactions can be thought of in a semi-classical way, where the dipole setup between an atom's electrons and its positive core interact with a classically oscillating electric field to produce atomic transitions that only occur at certain allowed wavelengths of light corresponding to energy difference of the atomic transition in question [1]. More fundamentally, one can view these transitions as the absorption and emission of a photon whose energy matches the given transition energy [2, 3], which uncovers further properties of these transitions leading one to an understanding of the spectroscopic selection rules.

These optical selection rules, which state that for a dipole transition (known as an E1 transition) the total angular momentum (AM) of an electron L cannot change by more than one when undergoing an optical transition, as this AM is either transferred to an emitted photon ($\Delta L = -1$) or absorbed by a photon ($\Delta L = +1$) whose spin angular momentum (SAM) is always one. Outside of the dipole regime, one may, although rarely, encounter literature on quadrupole transitions (or more succinctly, E2 transitions). These occur when a second quanta of AM is absorbed or emitted by an electron, and are typically coupled to the gradient of an electromagnetic (EM) field – whereas dipole transitions are coupled to the field's amplitude. Since E2 transitions are coupled to the EM field's gradient, they tend to be much much weaker than a dipole transition, by a factor on the order of 10^{-6} when compared to a dipole transition. For this reason, quadrupole transitions are rarely studied due to the difficulty in achieving them and one typically studies atomic transitions in what is known as the dipole approximation [4].

It is the goal of this thesis to discuss the ways in which this selection rule is extended when the photon absorption/emission process contains not only a spin, but also an orbital component of angular momentum. These transitions go beyond the dipole approximation into the lesser studied E2 transitions as these involve the absorption or emission of a photon with a total AM of two, and allow an atomic electron to couple to both the spin and orbital components of the photon.

1.2 Structuring light: Laguerre-Gauss beams

Since we are looking to explore the interaction of atoms with not only the spin component of light, but also its orbital component, we need a light field that possesses

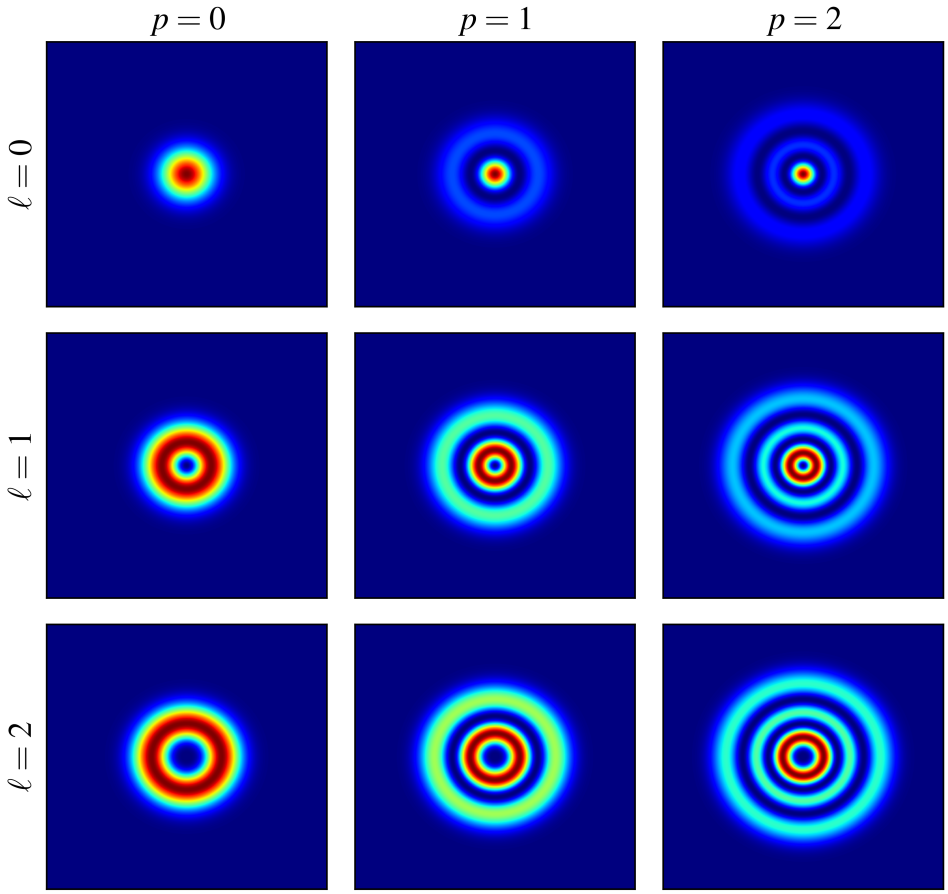

FIGURE 1.1: Transverse (xy) profiles of a Laguerre-Gauss beam for values of ℓ and p each ranging from 0 to 3.

an orbital angular momentum. Such a field is given readily by the Laguerre-Gauss (LG) beams and are the known paraxial regime solutions to the Helmholtz equation – which governs the solutions to Maxwell's source free equations. These beams are given in the cylindrical coordinates (r, ϕ, z) – where r is the radial, ϕ the azimuthal, and z the longitudinal coordinates of the beam, where the beam propagates along the z axis. The LG beams are characterized by the generalized Laguerre polynomial $\mathcal{L}_p^{|\ell|}$ [5] as well as an azimuthal phase $e^{i\ell\phi}$. The azimuthal number ℓ directly relates to the OAM of the beam about its centre L_z, where $L_z = \ell\hbar$ [6–8].

LG beams are cylindrically symmetric about their centre and possess a transverse Gaussian envelope which determines their overall propagation characteristics. Transverse profiles in the (r, ϕ) plane of the beam are shown in Fig. 1.1 for various values of the ℓ and p indices. Side profiles of the beam are shown in Fig. 1.2 for $p = 0$, $\ell = 0, 1$ and displays the focusing and defocusing effect inherent in any laser beam. One can see that increasing ℓ turns the gaussian beam into a 'donut' whose radius grows as ℓ grows, while p controls the number of rings surrounding the beam. For most practical purposes, we typically set $p = 0$.

Such beams are chosen due to their ease in generating them in a lab setting. Common methods for their generation include: phase plates, which introduce a $\exp(i\ell\phi)$ phase

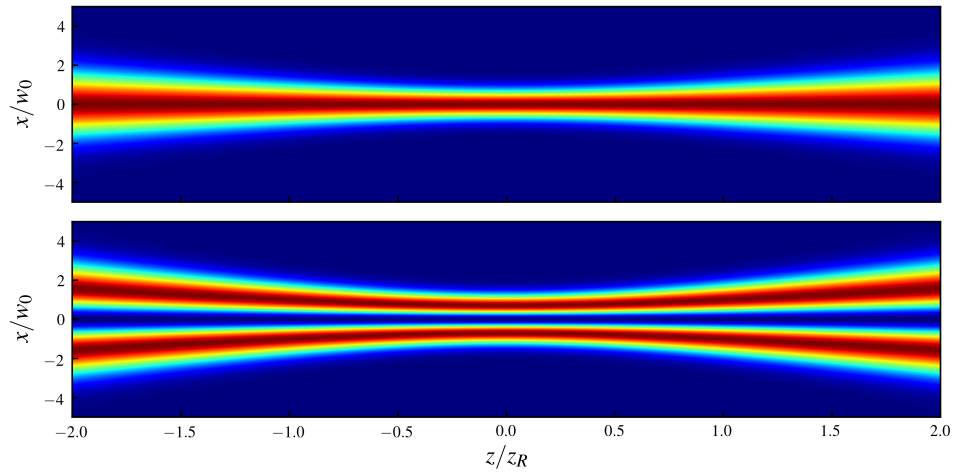

FIGURE 1.2: Laguerre-Gauss beam profiles as viewed from the side (xz) plane for $\ell = 0$ (top) and $\ell = 1$ (bottom). The beam is shown to focus and defocus around a point set to $z = 0$, where it reaches a beam diameter characterised as w_0, typically on the order of millimetres. The Rayleigh range $z_R = \pi w_0^2/\lambda$ is typically on the order of several meters. For a gaussian beam, propagating through one Rayleigh range corresponds to a change in beam width by a factor $\sqrt{2}$. The intensity in these plots have been amplified by a factor $1 + (z/z_R)^2$ in order to increase visibility of the beams outside of their focus.

into a gaussian beam [9, 10]; Q-plates, which convert a beam's SAM into OAM [11, 12]; and programmable spatial light modulators (SLMs) [13].

Laguerre-Gauss beams are not the only form of beam that can be structured, and in fact many additional classes of beams exist that solve the paraxial Helmholtz equation under different symmetry or coordinate considerations. Such additional classes include the Airy [14], Hermite-Gauss [6, 15], Ince-Gauss [16], and Hypergeometric-Gauss [17] beams. However, LG beams tend to be the most studied due to their ease in creating them, their favourable propagation properties, and their well-defined OAM about their axis of propagation. For the purposes of this thesis, we may use the term structured-light and Laguerre-Gauss mode interchangeably.

1.3 Review of structured light interacting with atoms

Since they were first studied in 1992 by Allen et. al. [6], Laguerre-Gauss beams have been the focus of numerous studies including telecommunications [18–21], optical microscopy [22–24], as well as quantum information and processing [25–27]. Several experiments demonstrating the interaction of a beam's OAM with macroscopic matter have also been performed using optical traps, where a beam's OAM can be transferred to a trapped particle, causing it to rotate [28–30], and 'doughnut-shaped' beams can even be used as traps themselves [31]. Rotating matter by using light can be thought of as an "optical spanner" [32] and allows for the construction of molecular scaled machines [33] powered by light.

On a more microscopic and fundamental scale, OAM beams have found applications involving the trapping and control of super-cold atoms [34]. Several experiments have been performed with Bose-Einstein condensates (BECs) that show one can both control the rotation of a BEC using light [35, 36], and observe the quantized transfer of well-defined OAM from light to a BEC using a two-photon Raman process [37] which can be used to create vortex phase qubits [38]. One can also optically pump the OAM of one light beam in to a system of cold cesium atoms and transfer this beam's OAM to a second beam, where the two beams are at different frequencies [39]. It is also possible to "store" the orbital angular momentum of light by making use of coherent population oscillation in cold cesium atoms [40].

Spectroscopic studies with structured light largely centre around producing dichroism effects in materials [41]. Some studies have attempted to determine whether or not light's OAM can interact with chiral matter, opening up possibilities of new spectroscopic techniques for detecting the chirality of matter, but have been inconclusive so far [42]. There's been some success with using OAM beams to narrow spectroscopic lines in Doppler-free spectroscopic setups [43], but the effect is quite weak, showing narrowing of the order of MHz for lines that are as wide as tens of MHz.

Though these applications are important in their own right, they do not involve the direct coupling of light's OAM to an atomic transition. Many theoretical works had been published that suggested such an interaction could take place [44–47], of which also demonstrated that new selection rules should arise if it did. It wasn't until 2016 that Schmiegelow et. al. , building on their previous theoretical work [44], performed the first experiment demonstrating the direct coupling of light's OAM to an atom's bound electron [48]. The experiment involved the use of a single trapped $^{40}Ca^{+}$ ion, and demonstrated that the ion could excite to previously forbidden E2 transitions. Not only that, but because E2 transitions couple to the field gradient, the experimenters had also shown that these transitions were possible in regions where the intensity was zero – specifically, they could excite an atom in the centre of a $\ell = 1$ beam, which as in Fig. 1.1 has zero field intensity.

The reason this experiment was so hard to perform is twofold. First, since E2 transitions are the second order interaction between light and atoms, they rely on the electric field gradient as well as the spatial extent of the atom. This effect leads to a transition strength that is of the order of 10^{-6} times weaker than that of E1 transitions, and as such, is nearly impossible in all but the most specialised of setups. Two highlighted theoretical works have been published in order to address the inaccessibility that may come with performing this experiment using an ion trap. The first [49] provides a comprehensive theoretical framework for analysing all quadrupole interactions as brought upon by an electric field's gradient, and is not restricted to focusing on the OAM of light. This paper also details that quadrupole interactions of rubidium can be enhanced when in the presence of an evanescent field created by an ultrathin optical fibre. The second paper [50] details increasing the electric field gradient through the use of nanofocusing effects that occur through the use of specially designed nano-scale plasmonic crystals.

Theoretical works have also been published that analyse the transfer of light OAM to molecules [51–54]. Of particular interest in these studies is the fact that a dipole transition involving the OAM of light could occur through a coupling between a

molecule's centre of mass OAM and the molecule's internal molecular rotation [54], but can only occur when such a molecule is polar (i.e. it is a two atom molecule whose constituents are not alike, e.g. carbon monoxide, CO). This type of transition does not, however, couple to the electronic motion [51] of the molecule, but only to the molecular rotation. In order to excite an electronic transition in a molecule one still needs to couple to the quadrupole moment.

2 Background

The purpose of this section is to refresh the reader on any topic that will be of use in this thesis. It is not meant to serve as an in-depth derivation of well-established formulae or theory, but rather provides a brief overview of certain important topics, along with textbook references should the reader require it. If the reader is familiar with any of the fields presented here, they are welcome to skip to the next section.

2.1 Electromagnetic waves and Laguerre-Gauss beams

The study of light, being an electromagnetic wave, starts by solving Maxwell's equations in a source free region, which for completeness is given by

$$\nabla \cdot \mathbf{E} = 0, \tag{2.1}$$
$$\nabla \cdot \mathbf{B} = 0, \tag{2.2}$$
$$\nabla \times \mathbf{E} = -\frac{\partial \mathbf{B}}{\partial t}, \tag{2.3}$$
$$\nabla \times \mathbf{B} = \mu_0 \varepsilon_0 \frac{\partial \mathbf{E}}{\partial t}, \tag{2.4}$$

where $\mathbf{E}$ and $\mathbf{B}$ are the electric and magnetic fields, and μ_0 and ε_0 are the vacuum permeability and permittivity, respectively. The solutions to this are easy to derive and typically follow by making $\mathbf{E} = U(\mathbf{r})e^{i\omega t}\hat{\boldsymbol{\epsilon}}$ where $\hat{\boldsymbol{\epsilon}}$ is a linear polarisation direction that lies in a plane transverse to the light's propagation, and $U(\mathbf{r})$ is a function that describes the spatial structure of the light field. After some brief algebraic manipulation, it can be shown that u must be a solution to the Helmholtz equation, defined as

$$\nabla^2 U + k^2 U = 0. \tag{2.5}$$

where $k/\omega = c$, $k = 2\pi/\lambda$, and $\omega = 2\pi f$, where λ is the wavelength of the light, and f is the frequency of the light.

From here, the paraxial approximation is made, where once we choose z as the axis of propagation, the $\partial^2 U/\partial z^2$ contribution to the Helmholtz equation is ignored and thought of as slowly varying compared to the rest of the terms. In cylindrical coordinates (r, ϕ, z) where $r^2 = x^2 + y^2$ and $\phi = \arctan(y/x)$, the family of solutions are

well-known and are named the Laguerre-Gauss beams, given by

$$U_{\ell p}(r,\phi,z) = \underbrace{\sqrt{\frac{2p!}{\pi(|\ell|+p)!}}\left(\frac{\sqrt{2}r}{w(z)}\right)^{|\ell|}\mathcal{L}_p^{|\ell|}\left(\frac{2r^2}{w^2(z)}\right)\exp(i\ell\phi)}_{\text{Orbital Angular Momentum}} \times \underbrace{\frac{w_0}{w(z)}\exp\left(\frac{-r^2}{w^2(z)}+\frac{ikr^2}{2R(z)}+i\Phi_g(z)+ikz\right)}_{\text{Gaussian Beam}}, \tag{2.6}$$

which for convenience has been grouped and labelled into the terms that cause OAM in the beam (given by $\ell\hbar$ per photon [6]), and the terms that are responsible for the Gaussian envelope and propagation. The terms $w(z)$, $R(z)$ and $\Phi_g(z)$ are the beam width, radius of curvature, and Guoy phase, respectively, and are defined as

$$w(z) = w_0\sqrt{1+\left(\frac{z}{z_R}\right)^2}, \tag{2.7}$$

$$R(z) = z\left[1+\left(\frac{z_R}{z}\right)^2\right], \tag{2.8}$$

$$\Phi_g(z) = (|\ell|+2p+1)\arctan\left(\frac{z}{z_R}\right). \tag{2.9}$$

The function $\mathcal{L}_l^p$ are the associated Laguerre polynomials [5] which give these family of solutions their name. Some examples of the beam's transverse profile and propagation charactersitics are given in Fig. 1.1 and Fig. 1.2.

2.1.1 Notation of EM fields

Typically, an electromagnetic field is given in complex form. This obviously does not make sense, as an EM field is a physical field, and therefore must be real. However, this notation is simply used as a shorthand to help describe many characteristics of the EM field in one simple equation. For example, if an EM field is denoted by a complex spatial field U and an arbitrary polarisation direction $\hat{\boldsymbol{\varepsilon}}$ with a propagation in the $\hat{\mathbf{z}}$ direction, the electric field is defined as the real part of this field (multiplied by the imaginary propagation factor $\exp(i\omega t)$), given by

$$\mathbf{E} = \mathrm{Re}(U\exp(i\omega t))\hat{\boldsymbol{\varepsilon}}. \tag{2.10}$$

Similarly, the magnetic field is defined as the real part of this field, with a polarisation direction that is at $90°$ to both the propagation direction $\hat{\mathbf{z}}$ and the electric field polarisation $\hat{\boldsymbol{\epsilon}}$, and is given by

$$\mathbf{B} = \frac{1}{k}\mathrm{Re}(U\exp(i\omega t))\left(\hat{\boldsymbol{\varepsilon}}\times\hat{\mathbf{z}}\right). \tag{2.11}$$

The intensity is given simply as

$$I = \frac{cn\varepsilon_0}{2}|U|^2, \tag{2.12}$$

where c is the speed of light and n is the refractive index of the medium through which light is travelling.

2.2 Atomic physics and angular momentum states

Atoms consist of essentially three particles: electrons that form a negatively charged outer shell structure, and a positive core composed of protons and neutrons. The electron motion constitutes the largest part of the energy structure of the electron. The next largest contributors to the energy level is due to relativistic corrections to the motion of the electron, as well as the spin-orbit coupling produced between the electron's spin magnetic moment and the magnetic field created by the electron's orbital motion. The final and smallest contributor is due to the spin-spin coupling, produced by the magnetic moment of the electron interacting with the nuclear core, to form the hyperfine structure.

The simplest atom to consider is the Hydrogen atom, featuring one proton and one electron. The Schrödinger equation for the electron in this case (assuming a stationary atom) is then

$$i\hbar\frac{\partial\Psi}{\partial t} = \left[-\frac{\hbar^2}{2m_e}\nabla^2 - \frac{e^2}{4\pi\varepsilon_0}\frac{1}{r}\right]\Psi, \tag{2.13}$$

the analytical solutions of which are easily found in any quantum mechanics textbook (see for example Griffiths [1]). The electron wavefunction is most readily described in terms of three quantum numbers, n, L, and M, where n is termed the principle quantum number being responsible for the allowed energy levels that the electron can exist in, L is the OAM of the electron's motion about the positive core, and M is the projection of the angular momentum on some predefined (usually z) axis. The angular momentum operators L^2 and L_z, and the angular momentum state $|n\,L\,M\rangle$ satisfy

$$\begin{aligned} H\,|n,L,M\rangle &= E_n\,|n\,L\,M\rangle \\ L^2\,|n,L,M\rangle &= \hbar^2 L(L+1)\,|n\,L\,M\rangle \\ L_z\,|n,L,M\rangle &= \hbar M\,|n\,L\,M\rangle\,, \end{aligned} \tag{2.14}$$

where E_n is the Rydberg energy for the n^{th} level, defined as $E_n = -13.6\text{eV}/n^2$. The angular momentum numbers are constrained such that $0 \leq L \leq n-1$, $-L \leq M \leq L$ and must be integers. A value $n = 1$ corresponds to the ground state, and n takes on only positive integer values. The energy levels here are degenerate, since each level n can contains $\sum_{L=0}^{n-1} L$ states, each of which contain $2L+1$ number of L_z projections, leading to a total degeneracy of $g_n = n^2$.

This solution is oversimplified, as we have yet to include the fine structure splitting. Firstly, an electron has an intrinsic spin, which sets up an intrinsic magnetic moment $\boldsymbol{\mu}_e$ defined as

$$\boldsymbol{\mu}_e = -g_e\frac{e}{2m_e}\mathbf{S} \tag{2.15}$$

where $\mathbf{S} = S_x + S_y + S_z$ is the intrinsic angular momentum of the electron, e is the charge of the electron, and g_e is the anomalous gyromagnetic factor which is approximately $g_e \approx 2$. As the electron orbits the proton, it sees (in its frame of reference) a proton orbiting it, leading to a magnetic field B at the location of the

electron. This interacts with the electron's intrinsic magnetic moment, giving an interaction energy given by $H_I = -\boldsymbol{\mu}_e \cdot \mathbf{B}$. This is termed *spin-orbit coupling* as it's a coupling between an electron's intrinsic spin and its orbital motion. The other contributor to the fine structure is a relativistic correction, which can be calculated by expanding the relativistic kinetic energy to a first order correction term.

The net result leads to a correction in the energy levels that, to first order, depends on the quantum number J, where

$$\mathbf{J} = \mathbf{L} + \mathbf{S} \tag{2.16}$$

and J can be equal to $J = |L - S|, |L - S| + 1, \ldots, L + S - 1, L + S$, and leads one to define a new quantum state $|n, L, J, M_J\rangle$. For an electron, $S = 1/2$, so for example a state where $L = 1$, J can be $J = 1/2$ or $J = 3/2$. Due to the spin-orbit coupling, there will be a small energy difference between the $J = 1/2$ and $J = 3/2$ states. The new degeneracy for each energy level is now $g_J = 2J + 1$ as is caused solely due to the number of projections an electron state can have on the z axis with the J_z operator. This degeneracy can be further lifted by making use of the *Zeeman effect* (see Griffiths [1] or Foot [4] for textbook references), which occurs when applying an external magnetic field, and allows one isolate a particular eigenstate $|n, L, J, M_J\rangle$ to its own energy level if we choose the z axis to align with the magnetic field direction.

The last correction that occurs is called hyperfine splitting, and is due to the proton's intrinsic spin interacting with the electron's spin. In a similar process to above, one ends up defining a quantum number F whose spin vector is given by

$$\mathbf{F} = \mathbf{J} + \mathbf{I}, \tag{2.17}$$

where $\mathbf{I}$ is the intrinsic spin of the proton. This leads one to define a final atomic state $|n, L, J, F, M_F\rangle$ and is usually written for convenience as $|n, F, M_F\rangle$. The degeneracy here is, again, just $g_F = 2F + 1$ due to the magnetic level degeneracy and can be lifted through the use of the Zeeman effect.

2.3 Atomic transitions

Before discussing atomic transitions, it is first important to discuss the interaction energy between an atom and an external EM field. An atom is, after all, an electromagnetic system, and is held together by electromagnetic forces, so it is obvious that such a system should interact with an EM field. It is also well known that atoms can absorb and emit light. To derive this interaction energy, one makes use of the electromagnetic potentials, defined as

$$\mathbf{E} = -\boldsymbol{\nabla} V - \frac{\partial \mathbf{A}}{\partial t}, \tag{2.18}$$

$$\mathbf{B} = \boldsymbol{\nabla} \times \mathbf{A}. \tag{2.19}$$

Assuming that the EM field is slowly varying over the charge distribution $\rho(\mathbf{r})$ such that $\partial\mathbf{A}/\partial t \approx 0$, it is possible to derive (see [1, 55] for textbook references) the interaction energy of this charge distribution $\rho(\mathbf{r})$ with an external EM field as

$$\begin{aligned} H_{int} &= \int d^3r \left[\rho(\mathbf{r})V(\mathbf{r}) - \mathbf{j}(\mathbf{r})\cdot A(\mathbf{r})\right] \\ &= \int d^3r \left[\rho(\mathbf{r})\left(V(0) + \partial_i V(0) r^i + \frac{1}{2}\partial_i\partial_j V(0) r^i r^j + \dots\right)\right. \\ &\left. -\mathbf{j}(x)\cdot\left(\mathbf{A}(0) + \partial_i\mathbf{A}(0) r^i + \frac{1}{2}\partial_i\partial_j\mathbf{A}(0) r^i r^j \dots\right)\right] \\ &= qV(0) - \mathbf{d}\cdot\mathbf{E} - \frac{1}{6}Q_{ij}\frac{\partial E_j}{\partial r_i} + \dots, \end{aligned} \tag{2.20}$$

where I've expanded the interaction into its multipolar form to the first three leading orders (which ignores the magnetic terms as these are too weak to consider), and have used the Einstein summation convention as shorthand (repeated indices are summed). The quantities that arise in the expansion are given by, respectively, the electric monopole, dipole, and quadrupole moments, defined by

$$q = \int d^3r\rho(\mathbf{r}) \qquad = \qquad \sum_i q_i \tag{2.21}$$

$$\mathbf{d} = \int d^3r\rho(\mathbf{r})\mathbf{r} \qquad = \qquad \sum_i q_i\mathbf{r}_i \tag{2.22}$$

$$Q_{ij} = \underbrace{\int d^3r(3r_i r_j - r^2\delta_{ij})\rho(\mathbf{r})}_{\text{Charge distribution } \rho(\mathbf{r})} \qquad = \qquad \underbrace{\sum_k (3r_{ki}r_{kj} - r_k^2\delta_{ij})q_k}_{\text{Point charges } q_i = q(\mathbf{r}_i)} \tag{2.23}$$

where δ_{ij} is the Kronecker delta symbol. It should be noted that the electric field terms in (2.20) are evaluated at the position of the centre of mass of the atom, while the dipole or quadrupole terms are written as functions of the electron coordinates.

The Hamiltonian for an electron in an external magnetic field is then

$$H = H_0 + H_{int} \tag{2.24}$$

where

$$H_0 = \left[-\frac{\hbar^2}{2m_e}\nabla^2 + V(\mathbf{r})\right], \tag{2.25}$$

with $V(\mathbf{r})$ being the potential that the electron is in (for a hydrogen atom, this is the usual $V(\mathbf{r}) = -\frac{e^2}{4\pi\varepsilon_0}\frac{1}{|\mathbf{r}|}$, but for any other atom $V(\mathbf{r})$ includes the contributions of the other electrons). The interaction Hamiltonian is usually simplified to

$$H_{int} \approx -\mathbf{d}\cdot\mathbf{E}, \tag{2.26}$$

as the contribution from the monopole term does not contribute to the dynamics of the system. The reason the quadrupole term is omitted is because $Q_{ij} \sim er^2$, and for a light field $\partial E_j/\partial r_i \sim k$, so for an atom (whose typical field of influence is an Angstrom) interacting with a visible light field, we have $r \approx 1\times10^{-10}$ m and

$k \approx 1 \times 10^7$ m^{-1}. Thus, the contribution by the quadrupole term is 1×10^{-3} smaller than the dipole term (where $|\mathbf{d}| \sim er$). This is known as the *dipole approximation* as we only consider the dipole interaction of the electric field with the atom.

This allows us to write the energy, or diagonal terms, of the Hamiltonian by purely using the H_0 term, giving (for a simple atomic state) $\langle n, l, m|H_0|n, l, m\rangle$ and gives the energy of the state. The off-diagonal matrix elements of the Hamiltonian is written purely with the interaction Hamiltonian as $\langle n', l', m'|H_{int}|n, l, m\rangle$ and is related to the transition probability between the $|n', l', m'\rangle$ and $|n, l, m\rangle$ states.

2.3.1 Einstein A and B coefficients

It can be shown that for atoms in thermal equilibrium there exists a decay rate from an excited energy state $|e\rangle$ to a lower ground state $|g\rangle$, known as the Einstein A coefficient that corresponds to spontaneous emission. To derive this coefficient, one first solves the time dependant Schödinger equation for the atomic interaction Hamiltonian described in (2.24). This will lead one (see [1]) to a transition rate between the ground and excited state corresponding to both the stimulated emission and absorbtion rates, given by

$$\Gamma_{g\leftrightarrow e} = \frac{\pi|\langle e|\mathbf{d}|g\rangle|^2}{3\varepsilon_0\hbar^2}\rho(\omega_{ge}) = B\rho(\omega_{ge}), \tag{2.27}$$

where $\rho(\omega_{ge})$ is the energy density of an electromagnetic field at the frequency $\omega_{ge} = (E_e - E_g)/\hbar$, $\mathbf{d}$ is the dipole moment from (2.22), and

$$B = \frac{\pi|\langle e|\mathbf{d}|g\rangle|^2}{3\varepsilon_0\hbar^2} \tag{2.28}$$

is the Einstein B coefficient.

Deriving the Einstein A is an elementary procedure, involving a simple rate equation and elementary statistical mechanics principles. One finds that the Einstein A coefficient is given by

$$A = \frac{\omega_{ge}^3\hbar}{\pi^2c^3}B, \tag{2.29}$$

or

$$A = \frac{\omega_{ge}^3|\langle e|\mathbf{d}|g\rangle|^2}{3\pi\varepsilon_0\hbar c^3}. \tag{2.30}$$

This was the way Einstein did it. A more modern approach to calculating these quantities is through the Weiskopf-Wigner theory which considers the coupling of the atom to the electromagnetic vacuum field. A good, and somewhat brief, derivation of the A and B coefficients through the Weiskopf-Wigner theory can be found online at [56]. More detailed derivations can be found in Steck's Quantum Optics [3].

2.3.2 Rotating Wave Approximation

Imagine a a two level system with states $|g\rangle$ and $|e\rangle$ with energy levels 0 and $\hbar\omega_{ge}$ (where ω_{ge} is the frequency difference between the ground and excited states), respectively, interacting with a monochromatic EM field $\mathbf{E} = \mathbf{E}_0\cos(\omega t)$. In this system, the dipole operator $\mathbf{d}$ can be decomposed into the form

$$\mathbf{d} = \langle e|\mathbf{d}|g\rangle\,|e\rangle\langle g| + \langle g|\mathbf{d}|e\rangle\,|g\rangle\langle e|\,, \tag{2.31}$$

where by parity considerations the diagonal terms $\langle e|\mathbf{d}|e\rangle = \langle g|\mathbf{d}|g\rangle = 0$ as is shown in [1, 3, 4]. We can define the lowering operator σ as

$$\sigma = |g\rangle\langle e|\,, \tag{2.32}$$

whose action on an atomic state lowers it from the excited state to the ground state. Choosing the phase of $\langle e|\mathbf{d}|g\rangle$ to be real, we have

$$\mathbf{d} = \langle e|\mathbf{d}|g\rangle\left(\sigma + \sigma^\dagger\right). \tag{2.33}$$

We can then write the terms of the Hamiltonian as

$$H_0 = \hbar\omega_{ge}\,|e\rangle\langle e| = \hbar\omega_e\sigma\sigma^\dagger, \tag{2.34}$$

$$H_{int} = -\langle e|\mathbf{d}|g\rangle\cdot\mathbf{E}\left(\sigma + \sigma^\dagger\right). \tag{2.35}$$

In the free atomic setup, where only H_0 applies, the time-dependent Heisenberg equation of motion for the σ operator gives

$$\partial_t\sigma = -\frac{i}{\hbar}[H_0, \sigma] \tag{2.36}$$

whose solution can be easily found as

$$\sigma(t) = \sigma_0 e^{-i\omega_{ge}t}. \tag{2.37}$$

One can then see that in (2.35) that the product between $\mathbf{E}$ and $\left(\sigma + \sigma^\dagger\right)$ will produce terms that oscillate rapidly as $e^{\pm i(\omega+\omega_{ge})}$ and slowly as $e^{\pm i\Delta t}$, which arise due to the fact that for a monochromatic field $\mathbf{E}$ can be expressed as

$$\mathbf{E} = \mathbf{E}_0\cos(\omega t) = \frac{1}{2}\left(\mathbf{E}_0 e^{-i\omega t} + \mathbf{E}_0 e^{i\omega t}\right). \tag{2.38}$$

We've also defined

$$\Delta = \omega - \omega_{ge} \tag{2.39}$$

as the detuning of the incident light field from the atomic resonance.

The rotating wave approximation (RWA) simply ignores the fast oscillating terms $e^{\pm i(\omega+\omega_{ge})}$ from the equation (their oscillations are considered fast enough to average to zero). More formally, this corresponds to the unitary transformation U where

$$U = \exp(i\omega t\,|e\rangle\langle e|), \tag{2.40}$$

which transforms an operator $H \to \tilde{H}$ by

$$\tilde{H} = UHU^\dagger + i\hbar(\partial_t U)U^\dagger, \tag{2.41}$$

and transforms a state $|\psi\rangle \to |\tilde{\psi}\rangle$ by

$$|\tilde{\psi}\rangle = U|\psi\rangle . \tag{2.42}$$

In practice, the tilde's above the transformed operators and states are widely ignored, as it is very common place to make the RWA.

2.3.3 Rabi Frequency

If we write out (2.35) in the RWA, we have

$$H_{int} = -\frac{1}{2}\Big(\langle e|\mathbf{d}|g\rangle \cdot \mathbf{E}_0\sigma - \langle e|\mathbf{d}|g\rangle \cdot \mathbf{E}_0\sigma^\dagger\Big). \tag{2.43}$$

If we define the Rabi frequency Ω as

$$\Omega = -\frac{\langle e|\mathbf{d}|g\rangle \cdot \mathbf{E}_0}{\hbar}, \tag{2.44}$$

then (2.35) becomes

$$H_{int} = \frac{\hbar\Omega}{2}\Big(\sigma + \sigma^\dagger\Big) \tag{2.45}$$

When one solves the atomic Schrödinger equation with $H = H_0 + H_{int}$ and ignores spontaneous emission, one quickly finds a solution where the state oscillates between the being purely in the excited state $|e\rangle$ and purely in the ground state $|g\rangle$, where the oscillation frequency is precisely the Rabi frequency [1, 3, 4].

2.3.4 Transition line-width and absorption cross section

To fully understand atomic transitions, it is useful to introduce the density matrix operator, defined as

$$\rho = \sum_{i,j} \rho_{ij} |i\rangle\langle j| , \tag{2.46}$$

which has the property that, for a state $|i\rangle$, the probability to be in that state is ρ_{ii} (i.e. the diagonal elements correspond to state probabilities). Off-diagonal elements ρ_{ij} correspond to coherences between states $|i\rangle$ and $|j\rangle$. In the Heisenberg picture, the equation of motion for the density matrix for atomic systems interacting with an EM field can be conveniently written as

$$\partial_t \rho = -\frac{i}{\hbar}[H_0 + H_{int}, \rho] + \Gamma\mathcal{D}[\sigma]\rho, \tag{2.47}$$

where σ is the atomic lowering operator defined previously, which again for a two level system is $\sigma = |g\rangle\langle e|$ so that $\sigma|e\rangle = |g\rangle$. The Lindbald superoperator $\mathcal{D}[A]$ is

defined for an operator A as

$$\mathcal{D}[A]\rho = A\rho A^\dagger - \frac{1}{2}\left(A^\dagger A\rho + \rho A^\dagger A\right). \tag{2.48}$$

The origin of this superoperator in this equation is quite complicated, but it essentially represents a form of decay for the quantum system. More formally, the Lindbald superoperator represents the coupling of our atomic system with some kind of environment (in this case, the environment is the background electromagnetic field). For more on this superoperator, as well as its derivation, see Chapter 4.5 of Steck [3].

Writing (2.47) out for a two level system in the RWA, we have

$$\begin{aligned}
\partial_t\rho_{ee} &= i\frac{\Omega}{2}(\rho_{eg} - \rho_{ge}) - \Gamma\rho_{ee},\\
\partial_t\rho_{gg} &= -i\frac{\Omega}{2}(\rho_{eg} - \rho_{ge}) + \Gamma\rho_{ee},\\
\partial_t\rho_{ge} &= -i\Delta\rho_{ge} - i\frac{\Omega}{2}(\rho_{ee} - \rho_{gg}) - \frac{\Gamma}{2}\rho_{ge},\\
\partial_t\rho_{eg} &= i\Delta\rho_{ge} + i\frac{\Omega}{2}(\rho_{ee} - \rho_{gg}) - \frac{\Gamma}{2}\rho_{eg}.
\end{aligned} \tag{2.49}$$

The Γ coefficient can be identified as the Einstein A coefficient from (2.30). Γ tends to be preferred when talking of decay rates due to notational preferences. When we solve for ρ_{ee} in the steady state $\partial_t\rho \to 0$ we find

$$\rho_{ee} = \frac{\Omega^2/\Gamma^2}{1 + \left(\frac{2\Delta}{\Gamma}\right)^2 + \frac{2\Omega^2}{\Gamma^2}}, \tag{2.50}$$

and because $\mathrm{Tr}[\rho] = 1$ we have $\rho_{gg} = 1 - \rho_{ee}$.

If this atomic system were, say, irradiated by a source of light travelling along the z-axis, then a simple conservation of energy consideration, as in [4], would show that

$$\frac{\mathrm{d}I}{\mathrm{d}z} = -N(\rho_{gg} - \rho_{ee})\sigma(\omega)I(\omega), \tag{2.51}$$

where N is the number of particles in the atomic system, and $\sigma(\omega)$ is the absorption cross section for light at frequency ω. In a steady state, the conservation of energy requires

$$N(\rho_{gg} - \rho_{ee})\sigma(\omega)I(\omega) = N\rho_{ee}\Gamma\hbar\omega_{ge}, \tag{2.52}$$

where I is the intensity of the light. This essentially states that the energy absorbed by the system (left-hand side of the above) must be equal to the energy emitted by the system (i.e. the rate of spontaneous emission) Thus we can write a solution to the cross-section, given by

$$\sigma(\omega) = \frac{6\pi c^2}{\omega_{ge}^2} g_H(\omega), \tag{2.53}$$

where

$$g_H(\omega) = \frac{1}{1 + \left(\frac{2\Delta}{\Gamma}\right)^2}, \tag{2.54}$$

is the Lorentzian line-shape of the absorption cross section, whose full-width at half-maximum (FWHM) can be calculated as

$$\text{FWHM} = \Gamma. \tag{2.55}$$

So, the line-width of a transition is given by the decay rate Γ. This is plotted in Fig. 2.1.

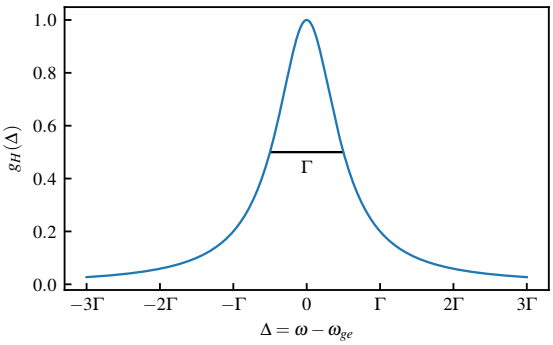

FIGURE 2.1: Plot of the atomic transition lineshape g_H vs $\Delta = \omega - \omega_{ge}$, illustrating the FWHM as Γ.

The peak absorption cross-section is given on resonance at $\omega = \omega_{ge}$ as

$$\sigma(\omega_{ge}) = \frac{3\lambda_{ge}^2}{2\pi}, \tag{2.56}$$

where $\lambda_{ge} = 2\pi c/\omega_{ge}$ is the wavelength of light.

This is rarely the lineshape we recover, as here we've assumed that the atom is stationary. In reality, the line shape is broadened when we assume a non-stationary atom. This is due to the fact that a non-stationary atom will see light either blue or red shifted, depending on the direction it is travelling relative to the light's propagation. Thus, a certain velocity class of atoms will be resonant with a field that would be considered off-resonant in a stationary frame of reference. This effect is known as doppler broadening, and a detailed derivation of this effect can be found in [3, 4]. To overcome this, one often makes use of a doppler free setup that involves the use of two overlapping counter-propagating beams, where one beam (the pump) typically operates at the saturation intensity, while another (the probe) is typically at 10% the intensity of the pump. The probe is then compared to a another beam (the reference) which does not overlap the pump beam, and a difference between the two intensities is taken in order to retrieve an approximately lorentzian lineshape for each atomic transition in our spectrum. Details of this can be found in [4], and an example of a doppler free setup can be seen in Fig. 5.4.

2.3.5 Saturation Intensity

The equation in (2.52) can also be used to solve for the population difference $\rho_{gg}-\rho_{ee}$, and yields

$$\rho_{gg} - \rho_{ee} = \frac{1}{1 + I/I_s(\omega)}, \tag{2.57}$$

where the saturation intensity parameter $I_s(\omega)$ is defined as

$$I_s(\omega) = \frac{\hbar\omega_{ge}\Gamma}{2\sigma(\omega)}, \tag{2.58}$$

whose minimum is given at resonance as

$$I_s(\omega_{ge}) = \frac{2\pi^2\hbar c\Gamma}{3\lambda^3} \tag{2.59}$$

and is often referred to as *the saturation intensity* for a radiative transition. One should aim at using an intensity somewhere in this region when trying to perform spectroscopic measurements.

2.4 Spherical Tensors

The spherical basis, useful when discussing atomic transitions, is defined as

$$\begin{aligned} \hat{\mathbf{e}}_{\pm1} &= \mp\frac{1}{\sqrt{2}}(\hat{\mathbf{x}} \pm i\hat{\mathbf{y}}) = -(\hat{\mathbf{e}}_{\mp1})^*, \\ \hat{\mathbf{e}}_0 &= \hat{\mathbf{z}} = (\hat{\mathbf{e}}_0)^*, \end{aligned} \tag{2.60}$$

where a vector $\mathbf{A} = A_x\hat{\mathbf{x}} + A_y\hat{\mathbf{y}} + A_z\hat{\mathbf{z}}$ is written as

$$\begin{aligned} A_{\pm1} &= \frac{1}{\sqrt{2}}(A_x \pm iA_y), \\ A_0 &= A_z, \\ \mathbf{A} &= \sum_q (-1)^q A_q\hat{\mathbf{e}}_{-q} = \sum_q A_q\hat{\mathbf{e}}_q^*. \end{aligned} \tag{2.61}$$

In this basis, the position operator $\mathbf{r} = x\hat{\mathbf{x}} + y\hat{\mathbf{y}} + z\hat{\mathbf{z}}$ (which is related to the dipole operator $\mathbf{d} = -e\mathbf{r}$) has the components given by

$$r_q = r\sqrt{\frac{4\pi}{3}}Y_1^q(\theta,\phi), \tag{2.62}$$

where $Y_l^q(\theta,\phi)$ are the well known spherical harmonics of degree l and order q [3].

Spherical tensors are mathematical objects that transform the same way as the spherical harmonics. They are written as $T_q^{(k)}$, and are of degree k and order q, where k and q are equivalent to l and q in $Y_l^q(\theta,\phi)$. These are generalised abstractions of the functions that are spherical harmonics. In practice though, one often sets $T_q^{(k)}$ to be

equal to its equivalent spherical harmonic $Y_k^q(\theta,\phi)$ up to some factor. The restrictions on k and q are

$$k \geq 0, \quad -k \leq q \leq k, \quad k, q \in Z \tag{2.63}$$

From Steck's "Quantum Optics Notes" [3], one can find the following properties for spherical tensors:

$$T_{q_1}^{(k_1)} T_{q_2}^{(k_2)} = \sum_{k,q} \sqrt{\frac{(2k_1+1)(2k_2+1)}{4\pi(2k+1)}} \langle k_1\, q_1, k_2\, q_2 | k\, q\rangle \langle k\, 0 | k_1\, 0, k_2\, 0\rangle\, T_q^{(k)}, \tag{2.64}$$

$$T_q^{(k)} = \sum_{q_1 q_2} T_{q_1}^{(k_1)} T_{q_2}^{(k_2)} \langle k_1\, q_1, k_2\, q_2 | k\, q\rangle\,, \tag{2.65}$$

$$R(\boldsymbol{\zeta}) T_q^{(k)} R^\dagger(\boldsymbol{\zeta}) = \sum_{q'=-k}^{k} T_{q'}^{(k)} d_{q'q}^{(k)}(\boldsymbol{\zeta}), \tag{2.66}$$

where (2.64) is the recoupling relation, (2.65) is the product rule, (2.66) is the rotation relation for a rotation operator R and a rotation vector $\boldsymbol{\zeta}$ where $d_{q'q}^{(k)}$ is known as the Wigner-d matrix.

The Wigner-d $d_{q'q}^{(k)}$ can be explicitly calculated when $\boldsymbol{\zeta}$ is given in Euler angles $\boldsymbol{\zeta} = \alpha\hat{\mathbf{z}} + \beta\hat{\mathbf{y}}' + \gamma\hat{\mathbf{z}}''$ where $\hat{\mathbf{y}}'$ is the new y-direction after the $\alpha\hat{\mathbf{z}}$ rotation, and $\hat{\mathbf{z}}''$ is the new z-direction after the $\beta\hat{\mathbf{y}}'$ rotation. The rotation matrix, represented in the old $(\hat{\mathbf{x}}, \hat{\mathbf{y}}, \hat{\mathbf{z}})$ coordinate system before the rotation, is then

$$d_{q'q}^{(k)}(\boldsymbol{\zeta}) = e^{-iq'\alpha} d_{q'q}^{(k)}(\beta\hat{\mathbf{y}}) e^{-iq\gamma}, \tag{2.67}$$

where

$$d_{q'q}^{(k)}(\beta\hat{\mathbf{y}}) = \sqrt{(k+q)!(k-q)!(k+q')!(k-q')!} \times \sum_s \frac{(-1)^s}{(k-q'-s)!(k+q-s)!(s+q'-q)!s!} \left(\cos\frac{\beta}{2}\right)^{2k+q-q'-2s} \left(-\sin\frac{\beta}{2}\right)^{q'-q+2s}, \tag{2.68}$$

and the sum over s occurs for all values where the arguments of the factorials are positive.

2.5 The Wigner-Eckart theorem

The basis of the Wigner-Eckart theorem relies on the fact that the spherical tensor $T_q^{(k)}$ transforms like the angular momentum ket $|k\, q\rangle$, while the atomic state $|n\, l\, m\rangle$ transforms like the angular momentum ket $|l\, m\rangle$. As such, the product $T_q^{(k)} |n\, l\, m\rangle$ transforms like the composite state $|k\, q\rangle\, |l\, m\rangle$. When we consider the angular momentum addition relation

$$T_q^{(k)} |n\, l\, m\rangle \sim |k\, q; l\, m\rangle = \sum_{k'q'} |k'\, q'\rangle \langle k'\, q' | l\, m; k\, q\rangle\,, \tag{2.69}$$

where $\langle k'\, q' | l\, m;\, k\, q\rangle$ is a Clebsch-Gordon coefficient. Premultiplying this by $\langle n'\, l'\, m'|$ yields

$$\left\langle n'\, l'\, m' \right| T_q^{(k)} \left| n\, l\, m \right\rangle = \left\langle n'\, l'\, m' \middle| n\, l'\, m' \right\rangle \left\langle l'\, m' \middle| l\, m;\, k\, q \right\rangle , \tag{2.70}$$

where $\langle n'\, l'\, m'|n\, l'\, m'\rangle$ is some m'-independent quantity (and thus orientation independent quantity) and relies only on the radial part of the wavefunction of the electron. We define this by the reduced matrix element

$$\langle n'\, l' || \mathbf{T}^{(k)} || n\, l \rangle = (-1)^{2k} \left\langle n'\, l'\, m' \middle| n\, l'\, m' \right\rangle , \tag{2.71}$$

thus, after substituting into (2.70), we get the Wigner-Eckart theorem as

$$\left\langle n'\, l'\, m' \right| T_q^{(k)} \left| n\, l\, m \right\rangle = (-1)^{2k} \langle n'\, l' || \mathbf{T}^{(k)} || n\, l \rangle \left\langle l'\, m' \middle| l\, m;\, k\, q \right\rangle . \tag{2.72}$$

This has particular importance for dipole transitions as, from (2.62) and defining $T_q^{(1)} = r\sqrt{\frac{4\pi}{3}} Y_1^{(q)}$ we have

$$\mathbf{r} = \mathbf{T}^{(1)}, \tag{2.73}$$

and thus with $\mathbf{d} = -e\mathbf{r}$, and with $H_{int} \sim \mathbf{d} \cdot \mathbf{E}$ means that the matrix elements of H_{int} are calculated with the Wigner-Eckhart theorem. This theorem essentially states that all atomic transitions can be calculated using some m-independent factor (the $\langle n'\, l' || \mathbf{T}^{(k)} || n\, l \rangle$ factor) multiplied with a Clebsch-Gordon coefficient.

3 Theory

In this section I discuss the most important theoretical elements of my thesis. Most, if not all, of the theoretical conclusions made here are fully derived in this section. Discussions also accompany these theoretical calculations, as well as the implications these conclusions have when one wishes to perform experiments.

3.1 Quadrupole Coupling Theory

3.1.1 The quadrupole moment in terms of spherical tensors

Most atomic literature deals with the dipole approximation, that is to take (2.20) and to only keep the dipole interaction, leading to an interaction Hamiltonian $H_{int} = -\mathbf{d}\cdot\mathbf{E}$. Here, we consider the next leading term in the expansion of H_{int} from (2.20), that is, the quadrupole interaction

$$H_{Q,int} = -\frac{1}{6}\sum_{i,j} Q_{ij}\frac{\partial E_j}{\partial r_i}, \tag{3.1}$$

where the quadrupole moment for an atom with Z electrons at positions $\mathbf{r}_1,\ldots,\mathbf{r}_n$, and a nucleus at position $\mathbf{r}_0 = 0$, is

$$Q_{ij} = -e\sum_{k=1}^{Z}\left(3r_{ki}r_{kj} - \delta_{ij}r_k^2\right), \tag{3.2}$$

where the k^{th} electron is at position $\mathbf{r}_k$ and r_{ki} represents the i^{th} component of the vector $\mathbf{r}_k$. In matrix form, this is written as

$$[Q_{ij}] = \begin{bmatrix} Q_{xx} & Q_{xy} & Q_{xz} \\ Q_{yx} & Q_{yy} & Q_{yz} \\ Q_{zx} & Q_{zy} & Q_{zz} \end{bmatrix} = -e\sum_k \begin{bmatrix} 3x_k^2 - r_k^2 & 3x_k y_k & 3x_k z_k \\ 3y_k x_k & 3y_k^2 - r_k^2 & 3y_k z_k \\ 3z_k x_k & 3z_k y_k & 3z_k^2 - r_k^2 \end{bmatrix}. \tag{3.3}$$

In our theoretical treatment, we will presume we are dealing with an alkali atom, and as such, we can ignore all but the outer valence electron when making theoretical calculations, as it is only the outer electron that will be making transitions to higher excited states [1, 3]. In this case, we treat $\mathbf{r}$ as the position of the outer electron, whose quadrupole moment is simply

$$Q_{ij} = -e\left(3r_i r_j - \delta_{ij}r^2\right) = -e\begin{bmatrix} 3x^2 - r^2 & 3xy & 3xz \\ 3yx & 3y^2 - r^2 & 3yz \\ 3zx & 3zy & 3z^2 - r^2 \end{bmatrix}. \tag{3.4}$$

One can write this in terms of usual spherical coordinates, which can then be decomposed into the spherical harmonics, and thus, spherical tensors, where we'll first define $T_q^{(k)} = r^2 Y_k^q(\theta, \phi)$). Doing so allows us to decompose the quadrupole moment into terms relying solely on $T_q^{(2)}$ for some order q. These terms are

$$
\begin{aligned}
Q_{ij}^{(q=\pm 2)} &= \sqrt{\frac{6\pi}{5}} \begin{bmatrix} T_{\pm 2}^{(2)} & \mp i T_{\pm 2}^{(2)} & 0 \\ \mp i T_{\pm 2}^{(2)} & -T_{\pm 2}^{(2)} & 0 \\ 0 & 0 & 0 \end{bmatrix}, \\
Q_{ij}^{(q=\pm 1)} &= \sqrt{\frac{6\pi}{5}} \begin{bmatrix} 0 & 0 & \mp T_{\pm 1}^{(2)} \\ 0 & 0 & i T_{\pm 1}^{(2)} \\ \mp T_{\pm 1}^{(2)} & i T_{\pm 1}^{(2)} & 0 \end{bmatrix}, \\
Q_{ij}^{(q=0)} &= \sqrt{\frac{4\pi}{5}} \begin{bmatrix} -T_0^{(2)} & 0 & 0 \\ 0 & -T_0^{(2)} & 0 \\ 0 & 0 & 2T_0^{(2)} \end{bmatrix},
\end{aligned}
\tag{3.5}
$$

where $Q_{ij} = -e \sum_q Q_{ij}^{(q)}$. We can define a set of 'basis' matrices as

$$
\begin{aligned}
u_{ij}^{(\pm 2)} &= \frac{1}{2} \begin{bmatrix} 1 & \mp i & 0 \\ \mp i & -1 & 0 \\ 0 & 0 & 0 \end{bmatrix}, \\
u_{ij}^{(\pm 1)} &= \frac{1}{2} \begin{bmatrix} 0 & 0 & \mp 1 \\ 0 & 0 & i \\ \mp 1 & i & 0 \end{bmatrix}, \\
u_{ij}^{(0)} &= \frac{1}{\sqrt{6}} \begin{bmatrix} -1 & 0 & 0 \\ 0 & -1 & 0 \\ 0 & 0 & 2 \end{bmatrix},
\end{aligned}
\tag{3.6}
$$

which have the properties $u_{ij}^{(q)} = u_{ji}^{(q)}$, $u_{ij}^{(q)} = (-1)^q u_{ij}^{(-q)}$, $\sum_{ij} u_{ij}^{(q)} u_{ij}^{(q')} = \delta_{qq'}$, and $\sum_i u_{ii}^{(q)} = 0$. We can then use this to define the quadrupole moment

$$
Q_{ij} = -e2\sqrt{\frac{6\pi}{5}} \sum_q u_{ij}^{(q)} T_q^{(2)}. \tag{3.7}
$$

For ease of reading, we can redefine $T_q^{(2)}$ as $T_q^{(2)} = 2\sqrt{\frac{6\pi}{5}} r^2 Y_2^q(\theta, \phi)$, yielding

$$
Q_{ij} = -e \sum_q u_{ij}^{(q)} T_q^{(2)}. \tag{3.8}
$$

Which is the same form for the quadrupole moment that was used in [49]. Thus, our interaction Hamiltonian can be written as

$$
H_{int} = \frac{e}{6} \sum_q T_q^{(2)} \partial E^{(q)}, \tag{3.9}
$$

where, I've defined

$$\partial E^{(q)} = \sum_{ij} u_{ij}^{(q)} \frac{\partial E_j}{\partial r_i}, \tag{3.10}$$

as the electric field q gradient, and is a quantity that is partially responsible for the strength of a $\Delta M = q$ transition due to the electric field gradient.

Since the only nonzero matrix elements of $u_{ij}^{(\pm 2)}$ are u_{xx}, u_{xy}, u_{yx} and u_{yy}, we can see that the $\partial E^{(\pm 2)}$ quantity is due to gradients of the spatial profile of the EM field in the transverse plane. Similarly, $u_{ij}^{(0)}$ has nonzero matrix elements u_{ii} for $i \in \{x, y, z\}$, and since $\partial E_i / \partial z = 0$ for a paraxial beam, we have that the $\partial E^{(0)}$ quantity is also due solely to transverse gradients. If $\mathbf{E}$ is a laser field and we've chosen our coordinates such that the z-axis lies in the direction of the beam's propagation, then this corresponds to the gradient of the beam's shape in the xy-plane. The value $\partial E^{(\pm 1)}$ is due to gradients in the propagation direction of the spatial profile of the EM field – and if $\mathbf{E}$ describes a laser beam, this corresponds to gradients in the field's propagation direction.

Thus, **shaping the EM field mode will directly lead to a change in the coupling strength of certain quadrupole transitions**. This is an important point, and one that has until recently gone ignored by most of the spectroscopic community. By simply affecting the shape of an incident laser beam, we have a way of increasing (or decreasing) the quadrupole coupling strength between two atomic states, and this is incredibly simple to do with something like an SLM. This allows us to explore new avenues of research in spectroscopy.

3.1.2 Quadrupole selection rules

Consider a spherical tensor $T_q^{(k)}$ (discussed in Section 2.4), where again we have the restrictions

$$k \geq 0, \quad -k \leq q \leq k, \quad k, q \in \mathbb{Z} \tag{3.11}$$

on the indices. Consider the matrix element of this tensor formed by that of an excited atomic state $|n'\, J'\, M'\rangle$ and lower ground state $|n\, J\, M\rangle$. It should be noted that capital letters indicate total angular momentum quantities, while lowercase represent uncoupled angular momenta quantities (e.g. L is the total electron OAM, while l is the OAM of a single electron). The Wigner-Eckart theorem from (2.72) tells us that this matrix element is

$$\langle n'\, J'\, M' | T_q^{(k)} | n\, J\, M \rangle = (-1)^{2k} \langle n'\, J' || \mathbf{T}^{(k)} || n\, J \rangle \left\langle J'\, M' \middle| J\, M; k\, q \right\rangle, \tag{3.12}$$

where $\langle n'\, J' || \mathbf{T}^{(k)} || n\, J \rangle$ is an M-independent reduced matrix element, and $\langle J'\, M' | J\, M; k\, q \rangle$ is a Clebsch-Gordon (CG) coefficient. Now for the CG coefficient to potentially be non-zero, the parameters within it must adhere to a number of conditions, namely:

$$|J - k| \leq J' \leq J + k, \tag{3.13}$$

$$M + q = M', \tag{3.14}$$

where (3.13) is the triangular condition, and (3.14) is due to angular-momentum conservation.

It's clear then that q represents the change in M between the excited state and ground state, so that $q = \Delta M = M' - M$. The degree k represents the possible angular momentum change in an atomic transition. For example, in a dipole transition we have $k = 1$ from (2.73), while in a quadrupole transition we have $k = 2$ from (3.8). To further illustrate that k represents the possible angular momentum change, consider a case where $k = 1$ and $J = 0$: the only valid transition is for $J' = 1$ – which is just an s to p (or p to d, d to f, etc) transition. If $k = 1$ and $J = 1$, then J' could range from 0, 1, or 2, but one should take care when $J' = 1 = J$ as this is forbidden when $M' = M = 0$ (this is due to conservation of angular momentum, the atom must absorb the spin of the photon). One should also take care to not flip the spin of an electron in an atomic transition as this is a magnetic transition only and is electrically forbidden.

An easy way to mathematically formalise the above paragraph is through the use of Wigner 6-j symbols – which represent a transformation between two different ways of coupling three angular momenta (in this case, the electron spin $\mathbf{S}$, it's OAM $\mathbf{L}$, and the photon's AM represented as $\mathbf{k}$). We apply this to the reduced matrix element, and allows us to write the fine-structure matrix element in terms of reduced matrix element that only involves the quantum number l. This states

$$\langle n'\, J'||\mathbf{T}^{(k)}||n\, J\rangle = \langle n'\, L'||\mathbf{T}^{(k)}||n\, L\rangle\,(-1)^{J+L'+k+S}\sqrt{(2J+1)(2L'+1)}\begin{Bmatrix} L' & L & k \\ J & J' & S\end{Bmatrix}. \tag{3.15}$$

For more on the Wigner 6-j symbol, see [3].

Fine Structure

The electric dipole fine-structure selection rules are (for $k = 1$) represented in Table 3.1. It should be noted that in these tables that commas represent 'or'. We're also using $\Delta J = J' - J$, $\Delta M = M' - M$ and so on.

Rule	Reason
$\Delta J = 0, \pm 1$	Dipole triangular condition
$\Delta M = q$	Conservation of angular momentum
$\Delta J \neq 0$ if $M' = M = 0$	Must absorb photon SAM
$S' = S$ and $m'_S = m_S$	Electric fields do not affect electron spin
$\Delta l = \pm 1$	Single electron dipole parity rule
if $\Delta L = \pm 1$ then $\Delta J \neq \mp 1$	Extension of triangular condition when $S = 1/2$

TABLE 3.1: Electric dipole fine-structure selection rules, with a brief reason for the rule's existence.

From (3.8), we see that the $Q_{ij} \sim T^{(2)}_q$. So for quadrupole coupling, $k = 2$. This corresponds to the photon having two units of angular momentum. One unit of AM is from the photon's intrinsic SAM, brought about by it's polarization. Another unit comes from it's OAM, which is caused in part by the fact that we are taking the

derivative of the electric field, as in (3.1). Angular momentum operators are linked to derivatives, as $\mathbf{L} = -i\hbar(\mathbf{r} \times \nabla)$, so this explains the origin of an extra unit of AM in quadrupole interactions.

By examining the properties of the CG coefficient $\langle J'\, M'|J\, M; 2\, q\rangle$, as well as the decomposition relation in (3.15), we can derive the quadrupole selection rules, given in Table 3.2.

Rule	Reason
$\Delta J = 0, \pm 1, \pm 2$	Quadrupole triangular condition
$\Delta M = q$	Conservation of angular momentum
$\Delta J \neq \pm 1$ if $M' = M = 0$	Must absorb photon SAM and OAM
$S' = S$ and $m'_S = m_S$	Electric fields do not affect electron spin
$\Delta l = 0, \pm 2$	Single electron quadrupole parity rule
if $\Delta L = 0$ then $\Delta J \neq \pm 2$	Triangular condition when $S = 1/2$
if $\Delta L = \pm 1$ then $\Delta J \neq \mp 1, \mp 2$	Triangular condition when $S = 1/2$
if $\Delta L = \pm 2$ then $\Delta J \neq 0$	Triangular condition when $S = 1/2$

TABLE 3.2: Electric quadrupole fine-structure selection rules, with a brief reason for the rule's existence. The 3rd and 2nd to last rules must have $L \neq 0$ and $L' \neq 0$.

Some noticeable differences can be spotted between Table 3.1 and Table 3.2. In quadrupole transitions, $\Delta J = \pm 2$ and $\Delta L = \pm 2$ are possible, and thus so is $\Delta M = \pm 2$. The parity rule also changes from $\Delta l = \pm 1$ for dipole transitions to $\Delta l = 0, \pm 2$ for quadrupole transitions, due to the fact that $Q_{ij} \sim r^2$ and thus can only couple atomic states with even parity.

It should be noted that the 2nd to last rule in Table 3.2 requires at least three electrons in order to become useful. As we will be dealing with an alkali atom, and assuming that only the valence electron will be of importance, this rule will not apply.

The quadrupole selection rules we derived in Table 3.2 match with previously published theoretical derivations. The single electron Δl rule can be found in [57], while textbook references on the other selection rules can be found in [58].

Hyperfine Selection Rules

Hyperfine transitions involve a ground state $|n\, F\, M_F\rangle$ and excited state $|n'\, F'\, M'_F\rangle$ where $\mathbf{F}$ is the total angular angular momentum of the atomic system, with $\mathbf{F} = \mathbf{J} + \mathbf{I}$ where $\mathbf{I}$ is the nuclear spin. It's assumed that the transition is driven by a field that can be described by the spherical tensor $T_q^{(k)}$, where $k = 1$ for dipole fields and $k = 2$ for quadrupole fields.

The dipole selection rules are given in Table 3.3, while the quadrupole hyperfine selection rules are given in Table 3.4. The only major differences between the dipole and quadrupole hyperfine rules is that the ΔF value can reach ± 2 for quadrupole transitions (and thus, the ΔM_F value can also reach ± 2 in quadrupole transitions).

Since these selection rules are a simple extension of the fine structure selection rules, it's rare to explicitly find them stated within the literature. However, the dipole

Rule	Reason
$\Delta F = 0, \pm 1$	Dipole triangular condition
$\Delta M_F = q$	Conservation of angular momentum
$\Delta F \neq 0$ if $M'_F = M_F = 0$	Photon SAM must be absorbed
$\Delta I = 0$ and $\Delta m_I = 0$	Electric-dipole transitions effect the electron only

TABLE 3.3: Dipole hyperfine selection rules.

Rule	Reason
$\Delta F = 0, \pm 1, \pm 2$	Quadrupole triangular condition
$\Delta M_F = q$	Conservation of angular momentum
$\Delta F \neq \pm 1$ if $M'_F = M_F = 0$	Photon SAM and OAM must be absorbed
$\Delta I = 0$ and $\Delta m_I = 0$	Electric-quadrupole transitions effect the electron only

TABLE 3.4: Quadrupole hyperfine selection rules.

hyperfine selection rules can be found in [3] and agree with our derived selection rules. The quadrupole rules can be found in [49] (though are stated more as a matter of fact in paragraph form rather than explicitly derived), and also agree with our reported results.

3.1.3 Effect of an external magnetic field on quadrupole transitions

Typically in dipole transitions, applying a uniform magnetic field will determine the z-axis of the experiment. This is due to the Zeeman effect, which splits the magnetic sublevels of an atomic state, works out be conveniently related to the operator J_z if we define the z axis to align with our magnetic field such that $\mathbf{B} = B\hat{\mathbf{z}}$. That is, our energy eigenstates correspond to the $|J\,M\rangle$ states, where $J_z\,|J\,M\rangle = \hbar M\,|J\,M\rangle$. In this case, working out the effect of the magnetic field relies on decomposing the electric field polarization components into the spherical basis (2.60). The net effect of this lies in the interaction matrix $H_{int} = -\mathbf{d}\cdot\mathbf{E}$, which in the spherical basis can be written as $H_{int} = E_0 \sum_q r_q \epsilon_q$, where $\mathbf{E} = E_0\hat{\boldsymbol{\epsilon}}$ and $r_q \sim T^{(1)}_q$ as from (2.62). Since we know that $\Delta M = q$ from our discussions above, we have that the $\epsilon_{\pm 1}$ components of the polarization vector $\hat{\boldsymbol{\epsilon}}$ correspond to circularly polarized light, while the ϵ_0 component corresponds to linearly polarized light. If we, say, rotate the magnetic field, the net effect of this on the theoretical calculations would be to change the relative strengths of each of the ϵ_q components, as a rotation of the magnetic field vector can be equivalently thought of as a rotation in the polarization of light.

For quadrupole transitions, note that Q_{ij} requires a choice of coordinate system in order to be defined. As in dipole transition case we choose the z-axis to be aligned with the magnetic field, thus maintaining consistency with our earlier choice of quantization axis, and allowing us to write the energy eigenstates simply as $|J\,M\rangle$.

Consider the system pictured in Fig. 3.1a. Here we've defined the z-axis as the direction of propagation of the light, the magnetic field $\mathbf{B}$ is rotated from the z-axis by an angle $\theta_B\hat{\mathbf{y}}$ and sits in the xz plane, while the polarization of the light $\hat{\boldsymbol{\epsilon}}$ is at an angle $\phi_\epsilon\hat{\mathbf{z}}$ from the x-axis and is confined to the xy plane. We also set the position of our atom to the origin point $\mathbf{r} = 0$.

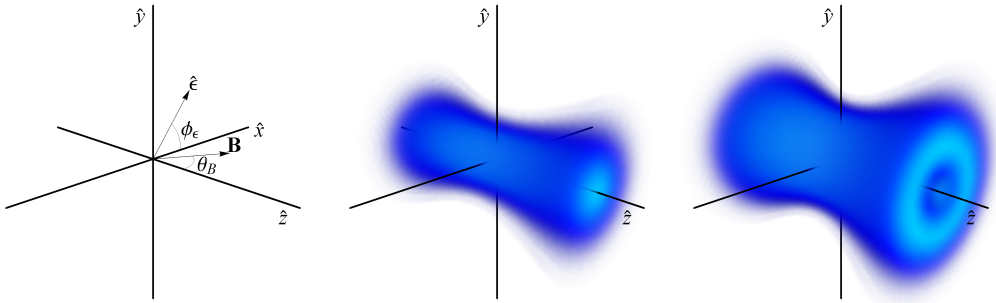

(A) (B) (C)

FIGURE 3.1: Diagram of (a) the polarization vector $\hat{\boldsymbol{\epsilon}}$ and the magnetic field vector $\mathbf{B}$ in our axis where the EM field propagates along the z-axis, (b) the intensity of an LG beam from (2.6) with $\ell = 0$, and (c) the intensity of an LG beam from (2.6) with $\ell = 1$. The colour of our beams is such that cyan represents a higher intensity than blue.

It's clear that the (x, y, z) basis would not be a good basis in which to describe the Q_{ij} matrix. Instead, we define the quadrupole moment in terms of the coordinates (x', y', z') where

$$\mathbf{r}' = \begin{bmatrix} x' \\ y' \\ z' \end{bmatrix} = \begin{bmatrix} \cos\theta_B & 0 & -\sin\theta_B \\ 0 & 1 & 0 \\ \sin\theta_B & 0 & \cos\theta_B \end{bmatrix} \begin{bmatrix} x \\ y \\ z \end{bmatrix} = R(\theta_B)\mathbf{r} \tag{3.16}$$

where $\mathbf{r}'$ is a position vector in the new coordinate system, $\mathbf{r}$ is in the old coordinate system, and $R(\theta_B\hat{\mathbf{y}})$ is a rotation matrix about the $\hat{\mathbf{y}}$ axis. This new coordinate system represents a rotated frame where the z'-axis aligns with the magnetic field, that is $\mathbf{B} = B\hat{\mathbf{z}}'$. In this coordinate system, we'd have

$$Q_{ij} = -e\left(3r'_i r'_j - \delta_{ij} r^2\right) \tag{3.17}$$

and

$$H_{int} = \frac{e}{6} \sum_q T_q^{(2)} \partial E^{(q)}, \tag{3.18}$$

where we now have

$$\partial E^{(q)} = \sum_{ij} u_{ij}^{(q)} \frac{\partial E'_j}{\partial r'_i} \tag{3.19}$$

which is in terms of E'_j (the EM field expressed in terms of the new (x', y', z') coordinates) and r'_i. It is often very inconvenient to use the E'_j quantity as the $\mathbf{E}$ field is more succinctly defined in the (x, y, z) basis. To calculate this, first note that for any vector field $\mathbf{E} = E\hat{\boldsymbol{\epsilon}}$, the matrix $\partial E_j/\partial r_i$ can be written as

$$\frac{\partial E_j}{\partial r_i} = (\boldsymbol{\nabla} E)\hat{\boldsymbol{\epsilon}}^{\mathrm{T}} \tag{3.20}$$

where $\hat{\boldsymbol{\epsilon}}^{\mathrm{T}}$ is the transpose of the unit vector $\hat{\boldsymbol{\epsilon}}$. Also note that we can transform between $\partial E_j/\partial r'_i$ (in the new coord system) to a matrix $\partial E_j/\partial r_i$ (in the old coordinate

system) by

$$\frac{\partial E_j}{\partial r'_i} = J\frac{\partial E_j}{\partial r_i}, \quad J = \frac{\partial r_j}{\partial r'_i}, \tag{3.21}$$

where J is known as the Jacobian of the transformation. In this case, $J = R(\theta_B)$. Combining this with the fact that $\mathbf{E}' = E(R(\theta_B))\hat{\boldsymbol{\epsilon}} = E\hat{\boldsymbol{\epsilon}}'$ we have (after some manipulation) that

$$\frac{\partial E'_j}{\partial r'_i} = R\frac{\partial E_j}{\partial r_i}R^{\mathrm{T}}, \tag{3.22}$$

or in index notation

$$\frac{\partial E'_j}{\partial r'_i} = \sum_{qp} R_{ip}\frac{\partial E_q}{\partial r_p}R_{jq}. \tag{3.23}$$

This will be applied in the next section as we study some examples of particular beams.

3.1.4 Quadrupole excitations in regions of zero-field intensity

Consider a Laguerre-Gauss beam with $\ell = 1$ in a region close to the beam's centre. We can describe this beam with the field amplitude $U_{\ell p}$ field from (2.6), and the electric field vector $\mathbf{E}$ to first order in the radial coordinate r by

$$\begin{aligned} U_{10} &= 2E_0\sqrt{\frac{1}{\pi}}\frac{r}{w_0}e^{i\phi}, \\ \mathbf{E} &= U_{10}\hat{\boldsymbol{\epsilon}}. \end{aligned} \tag{3.24}$$

Using Fig. 3.1a and the quantities derived in the section above we can calculate the $\partial E'_j/\partial r'_i$ matrix as

$$\left.\frac{\partial E'_j}{\partial r'_i}\right|_{\mathbf{r}'=0} = 2E_0\sqrt{\frac{1}{\pi}}\frac{1}{w_0}\begin{bmatrix} \cos^2\theta_B\cos\phi_\epsilon & \cos\theta_B\sin\phi_\epsilon & \sin\theta_B\cos\theta_B\cos\phi_\epsilon \\ i\cos\theta_B\cos\phi_\epsilon & i\sin\phi_\epsilon & i\sin\theta_B\cos\phi_\epsilon \\ \sin\theta_B\cos\theta_B\cos\phi_\epsilon & \sin\theta_B\sin\phi_\epsilon & \sin^2\theta_B\cos\phi_\epsilon \end{bmatrix}. \tag{3.25}$$

Thus, our $\partial E^{(q)}$ values can be calculated as

$$\begin{aligned} \partial E^{(\pm 2)} &= E_0\sqrt{\frac{1}{\pi}}\frac{1}{w_0}\left(\cos^2\theta_B\cos\phi_\epsilon \pm \cos\theta_B e^{-i\phi_\epsilon} - i\sin\phi_\epsilon\right), \\ \partial E^{(\pm 1)} &= E_0\sqrt{\frac{1}{\pi}}\frac{1}{w_0}\left(\mp\sin 2\theta_B\cos\phi_\epsilon - \sin\theta_B e^{-i\phi_\epsilon}\right), \\ \partial E^{(0)} &= E_0\sqrt{\frac{2}{3\pi}}\frac{1}{w_0}\left(3\sin^2\theta_B\cos\phi_\epsilon - e^{i\phi_\epsilon}\right). \end{aligned} \tag{3.26}$$

The corresponding matrix elements of the interaction Hamiltonian are given by (3.9), and can be calculated as

$$\begin{aligned}\langle n'\,J'\,M'|H_{int}|n\,J\,M\rangle &= \sum_q \langle n'\,J'\,M'|T_q^{(2)}\partial E^{(q)}|n\,J\,M\rangle \\ &= \sum_q \partial E^{(q)}\,\langle n'\,J'||\mathbf{T}^{(2)}||n\,J\rangle\,\big\langle J'\,M+q\big|J\,M;2,q\big\rangle\,\delta_{M',M+q},\end{aligned} \tag{3.27}$$

where I've inserted the conservation of angular momentum rule for CG coefficients in the form of a Kronecker delta function.

These matrix elements can be non-zero for the correct choice of J and M, which means that atomic excitations can take place in this region (i.e. in the beam centre). However, we've evaluated these quantities at $\mathbf{r}' = 0$, which corresponds to $\mathbf{r} = 0$. This is a region of the beam that has zero field intensity, so this is **an excitation in the dark**, and is only possible because quadrupole transitions couple to the EM field's gradient (which is nonzero at it's centre) and not to the field's intensity.

3.1.5 Comparison of an OAM=1 beam to a Gaussian beam at the beam centre

We've already studied the $\ell = 1$ case above. For the $\ell = 0$ case of the Gaussian beam, pictured in Fig. 3.1b, we can expand the field amplitude $U_{\ell p}$ field from (2.6) and the electric field vector $\mathbf{E}$ to first order in the propagation direction$z$ to give

$$\begin{aligned}U_{00} &= E_0\sqrt{\frac{2}{\pi}}e^{ikz}, \\ \mathbf{E} &= U_{00}\hat{\boldsymbol{\epsilon}}.\end{aligned} \tag{3.28}$$

Following the same procedure as above, the $\partial E'_j/\partial r'_i$ matrix is given by

$$\left.\frac{\partial E'_j}{\partial r'_i}\right|_{\mathbf{r}'=0} = ikE_0\sqrt{\frac{2}{\pi}}\begin{bmatrix}-\sin\theta_B\cos\theta_B\cos\phi_\epsilon & -\sin\theta_B\sin\phi_\epsilon & -\sin^2\theta_B\cos\phi_\epsilon \\ 0 & 0 & 0 \\ \cos^2\theta_B\cos\phi_\epsilon & \cos\theta_B\sin\phi_\epsilon & \sin\theta_B\cos\theta_B\cos\phi_\epsilon\end{bmatrix}. \tag{3.29}$$

This leads to

$$\begin{aligned}\partial E^{(\pm 2)} &= ikE_0\frac{1}{2}\sqrt{\frac{2}{\pi}}(-\cos\theta_B\cos\phi_\epsilon \pm i\sin\phi_\epsilon)\sin\theta_B \\ \partial E^{(\pm 1)} &= ikE_0\frac{1}{2}\sqrt{\frac{2}{\pi}}(\mp\cos 2\theta_B\cos\phi_\epsilon + i\cos\theta_B\sin\phi_\epsilon), \\ \partial E^{(0)} &= ikE_0\frac{1}{2}\sqrt{\frac{3}{\pi}}\sin 2\theta_B\cos\phi_\epsilon\end{aligned} \tag{3.30}$$

which will lead to a similar form for the interaction matrix elements as in (3.27).

Now, we consider an s-d transition. Specifically, we'll consider the $J = 1/2$ and $J' = 5/2$ single electron transition between the s and d states, with $M = -1/2$ and

$M' = M + q$. From (3.27), we see that the only non-zero matrix elements of the interaction hamiltonian occur when $M' = M + q$, or when $\Delta M = q$. Table 3.5 and Fig. 3.2 compare the strength of the interaction matrix elements between an $\ell = 0$ and $\ell = 1$ beam for various values of ΔM, θ_B and ϕ_ϵ.

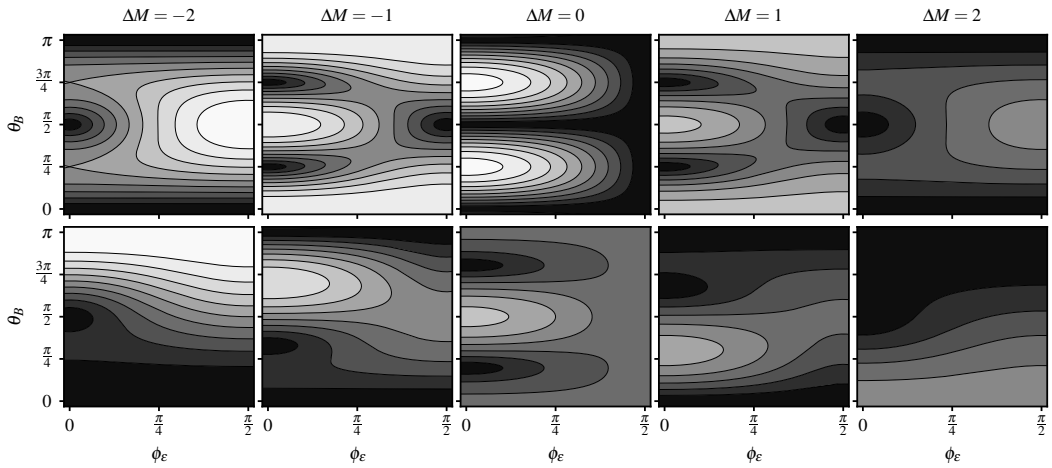

FIGURE 3.2: Relative strengths of a $|n, 1/2, -1/2\rangle$ to $|n', 5/2, -1/2 + \Delta M\rangle$ transition for an $\ell = 0$ (top row) and an $\ell = 1$ (bottom row) beam, for varying magnetic field angles θ_B and polarization angles ϕ_ϵ. The strengths of the plots are comparable throughout a row, but cannot be compared across columns. The colour values range from 0 (black) to the 1 (white) in steps of 0.1, where we've normalized the graphs such that 1 represents the maximum value of a transition.

ΔM	$\ell = 0$ beam	$\ell = 1$ beam
2	$\lvert(\cos\theta_B \cos\phi_\epsilon - i \sin\phi_\epsilon) \sin\theta_B\rvert$	$\frac{1}{\sqrt{2}}\lvert\cos^2\theta_B \cos\phi_\epsilon + \cos\theta_B e^{-i\phi_\epsilon} - i \sin\phi_\epsilon\rvert$
1	$\sqrt{2}\lvert\cos 2\theta_B \cos\phi_\epsilon - i \cos\theta_B \sin\phi_\epsilon\rvert$	$\lvert\sin 2\theta_B \cos\phi_\epsilon + \sin\theta_B e^{-i\phi_\epsilon}\rvert$
0	$\frac{3}{\sqrt{2}}\lvert\sin 2\theta_B \cos\phi_\epsilon\rvert$	$\lvert 3\sin^2\theta_B \cos\phi_\epsilon - e^{i\phi_\epsilon}\rvert$
-1	$2\lvert\cos 2\theta_B \cos\phi_\epsilon + i \cos\theta_B \sin\phi_\epsilon\rvert$	$\sqrt{2}\lvert\sin 2\theta_B \cos\phi_\epsilon - \sin\theta_B e^{-i\phi_\epsilon}\rvert$
-2	$\sqrt{5}\lvert(\cos\theta_B \cos\phi_\epsilon + i \sin\phi_\epsilon) \sin\theta_B\rvert$	$\sqrt{\frac{5}{2}}\lvert\cos^2\theta_B \cos\phi_\epsilon - \cos\theta_B e^{-i\phi_\epsilon} - i \sin\phi_\epsilon\rvert$

TABLE 3.5: Relative transition strength comparison between an $\ell = 0$ beam to an $\ell = 1$ beam from (3.30) and (3.26) respectively, evaluated at the centre of the transverse beam profile. All the values represented here are multiplied by a factor $E_0\sqrt{2/5\pi}\,\langle n'\,5/2||\mathbf{T}^{(2)}||n\,1/2\rangle$, as well as $k/2$ and $1/w_0$ for the $\ell = 0$ and $\ell = 1$ beams, respectively. These values relate to the Rabi frequency of the transition, ignoring phase. These are the quantities are plotted in Fig. 3.2.

From Table 3.5 we can see that for the $\ell = 0$ beam that the strength of the $\Delta M = q$ and $\Delta M = -q$ transitions are the same up to a multiplicative factor induced by the CG coefficient. The transition strengths are also symmetric about the $\theta_B = \pi/2$ axis for the $\ell = 0$ beam. For the $\ell = 1$ beam, we can see from Fig. 3.2 that a reflection (multiplied by a constant from the CG coefficient) about the $\theta_B = \pi/2$ axis occurs we take $\Delta M = q$ to $\Delta M = -q$.

The easiest transitions to understand are those that occur when $\theta_B = 0$. Here, the polarization angle ϕ_ϵ plays no role in the transitions, as our atomic system is axially symmetric when $\theta_B = 0$. From Fig. 3.2 we can see that a $\Delta M = 2$ and $\Delta M = 0$ transition is possible when our beam posseses OAM ($\ell = 1$). This is due to the fact that the OAM and the SAM of the photon will add, which both project onto the z-axis, and can either be in the same or opposite directions leading to a $\Delta M = 2$ or $\Delta M = 0$ transition, respectively. It's precisely because the OAM and SAM must be conserved in the atomic transition that the $\Delta M = \pm 1$ transitions cannot occur for OAM beams, but can occur when OAM is not present (i.e. $\ell = 0$). The same can be said for when $\theta_B = \pi$, only here it's as if the z-axis has been reflected through the xy-plane, thus causing the OAM in the beam (if any) to effectively reverse.

For non-zero θ_B, the analysis becomes more complicated. A good quantisation axis for the atom will always have the z axis defined by the magnetic field, as the corresponding energy eigenstates can be described by a $|J\, M_J\rangle$ state. However, in this coordinate system, defining the OAM of the electric field becomes tricky. The simplest coordinate system in which to calculate the EM field's OAM is one where z aligns with the propagation direction of our beam. In other words, the OAM of the electric and the AM of our atomic state misalign when $\theta_B \neq 0$, causing a more complicated coupling scheme to arise.

Similar results have been derived in a theoretical paper found in [44], however, we obtain results that somewhat differ due to some differences in our derivation. Instead of using the quadrupole interaction derived in (2.20), the paper [44] used the dipole interaction $-\mathbf{d}\cdot\mathbf{E}$, where they evaluated the electric field $\mathbf{E}$ at the position of the electron (instead of at the position of the centre of mass of the atom as we've done here). It's a subtle difference, but one that can carry with it some important implications. For example, in [44] it's found that the dot product of $\mathbf{d}\cdot\mathbf{E}$ can be written as a sum of terms $T^{(2)}_q$, $T^{(1)}_q$, and $T^{(0)}_0$, whereas our quadrupole moment Q_{ij} was shown to rely solely upon $T^{(2)}_q$, as in (3.8). To my understanding, an external electric field interacts with the multipolar moments (dipole, quadrupole, etc) of an atom, and is written in a coordinate system completely separate to that of the electron's position. This understanding appears to be backed up, as another theoretical paper [49] used this line of reasoning when examining quadrupole transitions in rubidium.

3.1.6 Coupling strength outside of the beam centre

In the above sections our analysis relied on the fact that the atom was located at the centre of the beam's axis, but we can consider other locations for the position of the atom. This is just a matter of evaluating the gradient of the electric field, or more specifically on the value $\partial E^{(q)}$ from (3.10). We've seen from the above analysis that atomic transitions are only possible for $\Delta M = q$ and that the strength of these transitions is related to $\left|\partial E^{(q)}\right|$. In the case of an LG beam, this plotted in Fig. 3.1a for the case where $\theta_B = \phi_\epsilon = 0$.

We can see that the results predicted in Fig. 3.2 and Table 3.5 are qualitatively consistent with those shown in Fig. 3.3 when considering the centre of the beam. From Fig. 3.2 we see that when $\ell = 0$, there are no $\Delta M = \pm 2$ or $\Delta M = 0$ transitions when $\theta_B = \phi_\epsilon = 0$, and this is confirmed in Fig. 3.3. We can also see from Fig. 3.2 that

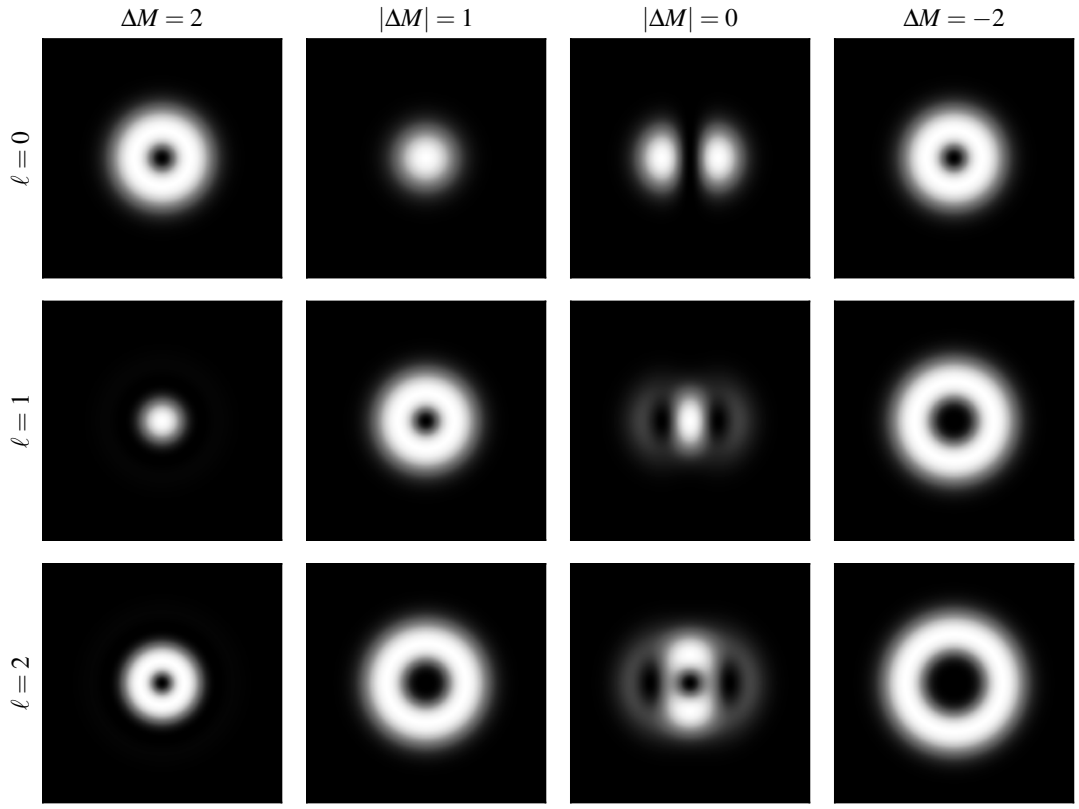

FIGURE 3.3: Transverse plots of the normalized $\left|\partial E^{(q)}\right|$ value for an LG beam of topological charge $\ell = 0$, 1, and 2. We've set the magnetic field vector to be aligned along the axis of the beam's propagation direction, and have set the polarization vector $\hat{\epsilon}$ to be aligned to the x-axis, which here is the horizontal axis. Note that since $\partial E^{(\pm 1)} \sim kE$, we have that the $|\Delta M| = 1$ is related to a beam's transverse intensity profile. The colour scheme here is a simple linear map from 0 (black) to 1 (white). Each individual plot has been normalized, and thus the strengths are not comparable between any two plots.

when $\ell = 1$, and when the atom is at the centre of the beam, there are no $\Delta M = \pm 1$ transitions, and this is confirmed again in Fig. 3.3.

What might be surprising to some is that $\Delta M = \pm 2$ transitions are possible even when the beam possesses no OAM ($\ell = 0$). A $\Delta M = \pm 2$ fundamentally implies that the photon must possess some OAM, otherwise the conservation of angular momentum selection rule is violated. So where is this OAM coming from? This dilemma is easily resolved if one recalls that the OAM of any system (even classical) requires the choice of a point of origin about which the OAM is measured from. So it's true that an $\ell = 0$ beam has no OAM if the point of reference is in the centre of the beam. However, any other point of reference will possess non-zero OAM, thus allowing $\Delta M = \pm 2$ transitions to occur.

To the best of our knowledge, no plot similar to Fig. 3.3 has been seen in literature, so we have nothing with which to compare our results. However, obtaining this plot was little more than an application of our theoretical analysis made in Section 3.1, which itself was compared to the theoretical results of [49].

3.1.7 Transition strength comparison to dipole transitions

The two main quantities of interest in atomic physics are the Rabi frequency and the transition rate between two states. Both quantities rely on, essentially, the $\langle e|H_{int}|g\rangle$ matrix element. For dipole transitions, $H_{int} = -\mathbf{d}\cdot\mathbf{E} \sim r$, and so the matrix element $\langle e|H_{int}|g\rangle \sim r_a$ where r_a is the radius of the atom (typically around 0.3 nm). We'll ignore the other factors involved, and just calculate an order of magnitude estimate.

For quadrupole transitions, we have $H_{int} = \sum Q_{ij}\partial_i E_j \sim \partial_i E_j$. For transitions involving OAM ($\ell = 1$) (3.26) gave the strength of the electric field derivative as roughly $\partial_i E_j \sim 1/w_0$. We also know that $Q_{ij} \sim r^2$. Thus, the matrix element is roughly $\langle e|H_{int}|g\rangle \sim r_a^2/w_0$, which is r_a/w_0 times the dipole transition strength. We can thus see that for OAM transitions, the smaller the beam width w_0, the stronger the transition. If we set w_0 to it's diffraction limited value of $w_0 = 2\lambda/\pi$, then $\langle e|H_{int}^{\ell=1}|g\rangle \sim \pi r_a^2/2\lambda$ so that an OAM transition is $\pi r_a/2\lambda \sim 1\times 10^{-3}$ times weaker than a dipole interaction if the beam is diffraction limited. In the case where $\ell = 0$, the strength of the derivative $\partial_i E_j \sim k = 2\pi/\lambda$. The matrix element is then $\langle e|H_{int}^{\ell=0}|g\rangle \sim 2\pi r_a^2/\lambda$, which is $2\pi r_a/\lambda \sim 4\times 10^{-3}$ times weaker than a dipole interaction.

The Rabi frequency is given in (2.44) and is directly related to the $\langle e|H_{int}|g\rangle$ matrix, thus the quadrupole Rabi frequency is around 10^{-3} times smaller than a dipole Rabi frequency. However, the transition rate, as given by the Einstein coefficients in (2.30) and (2.28), is related to $|\langle e|H_{int}|g\rangle|^2$, and thus a quadrupole transition rate is 10^{-6} times weaker than dipole transition rate.

Also note that even in the diffraction limited case, the strength of a $\ell = 0$ transition is approximately 4 times stronger than a $\ell = 1$ transition. This is due to the fact that the gradient in the z-direction of a laser field is, in general, always larger than the derivative in the xy-plane for a paraxial beam.

3.2 Experimental application of quadrupole coupling

3.2.1 Concerns from theoretical calculations

From our above theoretical analysis, it is clear that quadrupole couplings provide an interesting field of spectroscopy that has gone fairly unexplored, particularly in the context of structured light. Table 3.2 and Table 3.4 both provide new selection rules over their dipole counterparts, and Section 3.1.4 also showed that quadrupole excitations can occur in regions of zero field intensity, a concept which is completely foreign to the usual dipole transitions. We would like to test these theoretical predictions and explore new regimes of spectroscopy in a cost effective and easily accessible manner.

During the theoretical analysis of quadrupole coupling, a number of problems became apparent that would have presented some serious experimental difficulties. The first being the transition rate of quadrupole excitations is generally 10^{-6} times weaker than that of dipole transitions, and since the transition rate is related to the width of the transition as in (2.54), our linewidth would also be 10^{-6} times narrower

as well – dipole transitions typically have $\Gamma \sim 10^6$ Hz, so quadrupole transitions would have $\Gamma \sim 1$Hz. This makes for a transition that would be incredibly weak and very hard to pin down, requiring a very precise laser in order to properly resolve the quadrupole transition. The second problem was that we knew we wanted to perform our experiment on a gas cell, as this is a cost effective and readily available tool. Previous experiments have been performed on trapped ions [48] which have shown new selection rules for OAM laser beams, but trapping an ion can be an extremely difficult and expensive task.

To solve the problem of the very narrow linewidth, we needed to use an atom that had a high decay rate Γ, and thus a larger linewidth, in its quadrupole transition. One way we could cheat a larger decay rate is by using an atom that had a dipole transition in-between the quadrupole transition. A well known fact from theoretical calculations of multilevel systems is that the decay rate of a transition depends on the sum of all the decay rates from that state to any other state. So, if a p level existed in between an s and d level, then an electron in the d level would naturally decay to the p state, as this is a dipole decay, and since dipole decay rates are much larger than quadrupole decay rates, we have that the decay rate $\Gamma \approx \Gamma_{DP}$ with Γ_{DP} being the decay rate between the d and p state (we prove this later in this section). We also wanted an alkali atom as this would make the theoretical calculations much simpler. The three atoms that fit these requirements were rubidium, potassium and caesium. We chose potassium, as we also wanted to construct an external cavity laser diode (ECDL), and the laser diode we considered s to d transition in potassium (the Thorlabs L462P1400MM) was relatively cheaper and closer to the desired linewidth than the equivalent available diodes for rubidium, and much more intense than the available diodes for the caesium atom. Ultimately, we ended up not using the L462P1400MM diode as it was multimodal, but this was what guided our selection.

There are a number of ways to overcome the very weak coupling strength of quadrupole transitions. The first is to increase the intensity, or field amplitude of our light. We can do this simply by focusing the laser beam to a small waist. Another way of overcoming this is by increasing the particle density in our vapour cell. We can do this by heating the cell, which in turn would increase the vapour pressure, thus increasing our particle density. This would just provide more opportunities for our light to interact with the atoms in our sample. A drawback of heating the cell would be that it increases the linewidth of our measurements due to Doppler broadening. We can overcome this with a standard experimental technique, known as Doppler free saturated absorption spectroscopy, details of which can be found in [3, 59].

3.2.2 Three level model of potassium

In this section we idealise a potassium atom into a model containing only three levels. We do this in order to understand the underlying physics at play when we perform our experiment, and not to make any strict theoretical predictions on the actual transitions we will eventually see in our experiment. We refer now to Fig. 3.4 as the idealised three level model for potassium, where the energy levels between the $|s\rangle$ and $|d\rangle$ state is $\hbar\omega_d$ and that between the $|s\rangle$ and $|p\rangle$ is $\hbar\omega_p$, setting the ground energy level to be the s state.

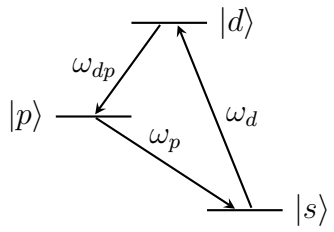

FIGURE 3.4: Three level model of potassium. We intend to excite from the $|s\rangle$ state to the $|d\rangle$ state. The state will then decay from the $|d\rangle$ state to the $|p\rangle$ state at a rate of Γ_{dp}, and from the $|p\rangle$ to the $|s\rangle$ state at a rate Γ_{ps}. There's also a decay from the $|d\rangle$ to the $|s\rangle$ state at a rate of Γ_{ds}, but this is typically small compared to Γ_{dp}.

The diagonal elements of the atomic Hamiltonian can then be written as

$$H_0 = \hbar\omega_d \left|d\right\rangle\!\left\langle d\right| + \hbar\omega_p \left|p\right\rangle\!\left\langle p\right| . \tag{3.31}$$

We wish to make an S to D transition in potassium while in the presence of a laser field described by $\mathbf{E}\cos(\omega t)$ with ω near ω_d. Now, an s to d transition has $\Delta L = 2$ transition, hence this is a quadrupole transition. Thus, we use the interaction Hamiltonian for quadrupole transitions, as given in (3.1) by

$$H_{int} = -\frac{1}{6}\sum_{ij} Q_{ij}\frac{\partial E_j}{\partial r_i}\cos(\omega t). \tag{3.32}$$

If we recognise the Rabi frequency from (2.44) as just being $\Omega_{eg} = \langle e|H_{int}|g\rangle/\hbar$ for a dipole interaction Hamiltonian (ignoring the time dependence), then the equivalent Rabi frequency for a quadrupole transition can be given by

$$\Omega_{eg} = -\frac{1}{6\hbar}\sum_{ij}\langle e|Q_{ij}|g\rangle\frac{\partial E_j}{\partial r_i}, \tag{3.33}$$

thus, the interaction Hamiltonian can be written as

$$H_{int} = \frac{\hbar}{2}(\Omega_{sp}\sigma_{sp} + \Omega_{sd}\sigma_{sd} + \Omega_{pd}\sigma_{pd})\left(e^{i\omega t} + e^{-i\omega t}\right) + c.c., \tag{3.34}$$

where I've defined the lowering operators σ_{ge} as $\sigma_{ge} = |g\rangle\langle e|$.

Since we've defined $\omega \approx \omega_d$, and with the time dependences of $\sigma_{sd} \sim e^{-i\omega_d t}$, $\sigma_{sp} \sim e^{-i\omega_p t}$, and $\sigma_{pd} \sim e^{-i(\omega_d-\omega_p)t}$ from (2.37), we can approximate H_{int} as

$$H_{int} \approx \frac{\hbar\Omega_{sd}}{2}\left(\sigma_{sd}e^{i\omega t} + \sigma_{sd}^{\dagger}e^{-i\omega t}\right). \tag{3.35}$$

The atomic Hamiltonian can then be written as

$$H = \hbar\omega_d \left|d\right\rangle\!\left\langle d\right| + \hbar\omega_p \left|p\right\rangle\!\left\langle p\right| + \frac{\hbar\Omega_{sd}}{2}\left(e^{i\omega t}\sigma_{sd} + e^{-i\omega t}\sigma_{sd}^{\dagger}\right). \tag{3.36}$$

We can make the RWA by using a transformation matrix

$$\begin{aligned} U &= \exp(i\omega t \left|d\right\rangle\!\left\langle d\right|) \\ &= \left|s\right\rangle\!\left\langle s\right| + \left|p\right\rangle\!\left\langle p\right| + \left|d\right\rangle\!\left\langle d\right| e^{i\omega t}, \end{aligned} \tag{3.37}$$

and applying the transformation rules from (2.41) to H, yielding the final Hamiltonian for the system, given by

$$H = -\hbar\Delta \left|d\right\rangle\!\left\langle d\right| + \hbar\omega_p \left|p\right\rangle\!\left\langle p\right| + \frac{\hbar\Omega}{2}\left(\sigma_{sd} + \sigma_{sd}^{\dagger}\right), \tag{3.38}$$

where $\Delta = \omega - \omega_d$ is the detuning of the laser and I have set $\Omega = \Omega_{sd}$ for convenience.

3.2.3 Dynamics of the three level model

The dynamics of an atomic system are neatly described by what is known as the atomic master equation, given in (2.47) by

$$\partial_t \rho = -\frac{i}{\hbar}[H, \rho] + \sum_i \Gamma_i \mathcal{D}\left[\sigma_i\right]\rho, \tag{3.39}$$

where σ_i corresponds to an element of the set of lowering operators $\{\sigma_{sd}, \sigma_{sp}, \sigma_{pd}\}$ with the corresponding decay rate Γ_i from $\{\Gamma_{ds}, \Gamma_{ps}, \Gamma_{dp}\}$. The Lindblad superoperator is given as $\mathcal{D}\left[\sigma_i\right]\rho$ and is defined in (2.48). Using our three-level model from (3.38), we receive a set of 4 coupled differential equations describing the main dynamics of the system, given by

$$\begin{aligned} \partial_t \rho_{dd} &= \frac{i}{2}\Omega(\rho_{ds} - \rho_{sd}) - (\Gamma_{ds} + \Gamma_{dp})\rho_{dd}, \\ \partial_t \rho_{pp} &= \Gamma_{dp}\rho_{dd} - \Gamma_{ps}\rho_{pp}, \\ \partial_t \rho_{ss} &= -\frac{i}{2}\Omega(\rho_{ds} - \rho_{sd}) + \Gamma_{ds}\rho_{dd} + \Gamma_{ps}\rho_{pp}, \\ \partial_t \rho_{ds} &= i\Delta\rho_{ds} - \frac{i}{2}\Omega(\rho_{ss} - \rho_{dd}) - \frac{1}{2}(\Gamma_{ds} + \Gamma_{dp})\rho_{ds}, \end{aligned} \tag{3.40}$$

as well as a set of two coupled equations which describe the coherences between the undriven states, namely

$$\begin{aligned} \partial_t \rho_{dp} &= i(\Delta - \omega_p)\rho_{dp} - \frac{i}{2}\Omega\rho_{sp} - \frac{1}{2}(\Gamma_{ds} + \Gamma_{dp} + \Gamma_{ps})\rho_{dp}, \\ \partial_t \rho_{ps} &= i\omega_p\rho_{ps} + \frac{i}{2}\Omega\rho_{pd} - \frac{1}{2}\Gamma_{ps}\rho_{ps}. \end{aligned} \tag{3.41}$$

For the most part, the time dependencies are on scales that are too short to notice (typically nanoseconds). For this reason, we look to steady state solutions of the above equations.

In the steady state where $\partial_t \to 0$, we can immediately solve for ρ_{pp} from the steady state condition on $\partial_t \rho_{pp} = 0$. This yields

$$\rho_{pp} = \frac{\Gamma_{dp}}{\Gamma_{ps}} \rho_{dd}, \tag{3.42}$$

thus from $\mathrm{Tr}[\rho] = \rho_{ss} + \rho_{pp} + \rho_{dd} = 1$ we have

$$\rho_{ss} = 1 - \left(1 + \frac{\Gamma_{dp}}{\Gamma_{ps}}\right) \rho_{dd}, \tag{3.43}$$

thus

$$\rho_{ss} - \rho_{dd} = 1 - \left(2 + \frac{\Gamma_{dp}}{\Gamma_{ps}}\right) \rho_{dd}. \tag{3.44}$$

From the steady state condition $\partial_t \rho_{ds} = 0$, and using (3.44), we find that the coherence between the s and d state is given by

$$\begin{aligned} \rho_{sd} &= \frac{i\Omega \left[1 - \left(2 + \frac{\Gamma_{dp}}{\Gamma_{ps}}\right) \rho_{dd}\right]}{2i\Delta + \Gamma_{ds} + \Gamma_{dp}} \\ &= \frac{\Omega(2\Delta + i\Gamma_d)}{4\Delta^2 + \Gamma_d^2} \left[1 - \left(2 + \frac{\Gamma_{dp}}{\Gamma_{ps}}\right) \rho_{dd}\right], \end{aligned} \tag{3.45}$$

where I've defined $\Gamma_d = \Gamma_{ds} + \Gamma_{dp}$ as the total decay rate of the $|d\rangle$ state. We can thus calculate $\rho_{ds} - \rho_{sd}$ as we have $\rho_{ds} = \rho_{sd}^*$. This yields

$$\rho_{ds} - \rho_{sd} = -\frac{2i\Omega\Gamma_d}{4\Delta^2 + \Gamma_d^2} \left[1 - \left(2 + \frac{\Gamma_{dp}}{\Gamma_{ps}}\right) \rho_{dd}\right]. \tag{3.46}$$

Thus, from the $\partial_t \rho_{dd} = 0$ steady state condition in (3.40), we can calculate the final expression for ρ_{dd} as

$$\rho_{dd} = \frac{\Omega^2/\Gamma_d^2}{1 + \left(\frac{2\Delta}{\Gamma_d}\right)^2 + \frac{2\Omega^2}{\Gamma_d^2}\left(1 + \frac{\Gamma_{dp}}{2\Gamma_{ps}}\right)}, \tag{3.47}$$

which is very similar to the expression of the excited state in the two level case from (2.50) (and would be equivalent to the two level system if $\Gamma_{dp}/\Gamma_{ps} = 0$).

3.2.4 Saturation intensity and absorption cross-section

If we consider a laser field of intensity I being absorbed through a volume of gas consisting of N particles, then the energy transferred from the beam to the gas is given by

$$E_{transfer} = \underbrace{N\rho_{ss}\sigma(\omega)I}_{\text{Absorption}} - \underbrace{N\rho_{dd}\sigma(\omega)I}_{\text{Stimulated emission}}, \tag{3.48}$$

where σ is the absorption cross section. Conversely, the volume of gas will also undergo spontaneous emission, leading to an outflow of energy. This is characterised

as

$$\begin{aligned} E_{out} &= \underbrace{N\rho_{dd}\hbar(\omega_d - \omega_p)}_{d \text{ to } p} + \underbrace{N\rho_{dd}\hbar\omega_d}_{d \text{ to } s} + \underbrace{N\rho_{pp}\hbar\omega_p}_{p \text{ to } s} \\ &= N\rho_{dd}\hbar\omega_d\Gamma_d, \end{aligned} \tag{3.49}$$

where I used the fact that $\rho_{pp} = \rho_{dd}\Gamma_{dp}/\Gamma_{ps}$ and $\Gamma_d = \Gamma_{ds} + \Gamma_{dp}$. In a steady state system, the energy put into the gas should be equal to the energy flowing out of it, thus we have

$$N(\rho_{ss} - \rho_{dd})\sigma(\omega)I = N\rho_{dd}\hbar\omega_d\Gamma_d. \tag{3.50}$$

The absorption cross-section is then

$$\sigma(\omega) = \frac{\hbar\omega_d\Gamma_d}{I}\frac{\rho_{dd}}{\rho_{ss} - \rho_{dd}}. \tag{3.51}$$

Using the values for ρ_{ij} calculated above, we can easily determine σ to be

$$\begin{aligned} \sigma(\Delta) &= \frac{\hbar\omega_d\Gamma_d}{I}\frac{\Omega^2/\Gamma_d^2}{1 + \left(\frac{2\Delta}{\Gamma_d}\right)^2} \\ &= \sigma_0 g_H(\Delta), \end{aligned} \tag{3.52}$$

where g_H is the usual Lorentzian lineshape from (2.54) with a FWHM of $\Gamma_d = \Gamma_{ds} + \Gamma_{dp} \approx \Gamma_{dp}$. The maximum of cross-section occurs at $\Delta = 0$ by σ_0, and is given by

$$\begin{aligned} \sigma_0 &= \frac{\Omega^2\hbar\omega_d}{\Gamma_d I} \\ &= \frac{3\lambda^2}{2\pi}\frac{\Gamma_{ds}}{\Gamma_d}, \end{aligned} \tag{3.53}$$

which comes from the fact that I've identified the Einstein A_{eg} coefficient from (2.30) as

$$A_{eg} = \frac{\omega^3\hbar\Omega_{eg}^2}{3\pi\varepsilon_0 c^3|E_0|^2}, \tag{3.54}$$

and is a result of substituting (2.44) into (2.30). Since we're using $\Omega = \Omega_{ds}$ and $A_{ds} = \Gamma_{ds}$, and using $I = c\varepsilon_0|E_0|^2/2$ with $\omega = 2\pi c/\lambda$, we have

$$\Omega_{ds}^2 = \frac{3\lambda^3\Gamma_{ds}I}{4\pi^2\hbar c}, \tag{3.55}$$

which was then used to derive (3.53). We can see that the quadrupole cross-section (3.53) is largely the same as the dipole cross-section (2.56) but with a multiplicative factor Γ_{ds}/Γ_d. The total decay rate $\Gamma_d \approx \Gamma_{dp}$ is typically 10^3 to 10^6 times larger than Γ_{ds}, making the quadrupole cross section between 10^{-3} to 10^{-6} times smaller than the cross-section of a dipole transition, making it extremely difficult to excite the quadrupole transition.

To get the saturation intensity, note that we can use (3.50) to solve for the $(\rho_{ss} - \rho_{dd})$ quantity, where we use (3.44) to write ρ_{dd} in terms of $(\rho_{ss} - \rho_{dd})$. The final quantity

comes out to be

$$\rho_{ss} - \rho_{dd} = \frac{1}{1 + I/I_s}, \tag{3.56}$$

where

$$\begin{aligned} I_s &= \frac{\hbar\omega_d\Gamma_d}{2\sigma}\frac{1}{1+\frac{\Gamma_{dp}}{2\Gamma_{ps}}} \\ &= \frac{2\pi^2\hbar c\Gamma_d}{3\lambda^3}\frac{1}{1+\frac{\Gamma_{dp}}{2\Gamma_{ps}}}\frac{\Gamma_d}{\Gamma_{ds}} \end{aligned} \tag{3.57}$$

is the saturation intensity of the quadrupole transition, and is the same as the dipole saturation intensity (2.58) derived in the two level system, except with a multiplicative factor of α, where

$$\alpha = \frac{1}{1+\frac{\Gamma_{dp}}{2\Gamma_{ps}}}\frac{\Gamma_d}{\Gamma_{ds}}. \tag{3.58}$$

Since again, $\Gamma_d \approx \Gamma_{dp}$, which is typically 10^3 to 10^6 times larger than Γ_{ds}, so our quadrupole saturation intensity would be between 10^3 to 10^6 times that of a typical dipole's saturation intensity. If the beam is focused to a waist of ~ 100 μm, a dipole transition will typically only require a laser beam power on the order of 1 μW to cause saturation, so a quadrupole transition would need a beam power on the order of 1 mW to 1 W (then focused) in order to reach saturation intensity. This is quite easily achievable, as most lasers operate in the mW regime without much intervention.

4 External Cavity Diode Laser

4.1 Overview

An external cavity diode laser (ECDL) is a method of utilising a diode laser in order to create a highly-tunable single longitudinal mode laser. This is in contrast to an unmodified diode laser, which are typically very sensitive to temperature and current changes, and have large linewidths of approximately 100 MHz [60]. An ECDL is relatively inexpensive upgrade to a diode laser, providing narrower linewidths, a tunable output frequency, and temperature control.

Construction of an ECDL typically employs the use of a reflection grating operating in the Littrow configuration [60, 61]. This configuration places the reflection grating a distance d from the diode, and is angled such that the angle of incidence θ of a collimated source of laser diode light such that

$$\sin\theta = \frac{\lambda}{2D}, \tag{4.1}$$

where λ is the target output wavelength of the diode, and D is the linespacing of the grating. This allows the first order of diffracted light to be reflected directly back into the laser diode, promoting the laser to operate at the wavelength λ. The zeroth order beam, reflected from the grating, serves as the output beam.

This would typically mean that the output beam angle is dependent on the desired wavelength of a beam, but one can correct for this by constructing a mount whereby a change in the angle θ would also change the angle of a mirror from which the output beam is reflected [61]. The result is a laser where wavelength shifts corresponding to a change in incident angle $\Delta\theta$ will shift the horizontal position of the output beam by an amount $\Delta x = 2L\Delta\theta$, where L is the distance between the grating and mirror. For most practical tuning applications the shift Δx is on the order of nanometres, and is insignificant for most atomic physics applications.

Most ECDL's will mount a piezoelectric (PZT) disk behind the reflection grating. Applying a voltage across this will result in a change of the distance d between the laser diode and reflection, thus changing the cavity length of laser and ultimately the output wavelength. This can be used to fine tune the output wavelength, and even scan across a frequency band on the order of GHz [60]. Some ECDL designs add a second piezoelectric stack that can adjust the angle θ. This stack is typically used for large scale frequency adjustment on the order of 40 GHz [61, 62], but can be used in conjuction with the PZT disk behind the grating in order to extend the mode-hop free scan range of the laser to up to 35 GHz [62].

Temperature control of the laser diode is usually achieved by mounting the diode in some form of copper assembly. Peltier thermoelectric units are then attached to the copper assembly for heating or cooling, as required. Typically, the peltier coolers are operated with a PID controller, or similar feedback mechanism, in order to achieve thermal stability of the laser diode. It is desired that the temperature of the diode does not change under any circumstances, and usually remains in operation even when the laser is turned off.

4.2 Design and construction specifications

For this section, we refer to the diagram shown in Fig. 4.1. This contains a to-scale representation of the ECDL we constructed for our experiment. The grating and mirror are epoxied to the grating mount, which sits within a custom designed housing to provide protection against dust. The laser diode itself is mounted in a lens tube that is held within the copper mount, and is thermally isolated from the housing through the use of a plastic o-ring. A lens is also mounted within the lens tube that collimates the output of the laser diode. The copper block makes thermal contact with the lens tube and is temperature controlled through the use of the peltier units, which are connected to a PID temperature controller. The piezo plate and stack allow for fine or course control of the output frequency, respectively. Finally, large scale adjustments to the position of the grating mount can be made with three adjustment screws, accessible through holes in the back of the housing. Technical drawings of the ECDL are provided in Appendix A.

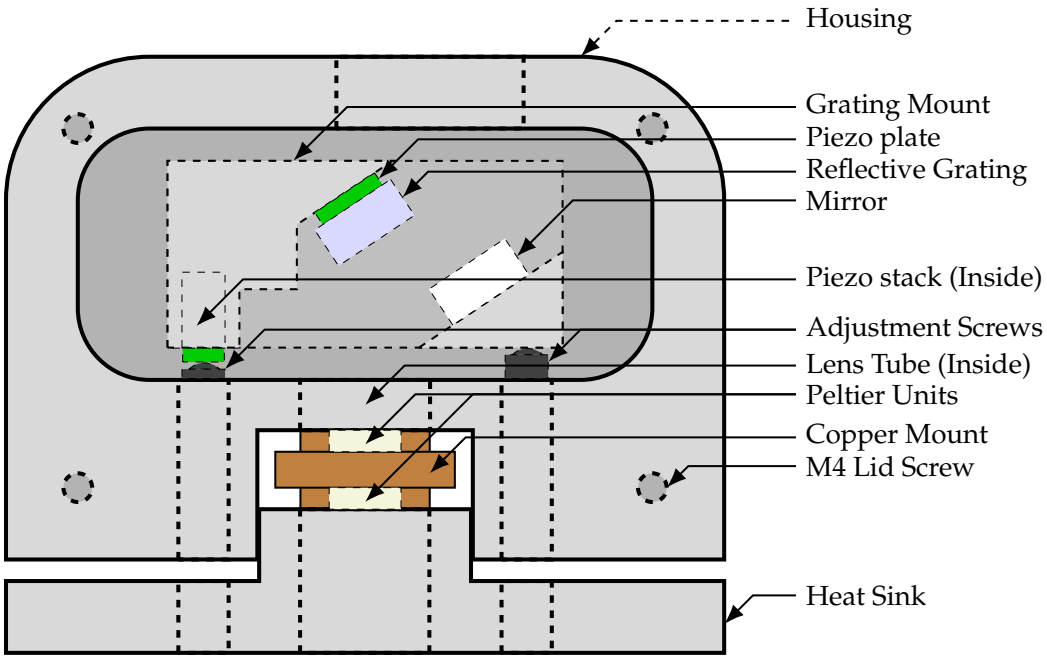

FIGURE 4.1: Diagrammatic representation of the ECDL that was constructed for our experiment.

The grating mount was designed by the author, while the housing and other components were designed by a previous student, Shaun Burd. An isometric view of the mount is shown in Fig. 4.2. The mount is held in the housing by springs. The springs are placed in to the middle hole on the far right, and in the bottom hole that's second to the left in Fig. 4.2. Screws are inserted perpendicular to these holes in order to secure the springs. An epoxy is used to mount the mirror, piezoelectric plate, and grating to the mount as shown in Fig. 4.1. The piezo stack is secured in the hole pictured on the left most side of the mount.

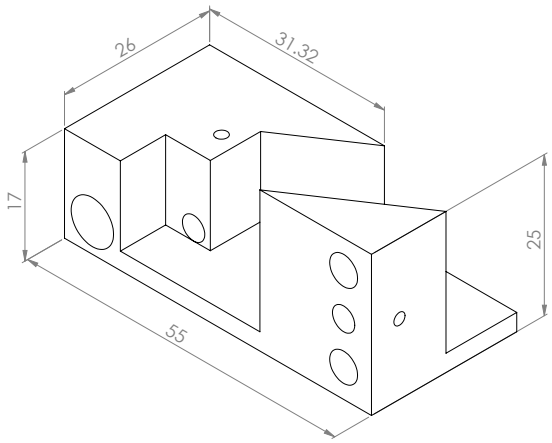

FIGURE 4.2: Isometric view of the grating mount. The units are in millimetres. Circles represent holes drilled in to the mount (see Appendix A for a technical drawing).

We wanted a wavelength close to 464.3 nm in order to perform E2 transitions in potassium (see Fig. 5.1). We chose a grating with 2400 lines/mm, leading to $d = 416.6$ nm, thus allowing us to construct a mount that must have an angle of incidence $\theta = 33.83°$ from (4.1). Gratings with smaller lines/mm would have lead to a smaller angle θ, which would have made the design for the mount difficult given the space constraints of the housing.

A summary of the parts used in the ECDL are given in Table 4.1. The parts listed correspond to those in Fig. 4.1. The current to the laser diode is delivered via a electrostatically protected Thorlabs SR9HF-DB9 cable, connected between the current controller and the four pins at the back of the laser diode. Electrostatic protection must be used when handling these laser diodes, as they can be permanently damaged or destroyed at even the slightest discharge.

4.2.1 Principles for designing future ECDLs

Through the experience gained through the construction of this ECDL, and some of the failed attempts along the way, we learnt a number of principles that can be applied to future ECDL designs. These are:

1. **Not all laser diodes are created equal.** Always check to ensure that the pin configuration of your laser diode (Thorlabs lists these as alphabetical codes,

Part	Manufacturer	ID
Reflective Grating	Thorlabs	GH13-24V
Mirror	Thorlabs	BBSQ05-E02
Piezo stack	Thorlabs	AE0505D08F
Piezo plate	Noliac	NAC2015
Lens Tube	Thorlabs	LT230P-B
Collimation Lens	Thorlabs	A230-A
Laser Diode	Nichia	NDBA116T
Current Controller	Thorlabs	LDC220C
Temp PID Controller	TE Tech	TC-36-25 RS232

TABLE 4.1: Summary of the parts used in our ECDL. Spec sheets are available at the corresponding manufacturer's website.

see Fig. 4.3) match with the available configurations that your current controller has. We were previously using a Thorlabs IP-250-BV current controller board for various laser diodes, but found that this was incompatible with the NDBA116T diode we had ordered for the new application. We had to order a LDC220C current controller that is compatible with a wide range of diode pin configurations given the correct connecting cable.

2. **The laser diode must be single mode.** We had previously ordered a Thorlabs L462P1400MM, a multimode laser, believing that in an ECDL configuration it would only lase at the seeded wavelength. This turned out to be false, and a new single mode diode had to be ordered.

3. **The collimation lens is more critical than it may seem.** We wanted to use the NDBA116T diode, which can only lase in continuous wave mode in an ECDL configuration. When adjusting the collimation lens of this diode at a low current (as to produce a small amount of non-lasing light, needed when performing collimation) we noted that a coloured spot would be focused in the far field. The colour would range from red through to deep blue, depending on the distance of the lens to the diode. It was found that the diode could only lase when the blue dot was visible in the far-field. We believe that this is due to the lens collimating different wavelengths of colour depending on the distance to the light source.

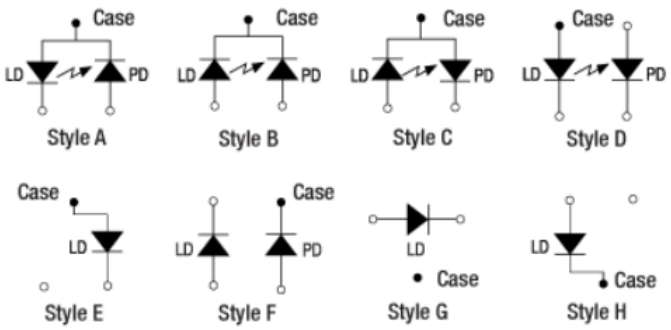

FIGURE 4.3: Thorlabs pin classification system. LD = laser diode, PD = photodiode.

4.3 Performance

4.3.1 Effect of diode current on ECDL metrics

Several performance metrics were taken of our ECDL. We first monitored the output power of the laser diode as we adjusted the current, which is represented in Fig. 4.4. We needed to establish a current limit in order to prevent the laser diode from outputting higher than 30 mW, as our diode's lifetime is shortened when we exceed this power limit. From our measurements we set the current limit at 190 mA, as any current above this point lead to an output power that exceeded 30 mW. The temperature of our laser diode for all recorded measurements was $25°C$.

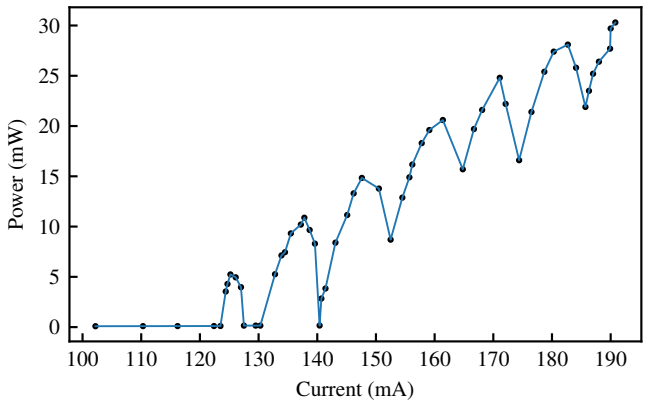

FIGURE 4.4: Graph of the output power of our ECDL as a function of the diode current. Data points are represented as black dots, and a blue solid curve has been plotted over this for visibility. The errors in our measurement were smaller than 0.1 mW and are too small to be represented here.

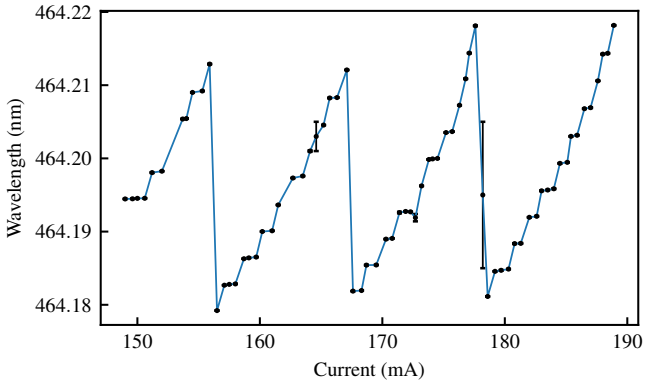

FIGURE 4.5: Graph of the output wavelength of our ECDL as a function of the diode current. The measured points are represented as black dots, with errors represented by vertical lines.

We can also see from Fig. 4.4 that the relationship between the current and power is quite complicated. There's an interplay between the current and the mode that is

promoted by the ECDL configuration. We see that the power oscillates as the current is adjusted, leading to the conclusion that certain current regimes are selecting for particular modes [62]. This isn't much of an issue for our applications, but is important to keep in mind when one adjusts the current.

The current can also control the wavelength of the ECDL output. This is shown in Fig 4.5, and agrees with our previous statement that the current is selecting for particular modes. We also see mode hops in this figure, where small adjustments to the current can lead to large changes in the output wavelength. This should also be kept in mind when scanning, as we would need to set our current such that the wavelength is stable, and not at the edge of a large mode hop.

4.3.2 Fabry-Perot spectrum

One way of measuring the output spectrum of a light source is with a fabry-perot (FP) interferometer. This consists of two mirrors facing one another, placed a distance l apart. Light entering the device will only constructively interfere with itself if it's wavelength is an integer multiple of l, that is $\lambda = nl$. To receive the spectrum of incoming light, one simply scans the distance l while monitoring the transmitted intensity with a photodiode.

The output of our fabry-perot, a Thorlabs SA200-3B, when illuminated with light from our ECDL is shown in Fig. 4.6. The sharp peaks represent the spectrum of our output, and they are seperated by the free spectral range of the fabry-perot, being 1.5 GHz. The time axis is arbitary, and depends on the scan rate of the device. The FP output, usually in volts produced from the internal photodiode, has been scaled to lie between 0 and 1.

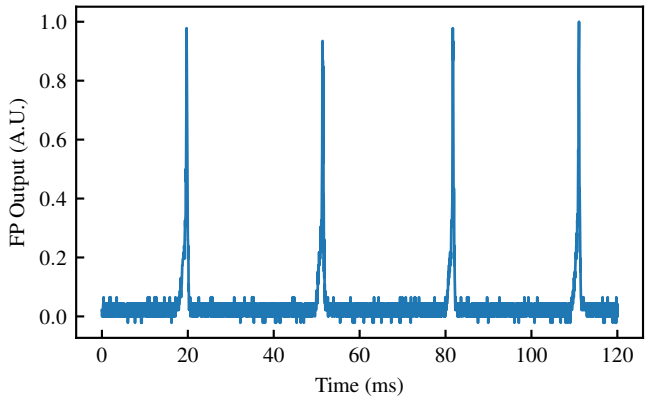

FIGURE 4.6: Fabry-Perot spectrum of our ECDL. Multiple peaks indicate that the entire free spectral range of 1.5 GHz of the fabry-perot have been scanned. The FP output is scaled to lie between 0 and 1, and represented by arbitrary units (A.U.). The time scale is arbitrary and dependent on the scan rate that was chosen with our equipment.

Since we know the free spectral range of the device, we can map the arbitrary time scale of our fabry-perot to a frequency scale. We can use this to measure the linewidth

(in MHz) of our laser, given by the FWHM of our output spectrum. We plot a single peak of our fabry-perot in Fig. 4.7 against the calculated frequency scale. A lorentzian was fit to the peak, showing excellent agreement with the profile of the measured spectrum. The FWHM was measured to be $\Gamma = 19.416(1)$ MHz at an output wavelength of 464.306 nm.

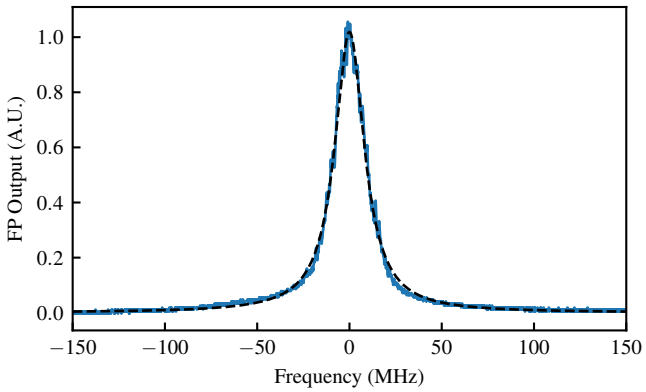

FIGURE 4.7: Plot of a single fabry-perot peak, retrieved from an oscilloscope where 4 averages were taken. A lorentzian fit to this peak is shown in dashed black. The frequency axis is calculated by mapping the free spectral range of 1.5 GHz to the average time between peaks in Fig. 4.6, and has been shifted such that the central peak is at 0 MHz.

The single peak in Fig. 4.7 indicates that the ECDL is operating in what is known as a single mode operation. That is, the output frequency of our laser is largely represent by one single frequency. A multi-modal laser will have multiple peaks at different frequencies. An example of a multimodal spectrum is represented in Fig. 4.8. Such an output spectrum is undesirable when performing spectroscopy, as scanning over a spectroscopic line would occur multiple times in one scan, leading to a confusing output spectrum.

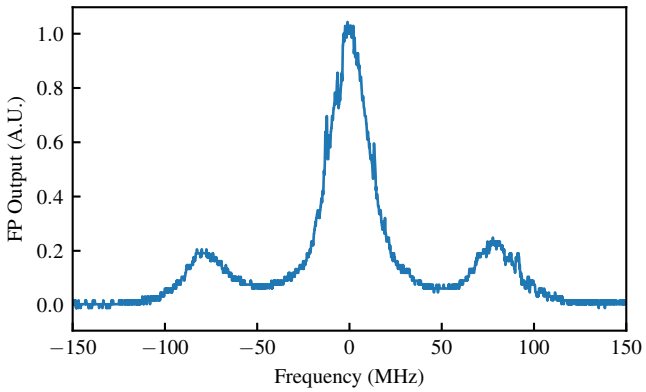

FIGURE 4.8: Example spectrum of a multi-modal ECDL output. This spectrum indicates that multiple frequencies are being produced by the ECDL.

4.3.3 Free running stability over time

We monitored the output wavelength and intensity of our laser as time passed, shown in Fig. 4.9. The wavelength meter can only measure single mode light and produces erratic measurements when multimodal light is measured. We can see from Fig. 4.9 that the laser remains in a single mode operation for approximately 25 minutes before entering multimodal operation. A magnified plot of this single mode region is shown in Fig. 4.10. We can see that in this regime, the wavelength does not change by more than 6×10^{-4} nm (or 850 MHz in frequency).

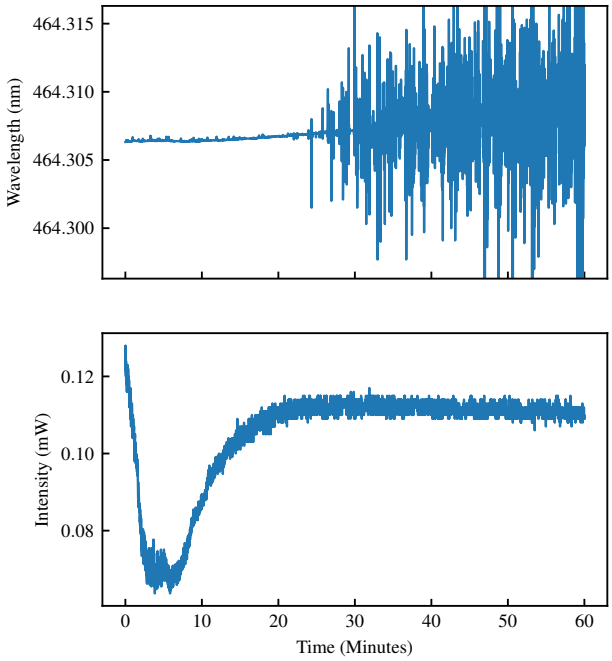

FIGURE 4.9: Plots of the wavelength and power of our ECDL over time. Erratic wavelength measurements correspond to the laser operating in a multimodal configuration.

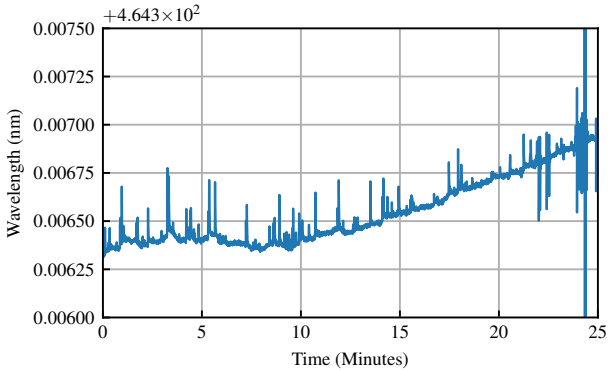

FIGURE 4.10: Plots of the measured wavelength over time, showing only the single mode regime of our measurements.

This stability quite impressive, as no frequency locking is implemented. With frequency locks, ECDL's can typically remain at the same wavelength for several days [60]. We could lock our laser to some frequency if desired, but we intend to use our ECDL for scanning and producing a spectrum, as opposed to locking to a single frequency.

4.3.4 Scanning capability

We monitored the output frequency of our laser light as we adjusted the voltage applied to the piezo plate behind the reflective grating (see Fig. 4.1). The results of this procedure are shown in Fig. 4.11, along with a linear curve that is fit to our data, and the fit produced a gradient of $m = 0.233442(14)$ GHz/V. We can see from Fig. 4.11 that we scanned over roughly 4.5 GHz with ease, and that no mode hop was observed during this period. This turned out to be sufficient for all of our experimental needs, and so the piezo stack (see Fig. 4.1) was not used.

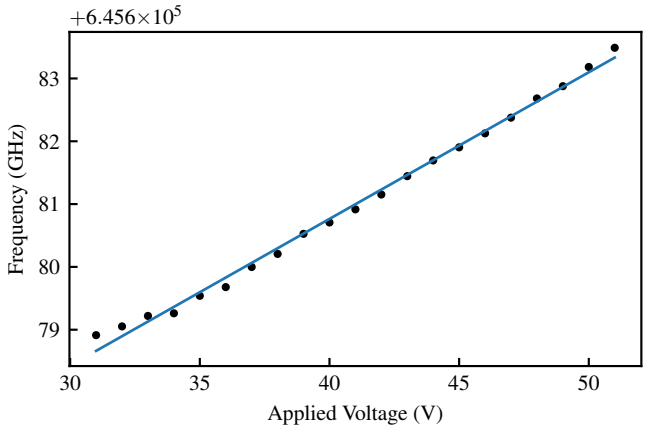

FIGURE 4.11: Output frequency as a function of the voltage applied to the piezo plate placed behind the reflective grating in our ECDL. Measured results are shown as black dots, while the solid curve is a linear fit to this data. The curve was found to have a gradient of $m = 0.233442(14)$ GHz/V.

5 Fluorescence Experiment

5.1 Potassium reference data

From our previous sections, particularly Section 3.2.1, we noted that we wished to use an alkali atom that had a P state between an S and a D state. We chose potassium, as the wavelength required to perform an E2 with this atom allowed us to buy a cheap laser diode for use in our ECDL. In this section, we collect from various sources and report on the physical properties of potassium, such as stability, isotope abundance, energy levels, etc.

Potassium exists in two stable isotopes, ^{39}K and ^{41}K, as well as a meta-stable isotope ^{40}K. The isotope, mass, natural abundance, lifetime, and nuclear spin are summarised in Table 5.1. Our gas sample, a Thorlabs GC25075-K Potassium Reference Cell, possesses all three isotopes in their natural abundance. We'll ignore the ^{40}K and ^{41}K isotopes in our analysis, as they constitute less than 7% of the sample.

Isotope	Mass (u)	Abundance (%)	τ	I
^{39}K	38.96370668(20)	93.2581(44)	stable	3/2
^{40}K	39.96399848(21)	0.0117(1)	1.26×10^9 y	4
^{41}K	40.96182576(21)	6.7302(44)	stable	3/2

TABLE 5.1: Isotopes of potassium. Includes the isotope, mass [63], natural abundance [64], radioactive lifetime [64], and nuclear spin I [64] properties of the isotope. The number of protons in all isotopes is $Z = 19$ for potassium.

One of the challenges with attempting to perform E2 transitions was the very small scattering cross-section presented by the fast moving atoms. To overcome this, we heat the gas cell in order to increase the number of atoms that can interact with our laser beam. Fig. 5.2 represents the vapor pressure curve for potassium, and can be found from [63] as

$$\begin{aligned} \text{(solid)} \qquad & \log p = 7.9667 - \frac{4646}{T} \qquad && 298\ \text{K} < T < T_m, \\ \text{(liquid)} \qquad & \log p = 7.4077 - \frac{4453}{T} \qquad && T_m < T < 600\ \text{K}, \end{aligned} \tag{5.1}$$

where p is the vapour pressure and $T_m = 63.65°C = 336.8$ K is the melting point of potassium. Note that the above equation gives the pressure in mbar units.

An energy diagram of the fine and hyperfine structure of potassium is given in Fig. 5.1, where the wavelength λ and linear frequency ν are retrieved from [64] and are measured in a vacuum, while the Γ values are taken from [65] and [66]. We can

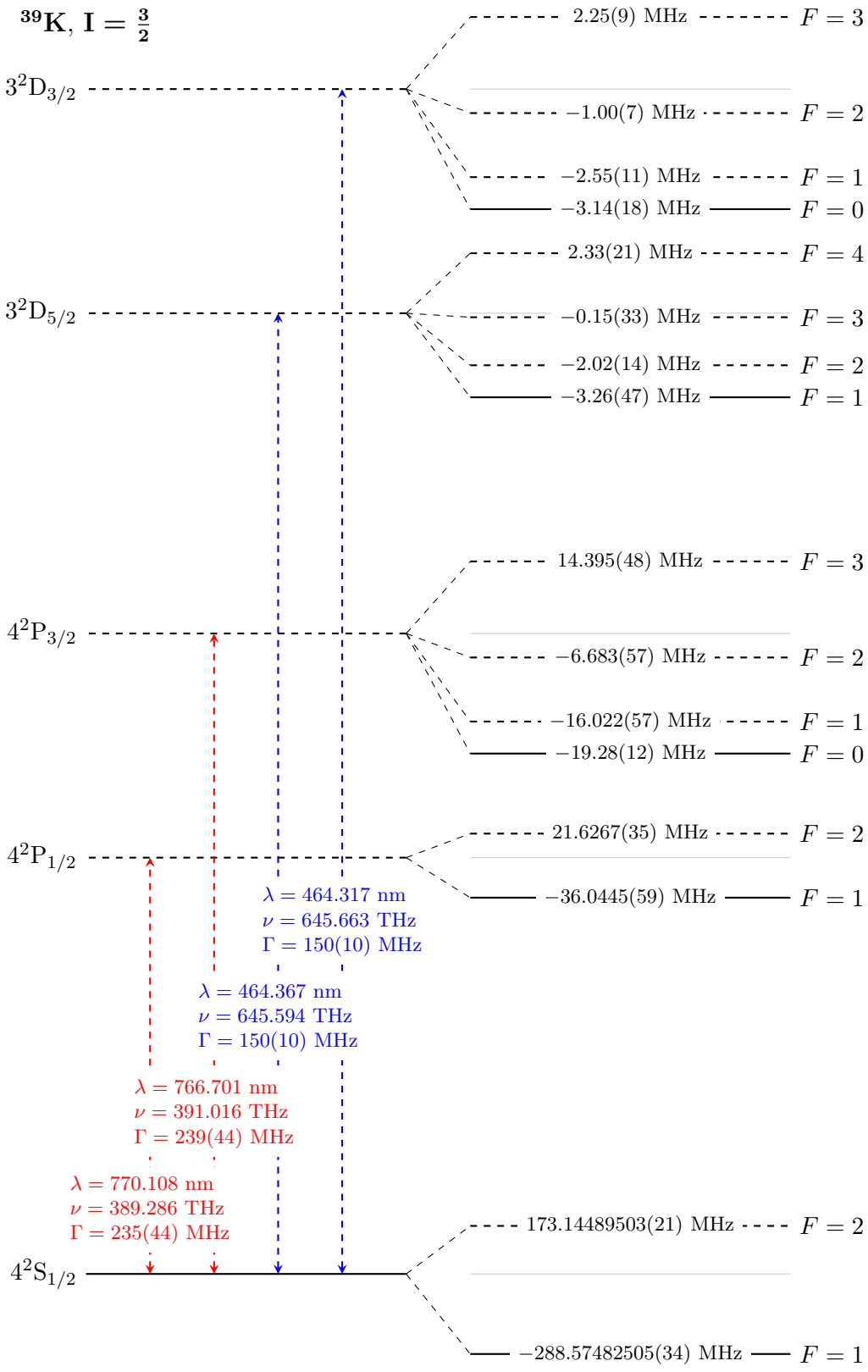

FIGURE 5.1: Energy level diagram of the ^{39}K potassium isotope. E1 (dipole) transitions and E2 (quadrupole) transitions are highlighted in red and blue, respectively. The hyperfine energy splitting is embedded within each hyperfine level in units of MHz.

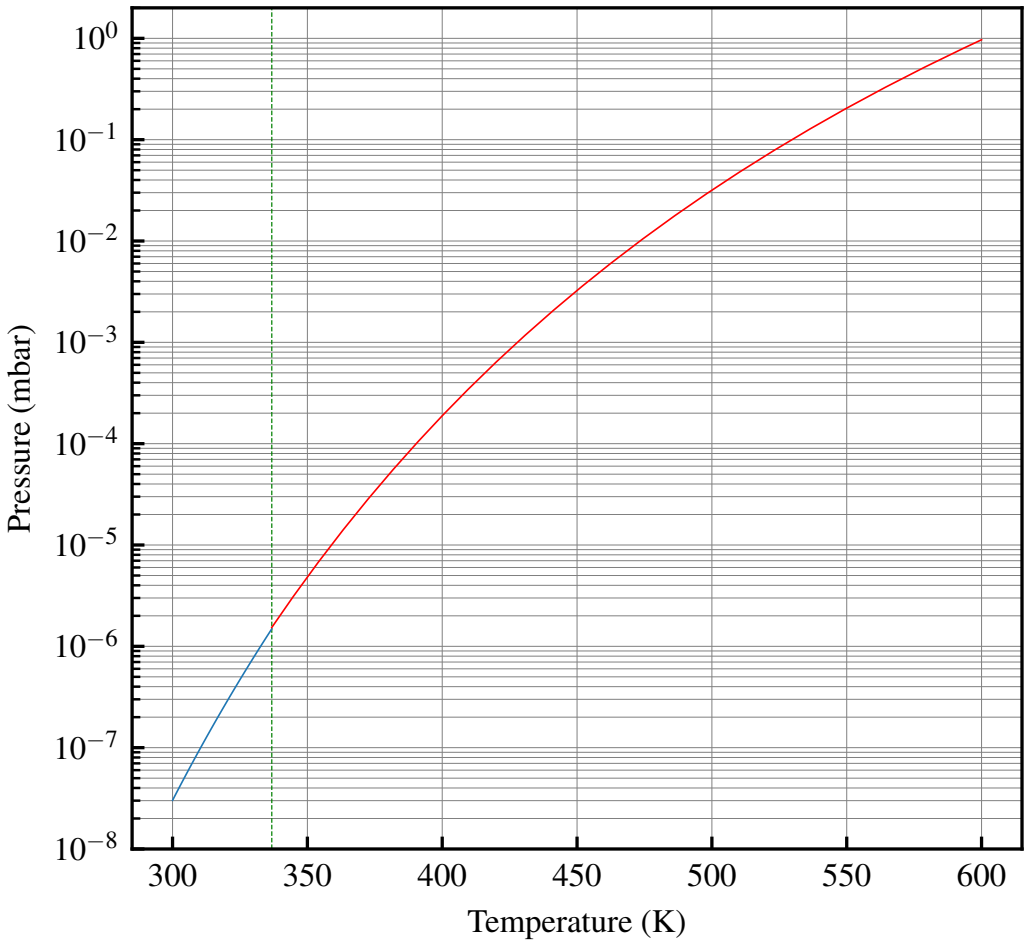

FIGURE 5.2: Vapor pressure curve of potassium. The blue curve is in the solid regime, while red is in the liquid regime.

see that in order to perform quadrupole transitions that we would need a laser capable of outputting ~ 464.3 nm, and from our considerations of saturation intensity in Section 3.2.4, would need to have an output power on the order of 1-100 mW. The Nichia NDBA116T was chosen as our laser diode, as it is a high-quality single mode laser capable of outputting a maximum of 30 mW of power. Note that the value for Γ in the quadrupole transitions is equivalent to $\Gamma_d = \Gamma_{dp} + \Gamma_{ds} \approx \Gamma_{dp}$ from Section 3.2.2. No explicit values for Γ_{dp} or Γ_{ds} could be found.

To calculate the hyperfine energy splitting seen in Fig. 5.1 we make use of the hyperfine splitting equation derived in [3], given by

$$\Delta E_{hfs} = \frac{1}{2} A_{hfs} K + B_{hfs} \frac{\frac{3}{2}K(K+1) - 2I(I+1)J(J+1)}{4I(2I-1)J(2J-1)}, \tag{5.2}$$

where $K = F(F+1) - J(J+1) - I(I+1)$. The constants A_{hfs} is the hyperfine A constant, and B_{hfs} is the hyperfine B constant, and are found through experiment. The meaning of F, J and I was discussed in Section 2.2. Note that this equation is only valid when $J \neq 1/2$. When $J = 1/2$, only the first term in ΔE_{hfs} is valid, i.e.

$\Delta E_{hfs} = A_{hks}K/2$ when $J = 1/2$. Values for the hyperfine A and B constants are summarized in Table 5.2 for each fine structure level. Note that the B constant in the $3^2D_{5/2}$ state remains unknown, where only an upper limit of 0.3 MHz can be found. The hyperfine states shown in Fig. 5.1 for the $3^2D_{5/2}$ level are calculated from the A hyperfine constant while setting the B constant to 0 ± 0.3 MHz.

Level	A_{hfs} (MHz)	B_{hfs} (MHz)
$4^2S_{1/2}$	230.85986004(28) [67]	0
$4^2P_{1/2}$	28.8356(47) [67–70]	0
$4^2P_{3/2}$	6.083(20) [67, 69, 70]	2.828(73) [67, 70]
$4^2D_{3/2}$	0.96(4) [71]	0.37(8) [71]
$4^2D_{5/2}$	0.62(4) [71]	< 0.3 [71]

TABLE 5.2: Hyperfine constants of the ^{39}K potassium isotope. The constants are given in units of linear frequency. The references are where the constants were received, where multiple reference implies that an average has been taken.

5.2 Experimental Setup

We wish to detect the presence of quadrupole excitations within a potassium gas cell that is subject to a laser beam with a wavelength of ~ 464 nm. To do this, we'll excite to either the $3^2D_{3/2}$ or the $3^2D_{5/2}$ quadrupole lines of potassium, and then detect the fluorescence due to the cascading decay path between the D $\rightarrow$ P followed by the P $\rightarrow$ S levels.

A depiction of our experimental setup is shown in Fig. 5.3. The home made 464nm ECDL from Chapter 4 was used here to excite quadrupole transitions in our potassium reference cell (a Thorlabs GC25075-K). A Thorlabs IO-3D-405-PBS optical isolator was placed directly in front of the ECDL to prevent back-reflection.

Our potassium cell was heated in order to overcome some of the difficulties of making a quadrupole transition in a gas. Initially, an oven was built in order to heat the cell, but this caused the windows of the cell to be coated in potassium, thus blocking the beam. A specially designed cell heater was then constructed from a combination of lens tubes and heating wire. The heating wire was wrapped around the lens tubes such that only the ends of the potassium cell were heated – cleaning the windows while also providing heat. The potassium cell was then placed inside of the lens tubes, which was done in order to isolate the cell from direct contact with the heating wire, which may have caused damage or shattering to the cell.

This heater was not particularly efficient, as the wires managed to reach $88\ ^\circ C$ when 260 V was applied, but the cell itself only reached $46^\circ C = 319.15$K at the centre of the cell, as measured by a thermocouple placed directly on the potassium cell. This inefficiency may be due to the fact that the cell was not in direct contact with the cell, but instead with a set of lens tubes. A lot of heat may have also been lost as the heating wire caused the mounting apparatus to become quite hot as well. The heating could be improved through the use of a Thorlabs GCH25-75 specially

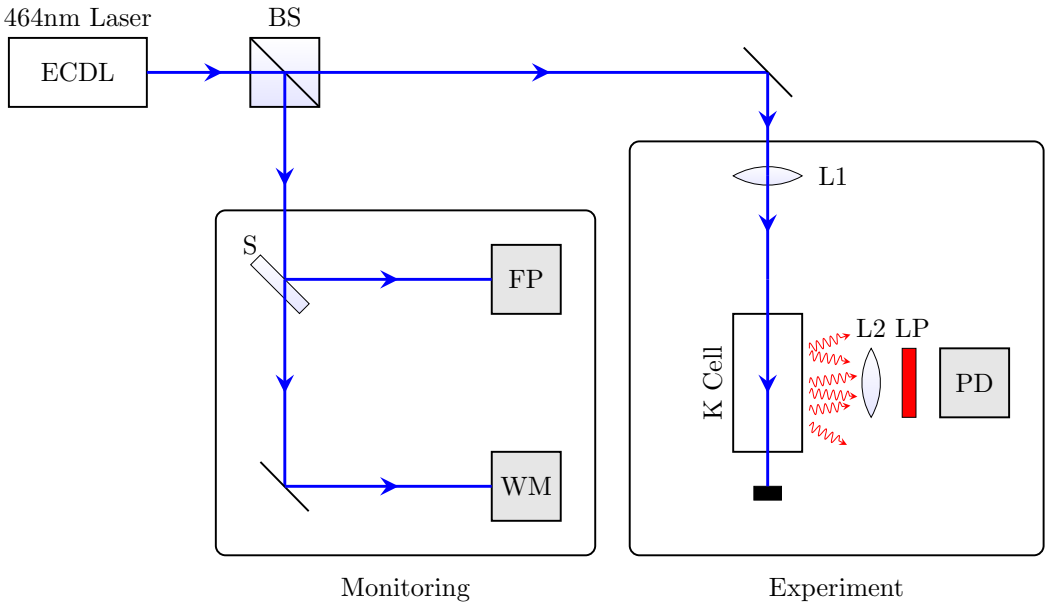

FIGURE 5.3: Experimental setup used to measure the P $\rightarrow$ S dipole fluorescence in a potassium gas cell. BS = beam splitter; S = sampler; L1 = 500 mm lens; L2 = 50 mm lens; LP = long pass filter; FP = fabry-perot; WM = wavelength meter; PD = photodetector.

designed cell heater (not purchased due to budget constraints), or by modifying our design in such a way as to minimise our drawbacks.

Fluorescence between the D and P state has a wavelength around 1177 nm, while that between the P and S state is around 770 nm. We chose the Thorlabs PDF10A photodetector for it's high-sensitivity, and was the same detector used in a similar experiment [72]. It's operating range is 320 - 1100 nm, allowing us to measure the P to S fluorescence but not the D to P fluorescence. The lens L1 forms a focal point somewhere in the cell, while the L2 lens forms an image of this focal point on the detector. A long pass filter was placed in front of the detector in order to remove the possibility of detecting any scattering from the 464 nm laser. The entire fluorescence experiment was also covered to prevent any background light from being detected.

To perform our experiment, the laser was tuned to a central wavelength of either 464.317 nm or 464.367 nm, depending on the transition we wished to make. The laser was then scanned using custom Labview code and a Synertronic Sveta-Piezo 100V, connected to the piezo plate behind the reflective grating wihin the ECDL (see Fig. 4.1). We scanned this diode with a peak-to-peak amplitude of 24 V, corresponding to a 5.6 GHz scan from Fig. 4.11. The fabry-perot was used to ensure the laser remained in single mode operation during scanning. The results of this procedure are reported in the section below.

5.3 Results and Analysis

The results of our experiment are shown in Fig. 5.5 and Fig. 5.6 and were retrieved from a digital oscilloscope where 32 averages were taken. Fig. 5.5 represents the $4^2S_{1/2}$ to $3^2D_{3/2}$ transition, while Fig. 5.6 represents the $4^2S_{1/2}$ to $3^2D_{5/2}$ transition. The fluorescence measurement in our figures has been scaled in such a way as to be comparable to one another. The maximum measured fluorescence power was $25.6 \pm 10\%$ fW, and all the measured fluorescence values have been reported as fractions of this value.

To model our transitions, we first note that the absolute frequency shifts of the hyperfine levels in the D states are less than 5 Mhz (see Fig. 5.1). Since our laser linewidth is around 20 Mhz (see Fig. 4.7), we deem the hyperfine states in the D levels to be unresolvable in our experiment. We then note that the frequency difference between the ground state's hyperfine levels is around 461.7197 MHz, and since our scan range covers 4.5 Ghz, we will observe both the $F = 1 \to F'$ and the $F = 2 \to F'$ transitions in our spectrum. We can also use the Boltzmann probability distribution $P(\nu_i) = \exp(h\nu_i/k_BT)/\sum_j \exp(h\nu_j/k_BT)$ to show that the population distribution between the two hyperfine ground states are equal up to four significant digits, and given by $P(\nu_{F=1}) = P(\nu_{F=2}) = 0.5$.

Now, consider a transition between two hyperfine states $|F'\, M'_F\rangle$ and $|F\, M_F\rangle$, where the transition is driven by a field described by the spherical tensor $T^{(2)}_q$. The Wigner-Eckart theorem tells us that the transition strength between these two levels is given by

$$\begin{aligned}\left|\langle F'\, M'_F|T^{(2)}_q|F\, M_F\rangle\right|^2 =& \left|\langle F'||\mathbf{T}^{(2)}||F\rangle\right|^2 \left|\langle F'\, M'_F|F\, M_F; 2\, q\rangle\right|^2 \\ =& (2F+1)(2J'+1)\left|\langle J'||\mathbf{T}^{(2)}||J\rangle\right|^2 \\ & \times \left|\langle F'\, M'_F|F\, M_F; 2\, q\rangle\right|^2 \begin{Bmatrix} J' & J & 2 \\ F & F' & I \end{Bmatrix}^2, \end{aligned} \tag{5.3}$$

where I used the recoupling relation in (3.15) for hyperfine states to ensure that I don't couple between states that violate the quadrupole hyperfine selection rules in Table 3.4. Since we have not applied a magnetic field, we have to sum over the M'_F and M_F states, and since we cannot resolve the D hyperfine levels, we must also sum over the F' states. This results in a quantity independent of q, but dependant on F and J'. In the case of $J' = 3/2$ this results in

$$\frac{1}{\left|\langle 3/2||\mathbf{T}^{(2)}||1/2\rangle\right|^2} \sum_{F',M'_F,M_F} \left|\langle F'\, M'_F|T^{(2)}_q|F\, M_F\rangle\right|^2 = \begin{cases} \frac{9}{25} & \text{if } F = 1, \\ \frac{31}{25} & \text{if } F = 2, \end{cases} \tag{5.4}$$

and in the case of $J' = 5/2$ this results in

$$\frac{1}{\left|\langle 5/2||\mathbf{T}^{(2)}||1/2\rangle\right|^2} \sum_{F',M'_F,M_F} \left|\langle F'\, M'_F|T^{(2)}_q|F\, M_F\rangle\right|^2 = \begin{cases} \frac{31}{25} & \text{if } F = 1, \\ \frac{9}{25} & \text{if } F = 2. \end{cases} \tag{5.5}$$

Using this information, we chose to model our transition spectrum as the sum of two gaussian peaks (as the spectrum is doppler broadened) that are offset by either $\nu_1 = -288.575$ MHz or $\nu_2 = 173.145$ MHz from a universal ν_0 parameter, corresponding to transitions from the ground $F = 1$ or $F = 2$ state, respectively. The relative amplitudes between the two gaussians are given by either (5.4) or (5.5) depending on which transition is made. We also require that the standard deviation σ is the same for both gaussian peaks, as both transitions should have the same doppler broadening. Using a least squares method, we fit this model to our data. The results are shown in Fig. 5.7 and Fig. 5.8, showing an excellent agreement with the data.

5.4 Discussion

Through the use of a custom built ECDL and the selection of potassium as our medium in order to overcome linewidth problems, we've demonstrated excitation of a quadrupole transition. This experiment serves as an important stepping stone in achieving quadrupole coupling in a gas. Though this experiment seems simple to perform on paper, it should be noted that a great deal of challenge was experienced due to this being a quadrupole transition. There is a reason that these transitions are called 'forbidden' – they're always much weaker than dipole transitions, they typically have exceptionally long decay times, and are very difficult to observe.

We could only find one paper that performed an experiment similar to ours that employed a potassium vapour cell [65]. This paper explored the lifetime of the $3^2\mathrm{D}_j$ states ($j = 1/2,\ 3/2$), and does not report on the fluorescence spectrum received. Instead, the paper makes use of a pulsed dye laser that operates at ~ 445 nm. Our experiment differs by making use of a continuous wave ECDL that performs a 5.6 GHz scan over the $4^2\mathrm{S}_{1/2} \rightarrow 3^2\mathrm{D}_j$ levels, where our aim was to monitor the fluorescence spectrum due to the $4^2\mathrm{P}_{j'} \rightarrow 4^2\mathrm{S}_{1/2}$ decay during the scan.

Other experiments similar in nature to ours have been performed on other atoms. One paper we found, which helped inspire this experiment, not only retrieved the fluorescence spectrum of a P to S transition in a caesium vapour cell, but also performed a unique form doppler free spectroscopy that used two different wavelengths of light in order to resolve the hyperfine transitions of caesium [72]. Their experiment used two ECDL's, where one was locked to the P to S transition (~ 852 nm) of caesium, while the other scanned the S to D quadrupole line (~ 685 nm). The population dynamics of the atom was such that one could detect that a quadrupole transition had occurred by monitoring the output intensity of the locked 852 nm line while scanning the 685 nm laser. More advanced experiments have managed to show evidence of a $5\mathrm{P}_{3/2}$ to $6\mathrm{P}_j$ ($j = 1/2, 3/2$) quadrupole transition in rubidium vapour [73] by monitoring the dipole fluorescence due to the 6P excited state decaying to the 5S ground state. This experiment made use of a doppler free setup with two differing wavelengths of light where one beam would excite to the $5\mathrm{P}_{3/2}$ state, while the counter propagating beam would cause the $5\mathrm{P}_3/2$ to $6\mathrm{P}_j$.

5.4.1 Choice of potassium over other atoms

We initially chose to use potassium over rubidium, both for its level structure as well as consideration of the cost of the diode. A consideration for beam intensity was also made, as quadrupole coupling also depends on the overall beam power. As such, we initially chose the Thorlabs L464P1400MM laser diode for use within our ECDL. This diode could reach a maximum power of over 1 W, and was closer to the desired wavelength than that of the equivalent rubidium laser. However, using the diode proved to be ineffective, as the diode was highly multi-modal, even in the ECDL configuration. We had to abandon this diode, and purchase a much more expensive Nichia NDBA116T laser diode, as this was single mode and could only operate in a continuous wavelength mode in an ECDL configuration. This diminished our expectations of performing this experiment at a low cost.

Another candidate atom for selection was caesium. It bears a similar level structure to that of rubidium and potassium. It's quadrupole line has a wavelength of 685 nm and cheap single mode laser diodes exist at this frequency, such as the Thorlabs HL6750MG. It's also a very well studied atom, as the frequency difference between it's ground level hyperfine states serves as the definition of our unit of time. We still chose potassium over this, as the laser diode we wished to use had a very high power, which we hoped would have allowed us to perform the our quadrupole transitions with similar ease as dipole transitions. However, as we did not end up using this high power diode, caesium would have been a much better choice.

5.4.2 Challenges in spectroscopy of quadrupole transitions

Measuring this fluorescence spectrum turned out to be more difficult than we imagined. Various experiments were performed that had failed up until we managed to get the PDF10A femtowatt detector. Previous experiments made use of a Hamamatsu R446 photomultiplier tube (PMT) connected to a lock-in amp, where signal modulation was performed using a chopper wheel on the incoming light. This failed, as we suspect the PMT we were using produced too much background noise for a detectable fluorescence signal even with the use of a lock-in amp. We should also note that, due to a lack of low-noise circuitry, we did not operate the PMT with any kind of amplification circuit at its output, so this could have been another reason as to why the PMT failed to produce a signal.

Other experiments attempted a Doppler free approach, where we split our beam into three paths through the use of a 10% sampler. A diagram of this experiment can be seen in Fig. 5.4. We attempted this experiment in order to resolve the hyperfine structure in our ground level. For this we used a Newport 2107 FC-M balanced photodetector – a device with two photodiodes whose output is the difference between the two photodiode signals – where one input was our reference beam, while the other was our probe. The result should have produced sharp output peaks when scanning over the hyperfine ground states in our vapour cell, but we had still not managed to receive a signal, even with the use of a lock-in amp. It's possible that, due to the extremely low amount of light that is absorbed in these quadrupole transitions, that our equipment was simply not sensitive enough to detect the presence of our signal.

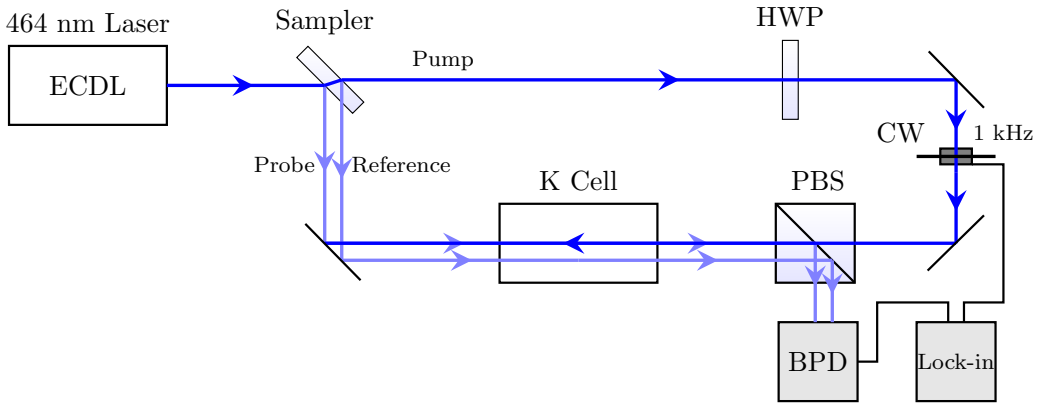

FIGURE 5.4: Initial doppler free experiment that we performed. The beam was split into a probe, pump and reference beam and sent through the vapour cell as per a usual doppler free setup. Signals from the BPD and CW were sent to the lock-in amp from which we attempted to measured our signal. The HWP is adjusted such that the maximal amount of light is transmitted through the PBS. HWP = half-wave plate; CW = 1 kHz chopper wheel; PBS = polarizing beam splitter; BPD = balanced photodiode

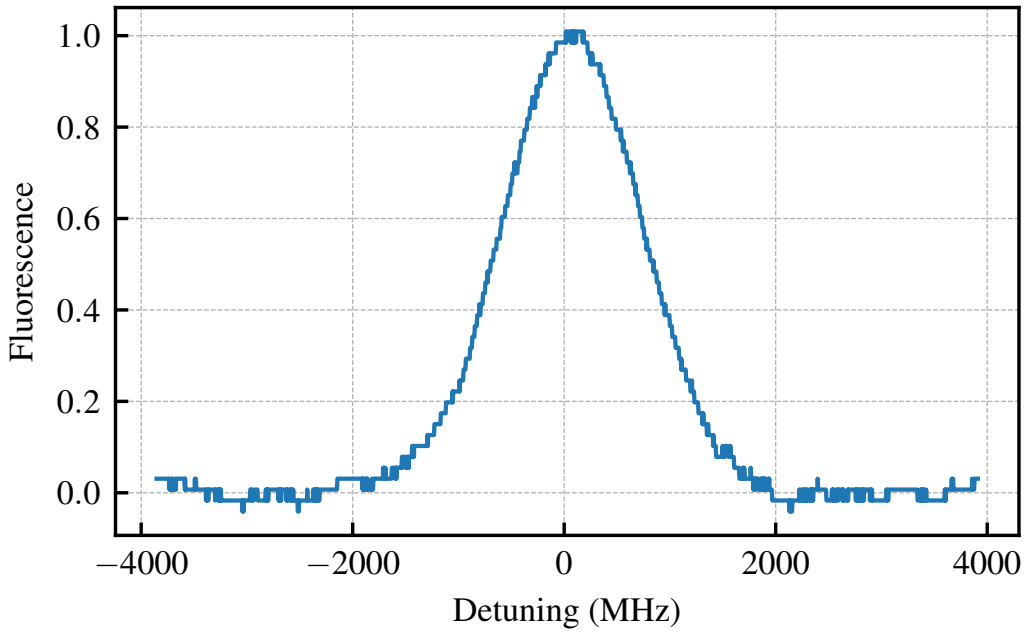

FIGURE 5.5: Measured fluorescence of potassium as observed when the $4^2S_{1/2}$ to $3^2D_{3/2}$ transition is made. The fluorescence is normalized such that 1 represents the maximum measured intensity, which was roughly $25.6 \pm 10\%$ fW.

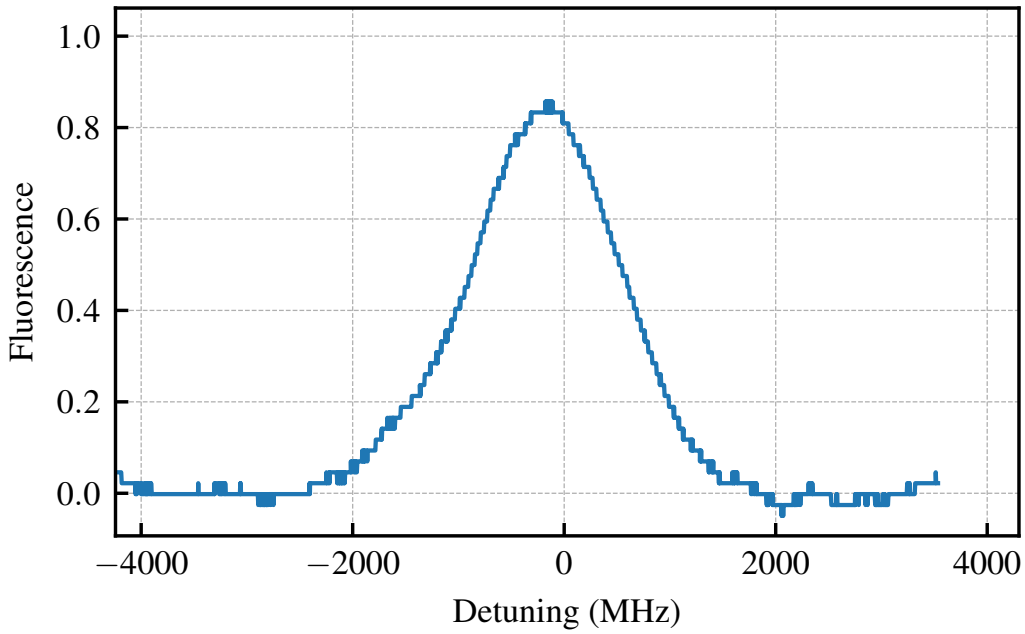

FIGURE 5.6: Measured fluorescence of potassium as observed when the $4^2S_{1/2}$ to $3^2D_{5/2}$ transition is made. The fluorescence is normalized as in Fig. 5.5.

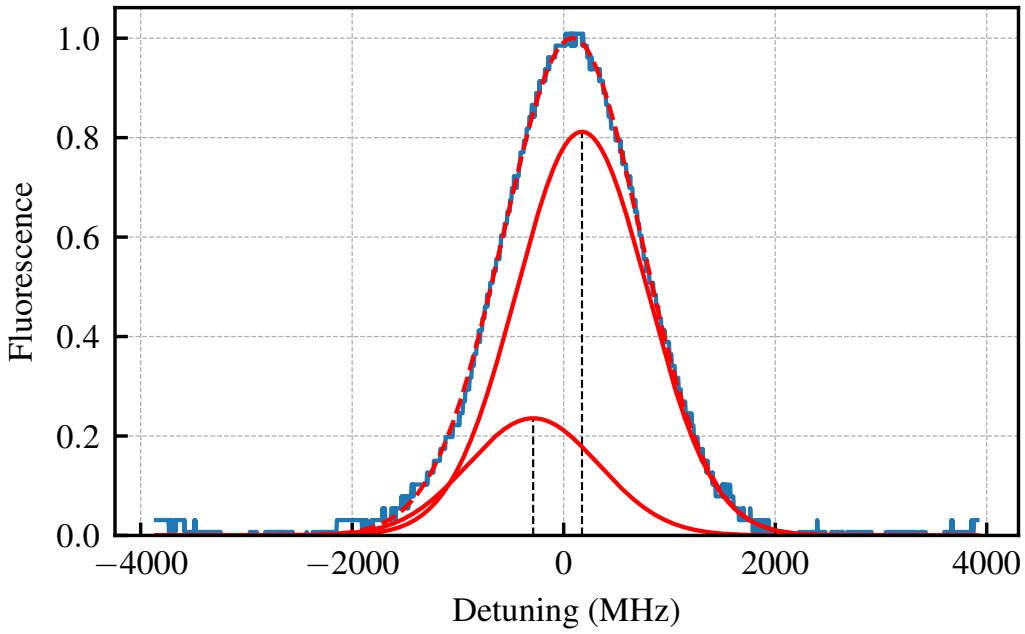

FIGURE 5.7: Result of curve-fitting the sum of two gaussians to the fluorescence data collected from the $4^2S_{1/2}$ to $3^2D_{3/2}$ quadrupole transition. The individual gaussians are shown in solid red, while their sum is shown in dashed red.

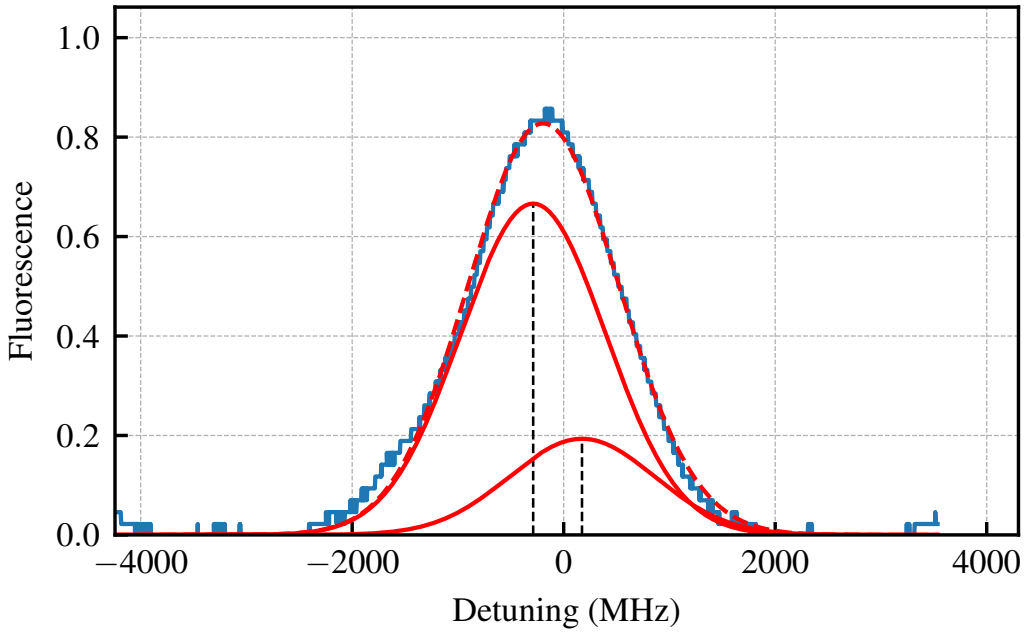

FIGURE 5.8: Result of curve-fitting the sum of two gaussians to the fluorescence data collected from the $4^2S_{1/2}$ to $3^2D_{5/2}$ quadrupole transition. The individual gaussians are shown in solid red, while their sum is shown in dashed red.

6 Conclusion

6.1 Summary

We've expanded upon the already existing spectroscopic theory by including quadrupole transitions. Examining these quadrupole transitions for a generalised magnetic field direction and polarization direction indicated that certain directions of the magnetic field can promote or suppress transitions between differing atomic magnetic sublevels, and was explained through the principle of conservation of angular momentum. This was especially relevant in the case where light had possessed OAM, where we had found similar results to previous theoretical calculations [44], which was later backed up by experimental evidence [48].

We then set up an experiment where we managed to show that we could perform an indirect form of quadrupole spectroscopy on a potassium S to D transition using a custom designed ECDL. The experiment proved difficult to perform as these quadrupole transitions are very weak, but we succeeded by using the fluorescence produced from the decay cascade D to P to S, where we recorded the fluorescence between the P and S states. This was similar in nature to previous experiments where a quadrupole transition was observed through fluorescence caused by a decay between dipole states after a quadrupole excitation had occurred [65, 72, 73], although we had used potassium over caesium [72] or rubidium [73].

6.2 Future Work

Future experiments would need to be able to resolve individual magnetic structure transitions. This is because the predictions made in Chapter 3 showed that quadrupole transitions involving LG-beams of non-zero topological charge $\ell \neq 0$ only really begin to play a role when a magnetic field is introduced and when the transitions between two magnetic states becomes involved.

Apart from the future work surrounding potassium, one could also explore molecules as a potential candidate for observing the OAM in light coupling with molecular transitions. Molecules can possess a rotation about their centre of mass, leading to rotational energy levels in their spectra. Some theoretical work with dipolar molecules (molecules with two atoms) [51, 54] has shown that the OAM of light can couple with these rotational modes, and that this can occur in the dipole approximation if the molecule is inhomogenous (that is, one atom weighs more than the other). To the best of our knowledge, no experiments exploring this coupling in molecules have been performed.

Appendix

A Technical drawings of the ECDL

The following pages give the technical drawings of the ECDL that was used in our experiment. These are meant for reproducibility purposes.

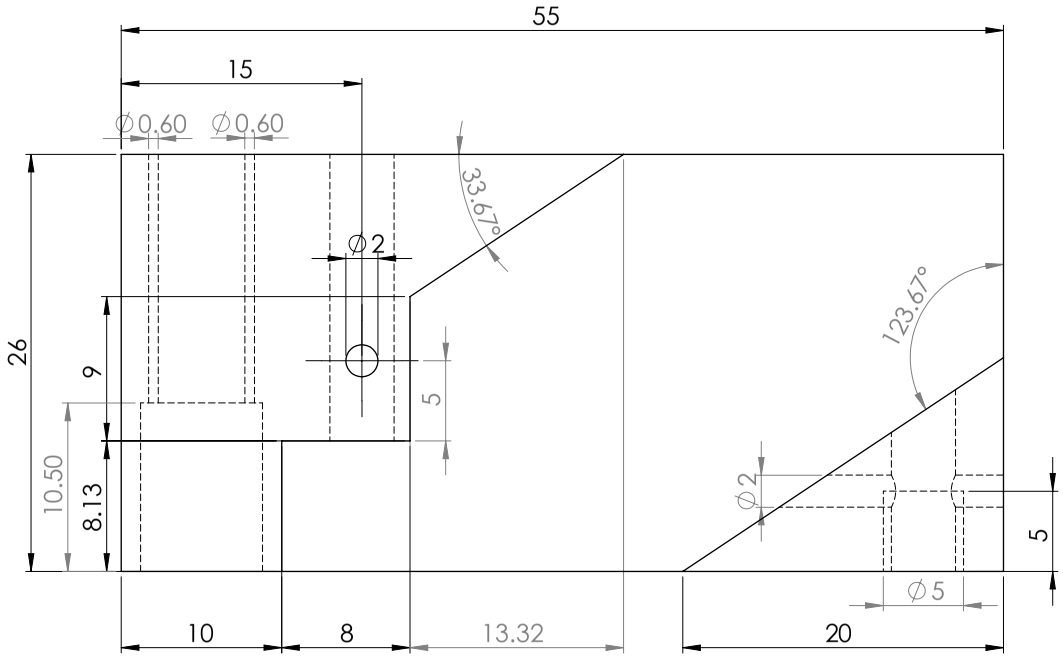

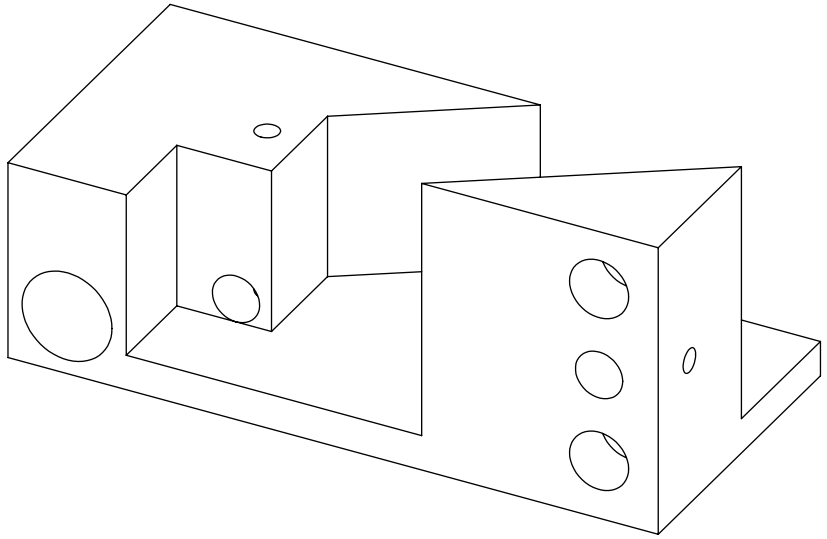

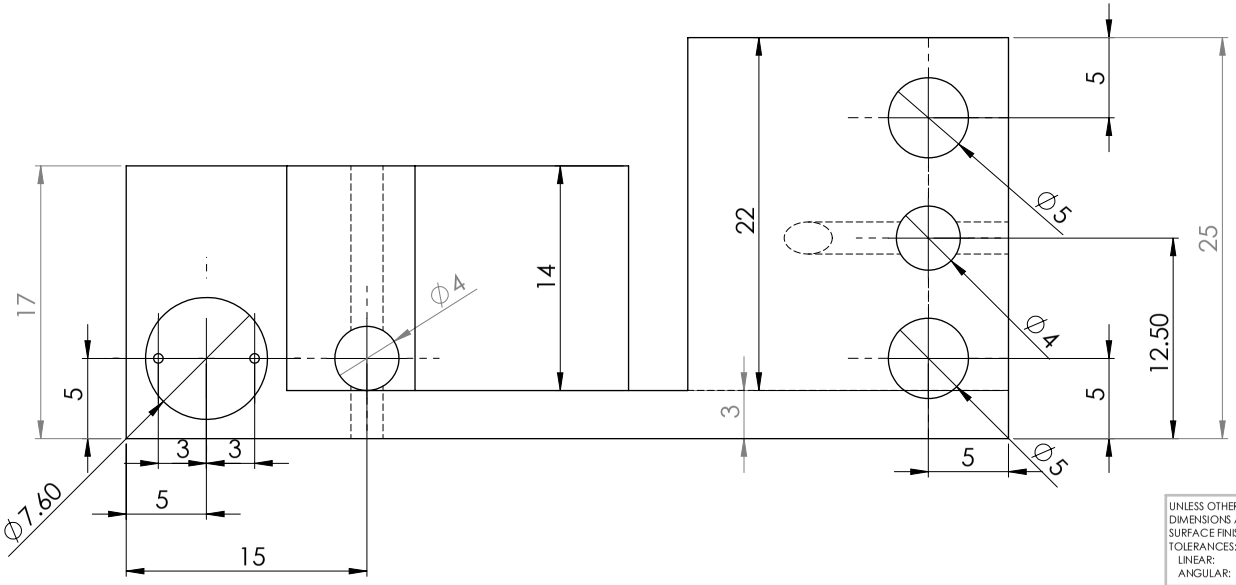

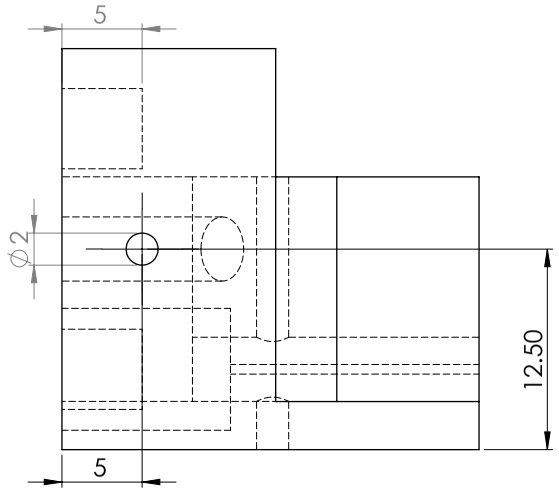

UNLESS OTHERWISE SPECIFIED: DIMENSIONS ARE IN MILLIMETERS SURFACE FINISH: TOLERANCES: LINEAR: ANGULAR:		FINISH:		DEBURR AND BREAK SHARP EDGES		DO NOT SCALE DRAWING	REVISION
	NAME	SIGNATURE	DATE			TITLE: 462nm Mount	
DRAWN	Jason						
CHK'D							
APPV'D							
MFG							
Q.A				MATERIAL:		DWG NO.	A3
				WEIGHT:		SCALE	SHEET 1 OF 1

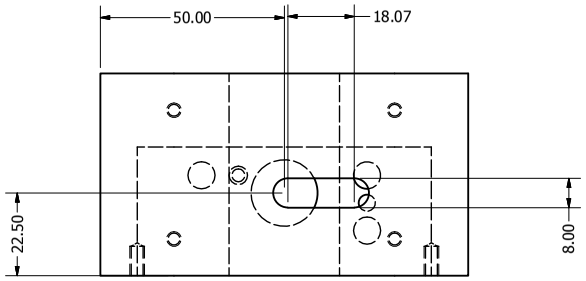

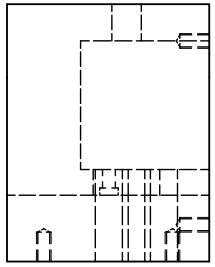

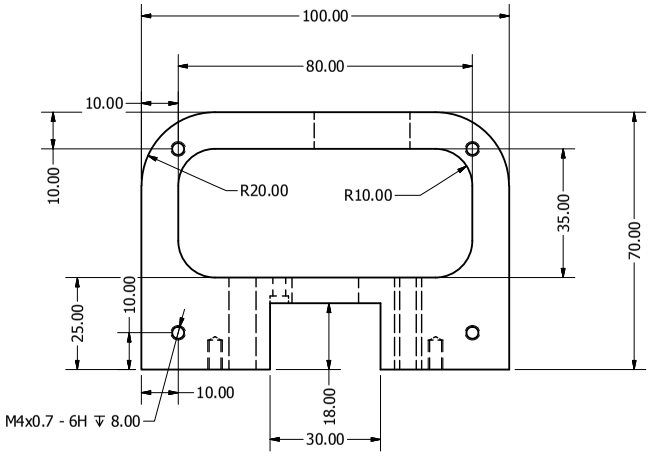

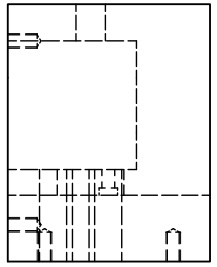

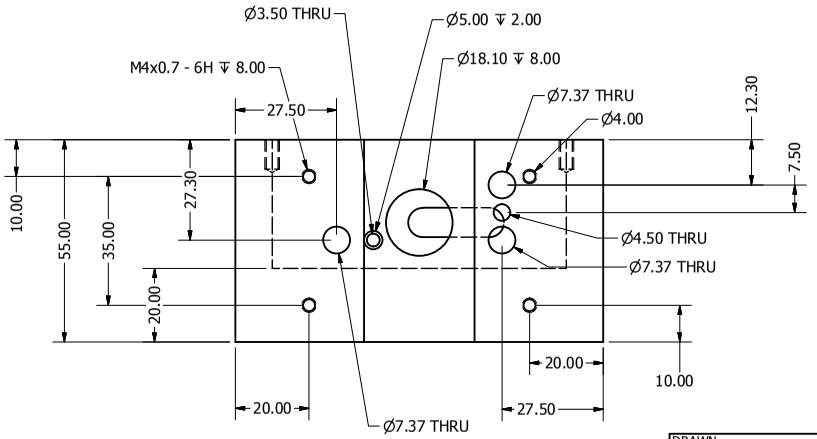

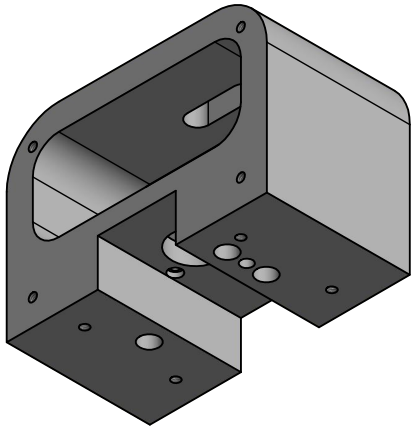

Material: Aluminium

Tolerances:
Linear tolerances

DRAWN Shaun	3/9/2014		
CHECKED		TITLE Diode laser housing	
QA			
MFG			
APPROVED		SIZE C	DWG NO Housing / REV
		SCALE	SHEET 1 OF 1

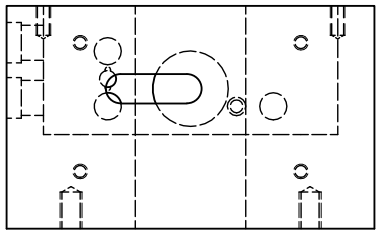

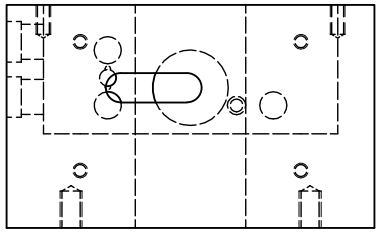

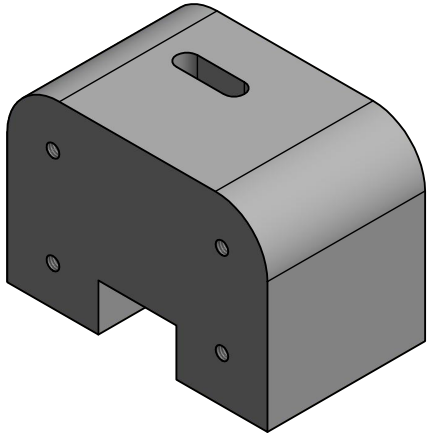

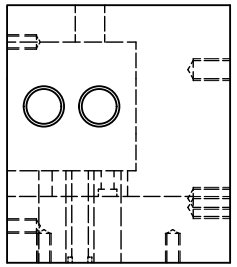

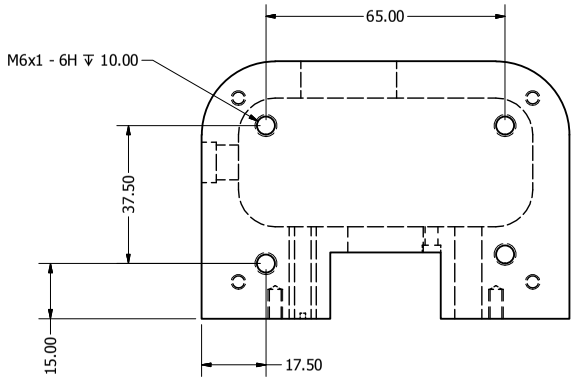

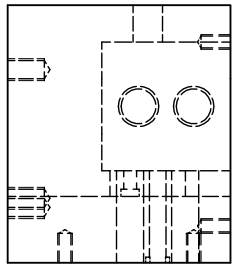

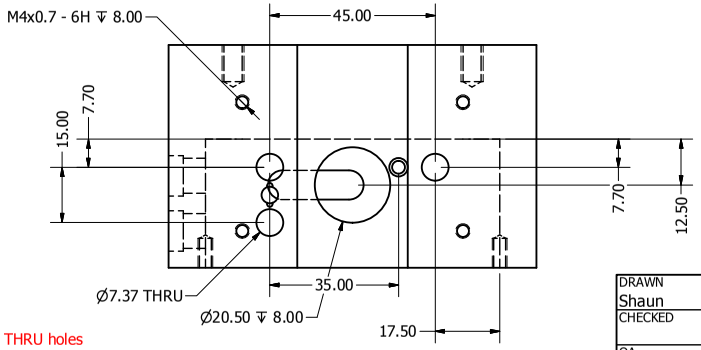

Material: Aluminium

Tolerances unless otherwise specified:
Linear dimensions:
Two decimals - ±0.05mm
One decimal - ±0.1mm
No decimals - ±0.5mm

Angular dimensions:

±0.5°

7.37mm THRU holes are for Thorlabs F19SSN2P threaded bushing. The recommended bore diameter is 0.290"+0.001"/-0.000". Please use this tolerance.

DRAWN	Shaun	3/19/2014	
CHECKED			TITLE: Diode Laser Housing extra details
QA			
MFG			
APPROVED			
SIZE	C	DWG NO	Housing_details
REV			
SCALE		SHEET 1 OF 1	

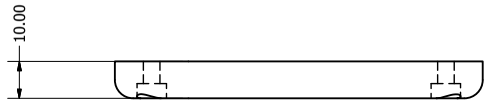

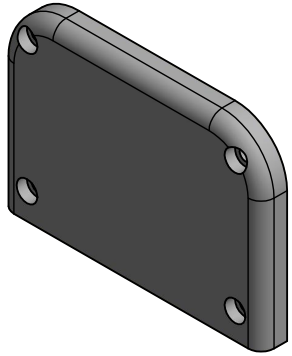

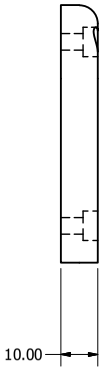

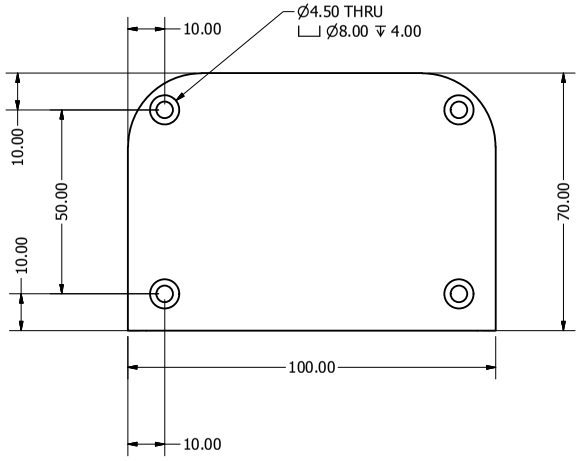

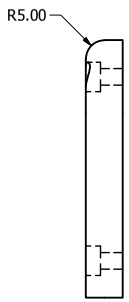

Material: Aluminium

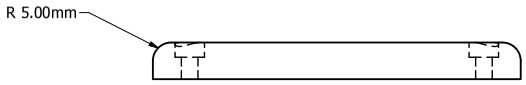

DRAWN Shaun	3/9/2014			
CHECKED		TITLE Lid		
QA				
MFG				
APPROVED		SIZE C	DWG NO Lid	REV
		SCALE	SHEET 1 OF 1	

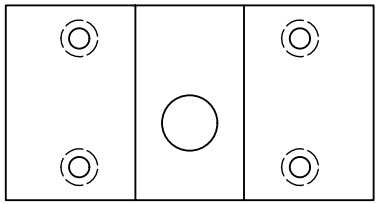

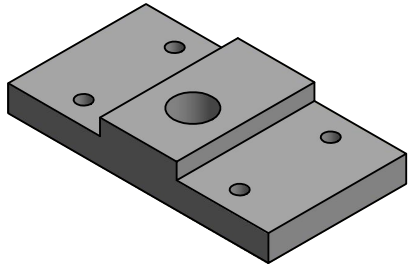

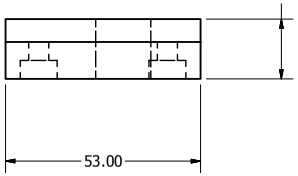

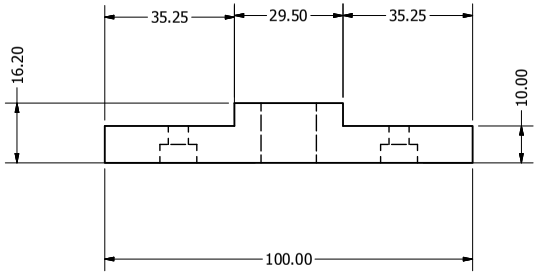

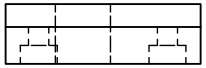

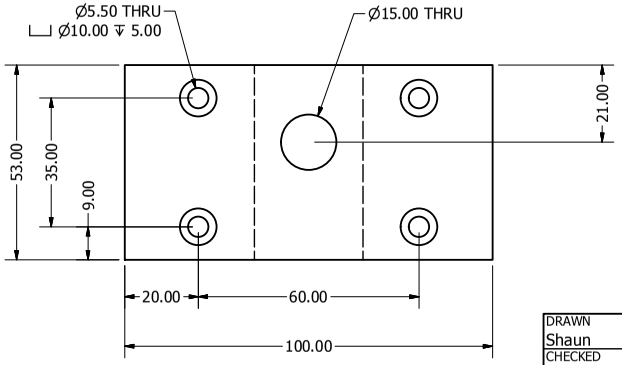

Material: Aluminium

DRAWN Shaun	3/9/2014	
CHECKED		TITLE: Heat sink
QA		
MFG		
APPROVED		
		SIZE C | DWG NO Heat_Sink | REV
		SCALE 1:1 | SHEET 1 OF 1

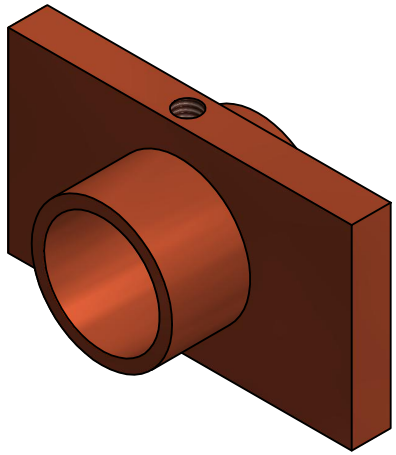

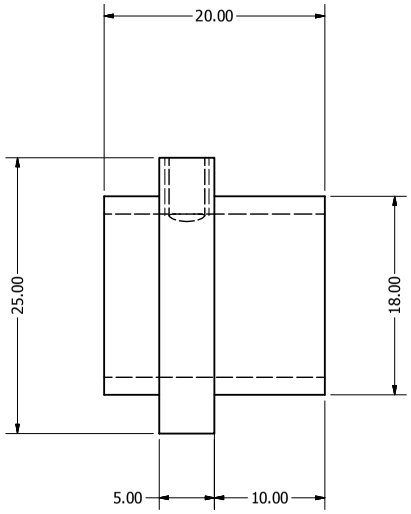

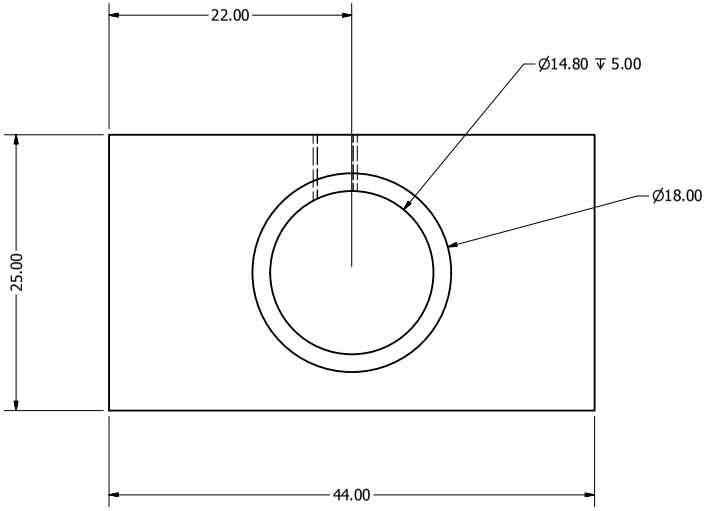

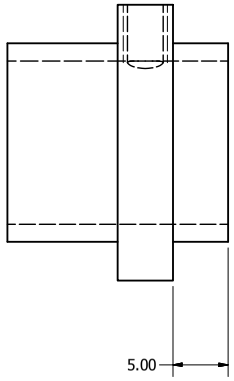

Material: Copper
Tolerances

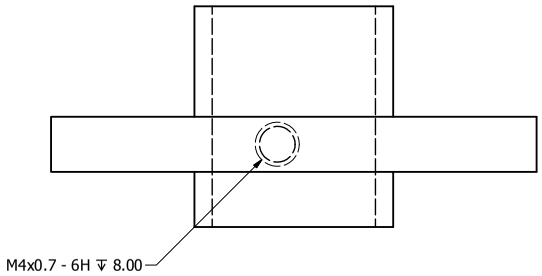

DRAWN Shaun	3/9/2014			
CHECKED		TITLE Collimator holder		
QA				
MFG				
APPROVED				
		SIZE C	DWG NO Collimator holder	REV
		SCALE 3:1	SHEET 1 OF 1	

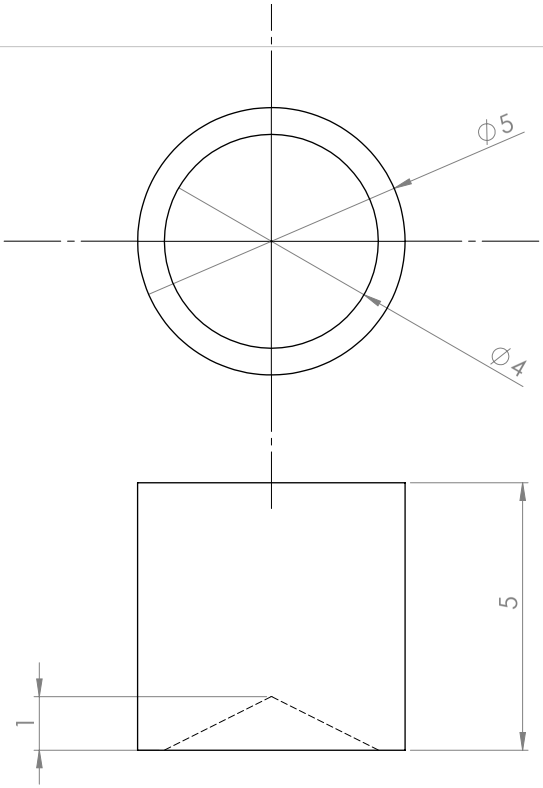

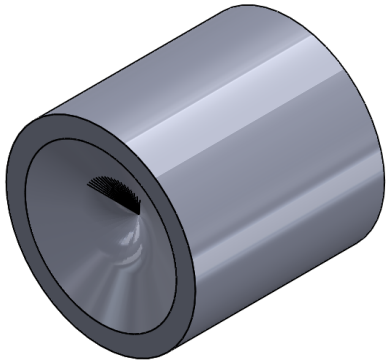

		UNLESS OTHERWISE SPECIFIED:		NAME	DATE
		DIMENSIONS ARE IN MILLIMETERS TOLERANCES: FRACTIONAL ± ANGULAR: MACH ± BEND ± TWO PLACE DECIMAL ± THREE PLACE DECIMAL ±	DRAWN		
			CHECKED		
			ENG APPR.		
			MFG APPR.		
		INTERPRET GEOMETRIC TOLERANCING PER:	Q.A.		
		MATERIAL	COMMENTS:		
NEXT ASSY	USED ON	FINISH			
APPLICATION		DO NOT SCALE DRAWING			

TITLE:

SIZE | DWG. NO. | REV

Aconical hole 2

SCALE: 10:1 | WEIGHT: | SHEET 1 OF 1

5 4 3 2 1

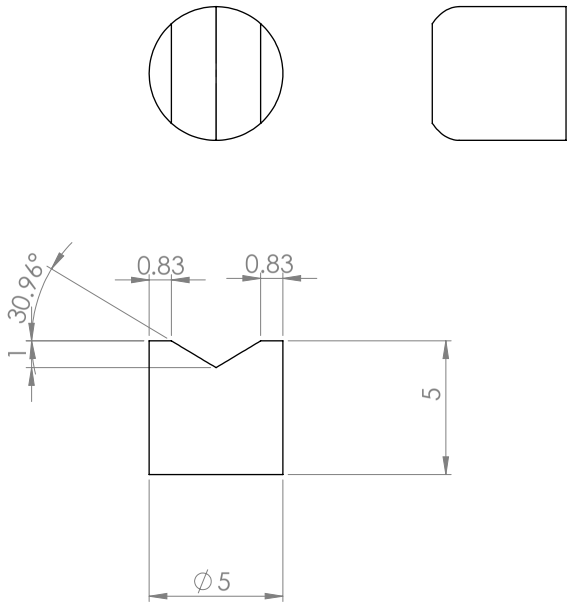

		UNLESS OTHERWISE SPECIFIED:		NAME	DATE
		DIMENSIONS ARE IN MILLIMETERS TOLERANCES: FRACTIONAL ± ANGULAR: MACH ± BEND ± TWO PLACE DECIMAL ± THREE PLACE DECIMAL ±	DRAWN		
			CHECKED		
			ENG APPR.		
			MFG APPR.		
		INTERPRET GEOMETRIC TOLERANCING PER:	Q.A.		
		MATERIAL	COMMENTS:		
NEXT ASSY	USED ON	FINISH			
APPLICATION		DO NOT SCALE DRAWING			

TITLE:

cylinder with wedge

SIZE	DWG. NO.	REV
A		
SCALE: 5:1	WEIGHT:	SHEET 1 OF 1

5 4 3 2 1

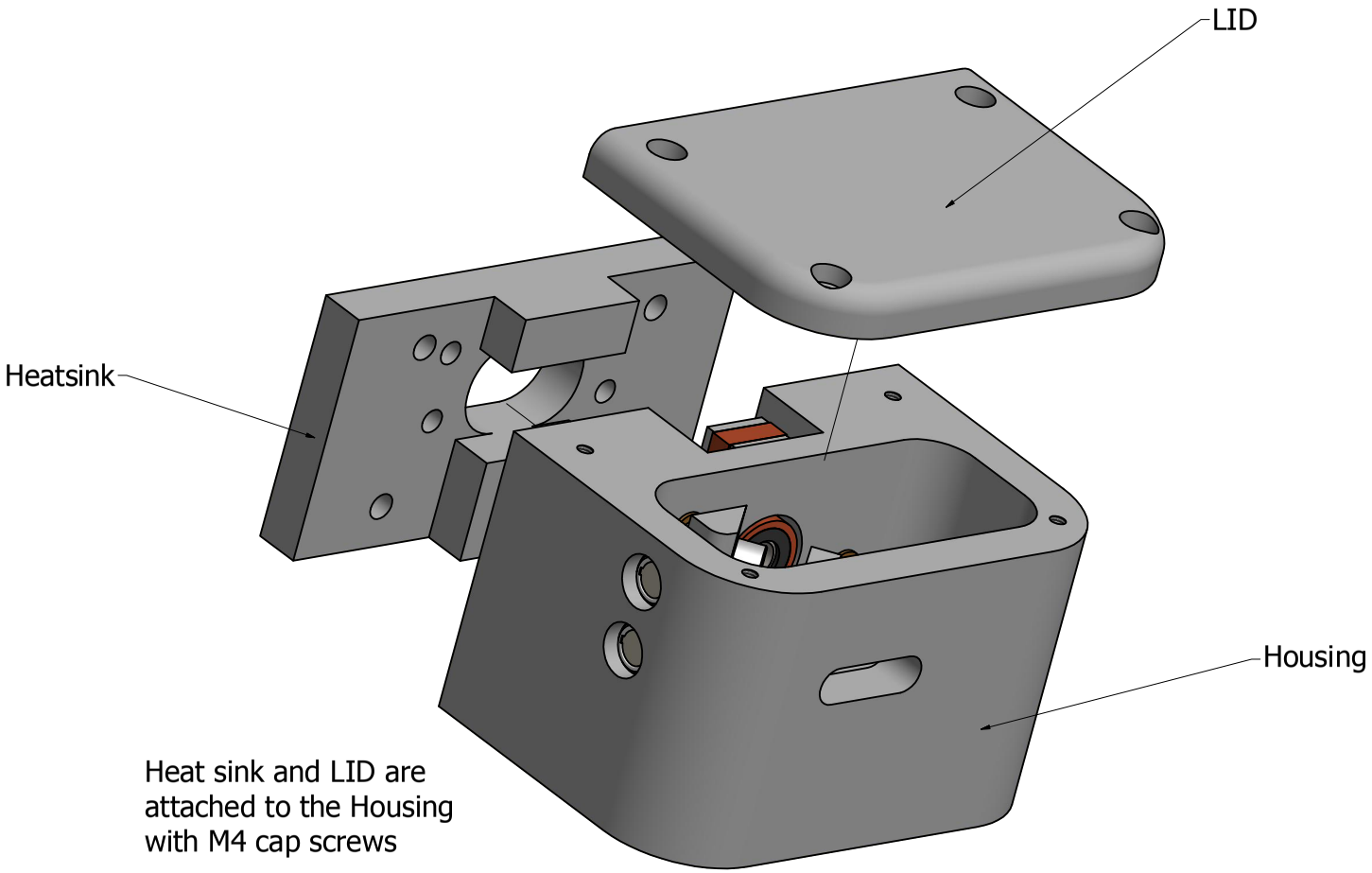

DRAWN Shaun	3/19/2014		
CHECKED		TITLE NLC ECDL Assembly	
QA			
MFG			
APPROVED			
		SIZE C / DWG NO / REV	
		SCALE / SHEET 1 OF 1	

Bibliography

[1]D. J. Griffiths and D. F. Schroeter, *Introduction to quantum mechanics* (Cambridge University Press, 2018).
[2]C. Gerry and P. Knight, *Introductory quantum optics* (Cambridge university press, 2005).
[3]D. A. Steck, "Quantum and atom optics", Oregon Center for Optics and Department of Physics, University of Oregon **47** (2007).
[4]C. J. Foot et al., *Atomic physics*, Vol. 7 (Oxford University Press, 2005).
[5]E. W. Weisstein, *Associated laguerre polynomial*, (2011) http://mathworld.wolfram.com/AssociatedLaguerrePolynomial.html.
[6]L. Allen, M. W. Beijersbergen, R. Spreeuw, and J. Woerdman, "Orbital angular momentum of light and the transformation of laguerre-gaussian laser modes", Physical Review A **45**, 8185 (1992).
[7]L. Allen, S. M. Barnett, and M. J. Padgett, *Optical angular momentum* (CRC Press, 2003).
[8]S. M. Barnett and L Allen, "Orbital angular momentum and nonparaxial light beams", Optics communications **110**, 670–678 (1994).
[9]G. Turnbull, D. Robertson, G. Smith, L Allen, and M. Padgett, "The generation of free-space laguerre-gaussian modes at millimetre-wave frequencies by use of a spiral phaseplate", Optics communications **127**, 183–188 (1996).
[10]K. Sueda, G Miyaji, N. Miyanaga, and M Nakatsuka, "Laguerre-gaussian beam generated with a multilevel spiral phase plate for high intensity laser pulses", Optics express **12**, 3548–3553 (2004).
[11]L. Marrucci, C Manzo, and D Paparo, "Optical spin-to-orbital angular momentum conversion in inhomogeneous anisotropic media", Physical review letters **96**, 163905 (2006).
[12]L. Marrucci, E. Karimi, S. Slussarenko, B. Piccirillo, E. Santamato, E. Nagali, and F. Sciarrino, "Spin-to-orbital conversion of the angular momentum of light and its classical and quantum applications", Journal of Optics **13**, 064001 (2011).
[13]J Arlt, K Dholakia, L Allen, and M. Padgett, "The production of multiringed laguerre–gaussian modes by computer-generated holograms", Journal of modern optics **45**, 1231–1237 (1998).
[14]G. A. Siviloglou and D. N. Christodoulides, "Accelerating finite energy airy beams", Optics Letters **32**, 979–981 (2007).
[15]Y. Qiu, H. Guo, and Z. Chen, "Paraxial propagation of partially coherent hermite–gauss beams", Optics communications **245**, 21–26 (2005).
[16]V. V. Kotlyar, S. N. Khonina, A. A. Almazov, V. A. Soifer, K. Jefimovs, and J. Turunen, "Elliptic laguerre-gaussian beams", JOSA A **23**, 43–56 (2006).
[17]V. Kotlyar, R. Skidanov, S. Khonina, and V. Soifer, "Hypergeometric modes", Optics Letters **32**, 742–744 (2007).

[18]J. Wang, J.-Y. Yang, I. M. Fazal, N. Ahmed, Y. Yan, H. Huang, Y. Ren, Y. Yue, S. Dolinar, M. Tur, et al., "Terabit free-space data transmission employing orbital angular momentum multiplexing", Nature photonics **6**, 488 (2012).
[19]N. Bozinovic, Y. Yue, Y. Ren, M. Tur, P. Kristensen, H. Huang, A. E. Willner, and S. Ramachandran, "Terabit-scale orbital angular momentum mode division multiplexing in fibers", science **340**, 1545–1548 (2013).
[20]D. Richardson, J. Fini, and L. Nelson, "Space-division multiplexing in optical fibres", Nature Photonics **7**, 354 (2013).
[21]Y. Yan, G. Xie, M. P. Lavery, H. Huang, N. Ahmed, C. Bao, Y. Ren, Y. Cao, L. Li, Z. Zhao, et al., "High-capacity millimetre-wave communications with orbital angular momentum multiplexing", Nature communications **5**, 4876 (2014).
[22]S. Fürhapter, A. Jesacher, S. Bernet, and M. Ritsch-Marte, "Spiral interferometry", Optics letters **30**, 1953–1955 (2005).
[23]S. Bernet, A. Jesacher, S. Fürhapter, C. Maurer, and M. Ritsch-Marte, "Quantitative imaging of complex samples by spiral phase contrast microscopy", Optics Express **14**, 3792–3805 (2006).
[24]C. Maurer, A. Jesacher, S. Bernet, and M. Ritsch-Marte, "What spatial light modulators can do for optical microscopy", Laser & Photonics Reviews **5**, 81–101 (2011).
[25]A. Mair, A. Vaziri, G. Weihs, and A. Zeilinger, "Entanglement of the orbital angular momentum states of photons", Nature **412**, 313 (2001).
[26]A. Vaziri, G. Weihs, and A. Zeilinger, "Experimental two-photon, three-dimensional entanglement for quantum communication", Physical Review Letters **89**, 240401 (2002).
[27]S. Gröblacher, T. Jennewein, A. Vaziri, G. Weihs, and A. Zeilinger, "Experimental quantum cryptography with qutrits", New Journal of Physics **8**, 75 (2006).
[28]M. Friese, J Enger, H Rubinsztein-Dunlop, and N. R. Heckenberg, "Optical angular-momentum transfer to trapped absorbing particles", Physical Review A **54**, 1593 (1996).
[29]M. Friese, T. Nieminen, N. Heckenberg, and H Rubinsztein-Dunlop, "Optical alignment and spinning of laser-trapped microscopic particles", Nature **394**, 348 (1998).
[30]L Paterson, M. MacDonald, J. Arlt, W. Sibbett, P. Bryant, and K. Dholakia, "Controlled rotation of optically trapped microscopic particles", Science **292**, 912–914 (2001).
[31]T. Kuga, Y. Torii, N. Shiokawa, T. Hirano, Y. Shimizu, and H. Sasada, "Novel optical trap of atoms with a doughnut beam", Physical Review Letters **78**, 4713 (1997).
[32]N. Simpson, K Dholakia, L Allen, and M. Padgett, "Mechanical equivalence of spin and orbital angular momentum of light: an optical spanner", Optics letters **22**, 52–54 (1997).
[33]T. Hugel, N. B. Holland, A. Cattani, L. Moroder, M. Seitz, and H. E. Gaub, "Single-molecule optomechanical cycle", Science **296**, 1103–1106 (2002).
[34]S Kulin, S Aubin, S Christe, B Peker, S. Rolston, and L. A. Orozco, "A single hollow-beam optical trap for cold atoms", Journal of Optics B: Quantum and Semiclassical Optics **3**, 353 (2001).
[35]K. Wright, L. Leslie, and N. Bigelow, "Optical control of the internal and external angular momentum of a bose-einstein condensate", Physical Review A **77**, 041601 (2008).
[36]A. L. Fetter, "Rotating trapped bose-einstein condensates", Reviews of Modern Physics **81**, 647 (2009).

[37]M. Andersen, C. Ryu, P. Cladé, V. Natarajan, A Vaziri, K. Helmerson, and W. D. Phillips, "Quantized rotation of atoms from photons with orbital angular momentum", Physical review letters **97**, 170406 (2006).
[38]K. T. Kapale and J. P. Dowling, "Vortex phase qubit: generating arbitrary, counter-rotating, coherent superpositions in bose-einstein condensates via optical angular momentum beams", Physical review letters **95**, 173601 (2005).
[39]J. Tabosa and D. Petrov, "Optical pumping of orbital angular momentum of light in cold cesium atoms", Physical review letters **83**, 4967 (1999).
[40]A. de Almeida, S Barreiro, W. Martins, R. de Oliveira, D Felinto, L Pruvost, and J. Tabosa, "Storage of orbital angular momenta of light via coherent population oscillation", Optics letters **40**, 2545–2548 (2015).
[41]M. van Veenendaal and I. McNulty, "Prediction of strong dichroism induced by x rays carrying orbital momentum", Physical review letters **98**, 157401 (2007).
[42]W Löffler, D. Broer, and J. Woerdman, "Circular dichroism of cholesteric polymers and the orbital angular momentum of light", Physical Review A **83**, 065801 (2011).
[43]B. C. Das, D. Bhattacharyya, and S. De, "Narrowing of doppler and hyperfine line shapes of rb–d2 transition using a vortex beam", Chemical Physics Letters **644**, 212–218 (2016).
[44]C. T. Schmiegelow and F. Schmidt-Kaler, "Light with orbital angular momentum interacting with trapped ions", The European Physical Journal D **66**, 157 (2012).
[45]J. Rodrigues, L. Marcassa, and J. Mendonça, "Excitation of high orbital angular momentum rydberg states with laguerre–gauss beams", Journal of Physics B: Atomic, Molecular and Optical Physics **49**, 074007 (2016).
[46]A. Peshkov, V. Serbo, S Fritzsche, and A Surzhykov, "Absorption of twisted light by a mesoscopic atomic target", Physica Scripta **91**, 064001 (2016).
[47]A. Picón, A. Benseny, J. Mompart, J. V. de Aldana, L. Plaja, G. F. Calvo, and L. Roso, "Transferring orbital and spin angular momenta of light to atoms", New Journal of Physics **12**, 083053 (2010).
[48]C. T. Schmiegelow, J. Schulz, H. Kaufmann, T. Ruster, U. G. Poschinger, and F. Schmidt-Kaler, "Transfer of optical orbital angular momentum to a bound electron", Nature communications **7**, 12998 (2016).
[49]F. Le Kien, T. Ray, T. Nieddu, T. Busch, and S. N. Chormaic, "Enhancement of the quadrupole interaction of an atom with the guided light of an ultrathin optical fiber", Physical Review A **97**, 013821 (2018).
[50]K. Sakai, T. Yamamoto, and K. Sasaki, "Nanofocusing of structured light for quadrupolar light-matter interactions", Scientific reports **8**, 7746 (2018).
[51]M Babiker, C. Bennett, D. Andrews, and L. D. Romero, "Orbital angular momentum exchange in the interaction of twisted light with molecules", Physical review letters **89**, 143601 (2002).
[52]A. Alexandrescu, D. Cojoc, and E. Di Fabrizio, "Mechanism of angular momentum exchange between molecules and laguerre-gaussian beams", Physical review letters **96**, 243001 (2006).
[53]A. S. Rury, "Examining resonant inelastic spontaneous scattering of classical laguerre-gauss beams from molecules", Physical Review A **87**, 043408 (2013).
[54]P. K. Mondal, B. Deb, and S. Majumder, "Angular momentum transfer in interaction of laguerre-gaussian beams with atoms and molecules", Physical Review A **89**, 063418 (2014).
[55]J. D. Jackson, *Electrodynamics* (Wiley Online Library, 1975).

[56] A. Pálffy, *Spontaneous emission: weisskopf-wigner theory*, (2015) https://www.mpi-hd.mpg.de/personalhomes/palffy/Files/Spontaneous.pdf.
[57] A. M. Ellis, "Spectroscopic selection rules: the role of photon states", Journal of chemical education **76**, 1291 (1999).
[58] R. D. Cowan, *The theory of atomic structure and spectra*, 3 (Univ of California Press, 1981).
[59] P. Chantry, "Doppler broadening in beam experiments", The Journal of Chemical Physics **55**, 2746–2759 (1971).
[60] A. Arnold, J. Wilson, and M. Boshier, "A simple extended-cavity diode laser", Review of Scientific Instruments **69**, 1236–1239 (1998).
[61] C. Hawthorn, K. Weber, and R. Scholten, "Littrow configuration tunable external cavity diode laser with fixed direction output beam", Review of scientific instruments **72**, 4477–4479 (2001).
[62] S. D. Saliba, M. Junker, L. D. Turner, and R. E. Scholten, "Mode stability of external cavity diode lasers", Applied optics **48**, 6692–6700 (2009).
[63] T. Tiecke, "Properties of potassium", University of Amsterdam, The Netherlands, Thesis, 12–14 (2010).
[64] J. E. Sansonetti, "Wavelengths, transition probabilities, and energy levels for the spectra of potassium (ki through k xix)", Journal of Physical and Chemical Reference Data **37**, 7–96 (2008).
[65] D. Hart and J. Atkinson, "Lifetimes of some excited s and d states of potassium", Journal of Physics B: Atomic and Molecular Physics **19**, 43 (1986).
[66] R. Berends, W Kedzierski, J. Atkinson, and L Krause, "The radiative lifetimes of the potassium 5p, 6p and 7p states", Spectrochimica Acta Part B: Atomic Spectroscopy **43**, 1069–1073 (1988).
[67] E. Arimondo, M Inguscio, and P Violino, "Experimental determinations of the hyperfine structure in the alkali atoms", Reviews of Modern Physics **49**, 31 (1977).
[68] A Banerjee, D Das, and V Natarajan, "Absolute frequency measurements of the d1 lines in 39k, 85rb, and 87rb with 0.1 ppb uncertainty", EPL (Europhysics Letters) **65**, 172 (2004).
[69] S. Falke, E. Tiemann, C. Lisdat, H. Schnatz, and G. Grosche, "Transition frequencies of the d lines of k 39, k 40, and k 41 measured with a femtosecond laser frequency comb", Physical Review A **74**, 032503 (2006).
[70] D. Das and V. Natarajan, "High-precision measurement of hyperfine structure in the d lines of alkali atoms", Journal of Physics B: Atomic, Molecular and Optical Physics **41**, 035001 (2008).
[71] A Sieradzan, R Stoleru, W. Yei, and M. Havey, "Measurement of hyperfine coupling constants in the 3 d t 2 d j levels of k 39, k 40, and k 41 by polarization quantum-beat spectroscopy", Physical Review A **55**, 3475 (1997).
[72] E. A. Chan, S. A. Aljunid, N. I. Zheludev, D. Wilkowski, and M. Ducloy, "Doppler-free approach to optical pumping dynamics in the 6s 1/2- 5d 5/2 electric quadrupole transition of cesium vapor", Optics letters **41**, 2005–2008 (2016).
[73] F Ponciano-Ojeda, S Hernández-Gómez, C Mojica-Casique, L. Hoyos, J Flores-Mijangos, F Ramírez-Martínez, D Sahagún, R Jáuregui, and J Jiménez-Mier, "Laser spectroscopy of the 5 p 3/2 to 6 p j (j= 1/2 and 3/2) electric dipole forbidden transitions in atomic rubidium", in Aip conference proceedings, Vol. 1950, 1 (AIP Publishing, 2018), p. 030001.